論文 / 著書情報
Article / Book Information

題目(和文)	
Title(English)	Development of Amorphous Carbon Tribological Coatings with Wear-Sensing Capability Using Luminescent ZnS-Based Underlayer
著者(和文)	Salee Atsawin
Author(English)	Atsawin Salee
出典(和文)	学位:博士(工学), 学位授与機関:東京工業大学, 報告番号:甲第9447号, 授与年月日:2014年3月26日, 学位の種別:課程博士, 審査員:平田　敦,戸倉　和,赤坂　大樹,花村　克悟,田中　智久
Citation(English)	Degree:Doctor (Engineering), Conferring organization: Tokyo Institute of Technology, Report number:甲第9447号, Conferred date:2014/3/26, Degree Type:Course doctor, Examiner:,,,,
学位種別(和文)	博士論文
Type(English)	Doctoral Thesis

Development of Amorphous Carbon Tribological Coatings with Wear-Sensing Capability Using Luminescent ZnS-Based Underlayer

Atsawin SALEE

Department of Mechanical Sciences and Engineering

Tokyo Institute of Technology

Doctoral Thesis (Academic Year 2013)

Table of contents

Table of contents I
Lists of figures IV
Lists of tables X

Chapter 1

1. Introduction 2

1.1. Friction and wear of tribological coatings 2
1.2. Wear monitoring of tribological coatings 3
1.2.1. Electrical resistivity measurement 3
1.2.2. Acoustic emission analysis 5
1.2.3. Luminescent spectroscopy 7
1.3. Amorphous carbon (a-C) films 9
1.3.1. Structure and classification of a-C films 9
1.3.2. Deposition of a-C films 11
1.4. Friction and wear of a-C films 16
1.4.1. Intrinsic factors 17
1.4.2. Extrinsic factors 18
1.4.3. Tribological applications of a-C films 23
1.5. Potential wear monitoring technique for a-C films 23
1.6. Objectives of this research 28
1.7. Structures of thesis 30
1.8. References 31

Chapter 2

2. Amorphous carbon coatings with ZnS:Mn underlayer 36

2.1. Introduction 36
2.2. Experimental 37
2.2.1. Fabrication of ZnS:Mn layers 37
2.2.2. Deposition of amorphous carbon (a-C) films 39
2.2.3. Coating characterisations 40

2.3. Results and discussion 41
2.3.1. A preliminary study on deposition of a-C films by R.F. magnetron sputtering 41
2.3.2. Luminescent ZnS:Mn layers 48
2.3.3. Depositions of a-C films on ZnS:Mn layers by R.F. magnetron sputtering method 63
2.4. Conclusion 76
2.5. References 77

Chapter 3

3. Amorphous carbon coatings with epoxy resin underlayer containing ZnS:Cu phosphor 82
3.1. Introduction 82
3.2. Experimental 84
3.2.1. Fabrication of epoxy resin coatings containing ZnS:Cu phosphor (EP/Zn:Cu) 84
3.2.2. Deposition of amorphous carbon (a-C) films 85
3.2.3. Coating characterisations 87
3.3. Results and discussion 88
3.3.1. As-fabricated EP/ZnS:Cu layers 88
3.3.2. a-C coatings with EP/ZnS:Cu underlayer deposited by sublimation of fullerene (C_{60}) powder in electron beam excited plasma (EBEP) method 93
3.3.3. a-C coatings with EP/ZnS:Cu underlayer deposited by pulsed vacuum arc deposition (VAD) method 105
3.4. Conclusion 122
3.5. References 124

Chapter 4

4. Amorphous carbon coatings with silica underlayer containing CdSe/ZnS quantum dots 128
4.1 Introduction 128

4.2 Experimental 130
4.2.1 Fabrication of silica coatings containing CdSe/ZnS quantum dots (silica/QD) 130
4.2.2 Deposition of amorphous carbon (a-C) films 130
4.2.3 Coating characterisations 132
4.3 Results and discussion 133
4.3.1 As-fabricated silica/QD layers 133
4.3.2 Deposition of a-C films on silica/QD layers by R.F. magnetron sputtering method 140
4.3.3 Demonstration of wear monitoring 149
4.4 Conclusion 156
4.5 References 158

Chapter 5

5. Summary of thesis 161
5.1 Thesis conclusions 161
5.2 Considerable issues concerning the present research for further studies 164
5.2.1 The luminescent sensing layer 164
5.2.2 Amorphous carbon layer 165
5.2.3 Overall coating system 166

Acknowledgements 167

Lists of figures

Chapter 1:

Fig. 1.1 (a) Schematic drawing of the proposed model of wear and temperature sensing layer by resistivity measurement [9], (b) WC insert with Al_2O_3 based coating and sensor level [10] 5

Fig. 1.2 (a) Wear-life diagram of CrN-coated steel disk using AE signal [13], (b) schematic of AE and frictional force vs. test time for a-C:H films delamination [14] 6

Fig. 1.3 (a) Schematic diagram of the concept of wear monitoring of the thermal barrier coating by luminescent spectroscopy [15], (b) schematic diagram of multilayered MoS_2 coatings with imbedded luminescent (Doped YSZ) wear-sensing layers, (c) optical spectra from the wear track after a wear test at 10,000 cycles and (d) at 150,000 cycles [16] 8

Fig. 1.4 The sp^3, sp^2 and sp^1 hybridised bonding [17] 10

Fig. 1.5 Ternary phase diagram of various a-C films with respect to their sp^2, sp^3 and hydrogen contents [19] 11

Fig. 1.6 Schematics of various deposition systems for a-C films [17,33] 12

Fig. 1.7 The various structures of conventional tribological coatings [49] 18

Fig. 1.8 The influence of an intermediate layer on durability of a-C:H films deposited on aluminium alloys [58] 19

Fig. 1.9 The wear rates of a-C:H films in sliding against different counterface materials and loads [63] 20

Fig. 1.10 The coefficient of friction values at the end of the tests for (a) a-C:H coating and (b) ta-C coating sliding against stainless steel [48] 21

Fig. 1.11 Effect of atmospheres on the friction characteristics of a-C:H and ta-C films [66] 22

Fig. 1.12 Optical absorption coefficients spectra of MoS_2 and a-C films [77,78] 25

Fig. 1.13 An expected structure of a-C coating with luminescent ZnS-based underlayer .29

Chapter 2:

Fig. 2.1 Schematic diagram of the R.F. magnetron sputtering system 39
Fig. 2.2 Optical microscopic images observed on the surfaces of a-C films deposited by R.F. magnetron sputtering at Ar pressure of (a) 10.0 Pa, (b) 1.0 Pa and (c) 0.4 Pa 42
Fig. 2.3 Raman spectra of a-C films deposited on Si-wafers by R.F. magnetron sputtering at Ar pressure of (a) 10.0 Pa, (b) 1.0 Pa and (c) 0.4 Pa 44
Fig. 2.4 Friction behaviours of a-C films deposited on Si-wafers by R.F. magnetron sputtering at Ar pressure of (a) 10.0 Pa and (b) 1.0 Pa..... 46
Fig. 2.5 Wear tracks formed on a-C films deposited by R.F. magnetron sputtering at Ar pressure of (a) 10.0 Pa and (b) 1.0 Pa after the friction tests 47
Fig. 2.6 Optical microscopic images observed on the surfaces of as-deposited and post-annealed ZnS:Mn films deposited on (a) soda-lime glass and (b) Si-wafer 50
Fig. 2.7 (a, b) SEM images of the fractured cross-section and (c, d) AFM images showing the surface morphologies of as-deposited and post-annealed ZnS:Mn films..... 51
Fig. 2.8 XRD patterns of (a) ZnS:Mn target, (b) as-deposited ZnS:Mn film and (c) ZnS:Mn film after post-annealing at 700°C 53
Fig. 2.9 Nanoindentation load-displacement curves for the as-deposited and post-annealed ZnS:Mn films 56
Fig. 2.10 (a) Photoluminescence (PL) investigation and PL spectra of as-deposited and post-annealed ZnS:Mn films under irradiating with a UV light at 365 nm and (b) a schematic luminescence process in ZnS:Mn crystal [45]..... 58
Fig. 2.11 UV-VIS absorption spectra of as-deposited and post-annealed ZnS:Mn films and the relationship between $(\alpha.hv)^2$ and hv of both films for determining the energy gap (inset) 60
Fig. 2.12 Raman spectra of as-deposited and post-annealed ZnS:Mn films excited by a green laser with the wavelength 532 nm 62
Fig. 2.13 Raman spectrum of a-C film deposited on as-deposited ZnS:Mn layer, while the inset showing the Raman spectrum of a-C film deposited on post-annealed

ZnS:Mn layer 65
Fig. 2.14 (a) and (b) showing the optical microscopic images, while (c) and (d) showing the AFM images of a-C/ZnS:Mn and a-C/Si/ZnS:Mn coatings, respectively 67
Fig. 2.15 Photoluminescence spectra of (a) a-C/ZnS:Mn and (b) a-C/Si/ZnS:Mn coatings compared with the as-fabricated ZnS:Mn layers 68
Fig. 2.16 UV-VIS absorbance spectra of a-C film deposited on soda-lime glasses without and with Si-intermediate layers 69
Fig. 2.17 Friction behaviours of a-C/ZnS:Mn and a-C/Si/ZnS:Mn coatings 70
Fig. 2.18 Optical microscopic images observed on the wear tracks formed on (a) a-C/ZnS:Mn and (b) a-C/Si/ZnS:Mn coatings and the contact ball surfaces 72
Fig. 2.19 Load-displacement curves of (a) a-C/ZnS:Mn and (b) a-C/Si/ZnS:Mn coatings as well as a-C films coated on Si-wafers and bare ZnS:Mn layer analysed by nanoindatation at the indented load 0.5 mN 73
Fig. 2.20 Photoluminescence spectra measured from the wear tracks of (a) a-C/ZnS:Mn and (b) a-C/Si/ZnS:Mn coatings 75

Chapter 3:

Fig. 3.1 SEM image of the as-purchased ZnS:Cu phosphor powder 85
Fig. 3.2 Schematic diagram of the electron beam excited plasma EBEP deposition system for a-C films 86
Fig. 3.3 Schematic diagram of vacuum arc deposition set-up for amorphous carbon films 87
Fig. 3.4 (a) SEM image at the fractural surface of the as-fabricated EP/ZnS:Cu coating, (b) optical microscopic image of EP/ZnS:Cu coating after curing and removing of polystyrene and (c) surface profile of the coating measure by laser profilometer 90
Fig. 3.5 Raman spectrum of the as-fabricated EP/ZnS:Cu coating 91
Fig. 3.6 Photoluminescence spectra of (a) as-fabricated EP/ZnS:Cu coating and (b) as-purchased ZnS:Cu phosphor powder under irradiated with UV light at 365 nm 92
Fig. 3.7 SEM images at the fractured surfaces of a-C films deposited on EP/ZnS:Cu layer (left) and Si-wafer (right) by sublimation of C_{60} in EBEP method at bias voltage

(V_b) of (a) -200 V and (b) 0 V 94
Fig. 3.8 Optical microscopic images observed at surfaces of a-C coatings with EP/ZnS:Cu underlayer deposited by sublimation of C_{60} in EBEP method at V_b of (a) -200 V and (b) 0 V as well as (c) defective surface profiles formed on the coatings 95
Fig. 3.9 Raman spectra obtained from a-C coatings with EP/ZnS:Cu underlayer and on Si-wafers deposited by sublimation of C_{60} in EBEP method at V_b of (a) -200 V and (b) 0 V 97
Fig. 3.10 Photoluminescence spectra of EP/ZnS:Cu before and after being deposited with a-C films by sublimation of C_{60} in EBEP method at V_b of (a) -200 V and (b) 0 V 100
Fig. 3.11 Friction behaviours of a-C coatings with EP/ZnS:Cu underlayer and on Si-wafers deposited by sublimation of C_{60} in EBEP method at V_b of (a) -200 V and (b) 0 V 102
Fig. 3.12 Optical microscopic images of the wear tracks formed on the surfaces of a-C coatings with EP/ZnS:Cu underlayer and on Si-wafer deposited by sublimation of C_{60} in EBEP method at V_b of (a, b) -200 V and (c, d) 0 V, respectively 103
Fig. 3.13 Photoluminescence spectra detected from the wear tracks after the friction test of a-C coatings with EP/ZnS:Cu underlayer deposited by sublimation of C_{60} in EBEP method at V_b of (a) -200 V and (b) 0 V 105
Fig. 3.14 SEM images of fractured surfaces of a-C deposited on (a) EP/ZnS:Cu layer and (b) Si-wafer by pulsed VAD method at 6000 pulses of discharge 106
Fig. 3.15 (a) Optical microscopic image and (b) surface profile scanned across the surface of a-C coatings with EP/ZnS:Cu underlayer and (C) optical microscopic image of a-C film deposited on Si-wafer by pulsed VAD method at 6000 pulses of discharge 108
Fig. 3.16 Raman spectra of a-C film with EP/ZnS:Cu underlayer and on Si-wafer deposited by pulsed VAD at 6000 pulses of discharge 110
Fig. 3.17 Photoluminescence spectra of EP/ZnS:Cu coatings as-fabricated and after being coated with a-C films by pulses VAD method at 6000 pulses of discharge 111
Fig. 3.18 Friction behaviours of a-C films with EP/ZnS:Cu underlayer and on Si-wafers deposited by pulsed VAD method at 6000 pulses of discharge sliding against (a)

stainless steel and (b) alumina balls at normal load of 0.77 N 113
Fig. 3.19 Optical microscopic images of the wear tracks formed on the surfaces of a-C coatings with (a, b) EP/ZnS:Cu underlayer and (c, d) on Si-wafer deposited by pulsed VAD at 6000 pulses after sliding against stainless steel and alumina balls, respectively 115
Fig. 3.20 Photoluminescence spectra detected from the wear tracks of a-C coatings with EP/ZnS:Cu underlayer deposited by pulsed VAD method at 6000 pulses of discharge after sliding against (a) stainless steel and (b) alumina balls 117
Fig. 3.21 (a) Photoluminescence (PL) spectra detected from the a-C coatings with EP/ZnS:Cu underlayer at various thicknesses of a-C film and (b) relationship between PL intensity at the peak centre of 525 nm as a function of a-C film thickness including the fitted equation and the coefficient of determination (R^2) 119
Fig. 3.22 Typical load-displacement curves of a-C films deposited on Si-wafer and EP/ZnS:Cu layer by pulsed VAD at 6000 pulses of discharge as well as the bare EP/ZnS:Cu layer analysed by nanoindentation at the indented load of 6 mN .. 121
Fig. 3.23 Surface profilometer scanning along the surface of as-fabricated a-C coating with EP/ZnS:Cu underlayer 122

Chapter 4:

Fig. 4.1 SEM image of cross-section of silica/QD coating 133
Fig. 4.2 FT-IR spectra showing the molecular conversion from PSZ/QD to silica/QD coating after curing at 50°C for 3 hr in relative humidity higher than 80% 134
Fig. 4.3 (a) Optical microscopic and (b) AFM image of as-fabricated silica/QD layer and (c) AFM image of neat silica coating 136
Fig. 4.4 (a) Photoluminescence (PL) investigation of as-fabricated silica/QD coating under irradiating with a UV light at 365 nm and (b) schematic band diagram showing the excitation and relaxation transitions of electron-hole in CdSe/ZnS quantum dots [21,22] 137
Fig. 4.5 Raman spectra measured from (a) silica/QD coating, (b) Neat CdSe/ZnS QD and (d) neat silica coating under the laser excitation at 532 nm 139
Fig. 4.6 Surface appearances observed with optical microscope of a-C/silica/QD coatings

prepared by (a) sublimation of C_{60} in EBEP method at the substrate bias voltage of -200 V and (b) pulsed VAD method at 6000 pulses of discharge with 20-nm-tungsten intermediate layer 141

Fig. 4.7 Optical microscopic and AFM images of (a) a-C/silica/QD coating (a-C layer thickness: 85 nm), (b) a-C/Si/silica/QD coating (a-C/Si layer thickness: 109 nm) and (c) a-C/Si/silica/QD coating (a-C/Si layer thickness: 364 nm) 143

Fig. 4.8 Raman spectra of a-C coatings with silica/QD underlayer deposited by R.F. magnetron sputtering, in which (a) a-C/silica/QD (a-C: 85 nm) and a-C/Si/silica/QD (a-C/Si: 109 nm) coatings, (b) a-C/Si/silica/QD (a-C/Si: 364 nm) coating and (c) a-C/Si coating on Si-wafer (a-C/Si: 364 nm)..... 145

Fig. 4.9 Friction behaviours of various a-C coatings with silica/QD underlayer deposited by R.F. magnetron sputtering 147

Fig. 4.10 Optical microscopic images observed on the wear tracks formed on the a-C coatings with silica/QD underlayer deposited by R.F. magnetron sputtering, in which (a) a-C/silica/QD coating (a-C: 85 nm) and (b and c) a-C/Si/silica/QD coatings (a-C/Si: 109 and 364 nm, respectively)..... 149

Fig. 4.11 Luminescence investigation by Raman spectroscopy measured from the coatings at various a-C coating thicknesses..... 150

Fig. 4.12 Relationship between luminescent intensity from the coating as a function of coating thickness including the fitted equation and coefficient of determination (R^2)..... 152

Fig. 4.13 (a) The area on wear track of a-C/Si/silica/QD coating with total thickness of 364 nm for wear monitoring demonstration, (b) Raman spectra obtained from the wear tracks at different three adjacent positions compared with the spectrum obtained from the virgin coating 154

Fig. 4.14 (a) AFM image obtained from the wear track at white dash area shown in Fig. 4.13, and (b) surface profile scanning across the wear track analysed by AFM (Note that position A and B are the reference positions for measuring the depth of wear track)..... 155

Lists of tables

Chapter 1:

Table 1.1 Some major properties of various a-C films as well as diamond and graphite [29,33,35].....15
Table 1.2 Energy conversion efficiencies (η) of some typical luminescent materials [81,82].....27
Table 1.3 Triboluminescence (TrL) of various materials [83] 27

Chapter 2:

Table 2.1 Process parameters for fabrication of ZnS:Mn layer by R.F. magnetron sputtering and post-annealing.....38
Table 2.2 Sputtering conditions to determine the deposition rate of a-C films.....40
Table 2.3 Thickness and corresponding deposition rate of a-C films deposited at various pressures measured by SEM at fractural surfaces 41
Table 2.4 Positions and widths of the D and G bands from the Gaussian peaks fitting of the Raman spectra in Fig. 2.3 as well as ratio of their integrated intensities ...43
Table 2.5 Ball-on-disk friction test condition for a-C film deposited by R.F. magnetron sputtering at various Ar pressures 46
Table 2.6 Thermal expansion coefficients of ZnS and a few other materials used as substrates for deposition of ZnS films [9,26] 49
Table 2.7 Structural parameters of as-deposited and post annealed ZnS:Mn films determined from the XRD patterns in Fig. 2.8 using Eq. (2.1)-(2.5) 56
Table 2.8 Hardness, elastic modulus and indentation depth of as-deposited and post-annealed ZnS:Mn films indented at 1.5 mN load.....56
Table 2.9 Process parameters and conditions for deposition of a-C film on ZnS:Mn layer by R.F. magnetron sputtering method 64
Table 2.10 Ball-on-disk friction test conditions for a-C/ZnS:Mn and a-C/Si/ZnS:Mn coatings fabricated by R.F. magnetron sputtering 70

Chapter 3:

Table 3.1 Deposition conditions for a-C films deposited by sublimation of C_{60} powder in electron beam excited plasma (EBEP) method 86
Table 3.2 Deposition conditions for a-C films deposited by pulsed vacuum arc deposition (VAD) method 87
Table 3.3 Thicknesses of a-C films deposited on EP/ZnS:Cu layers and Si-wafers by sublimation of C_{60} in EBEP at bias voltages (V_b) of -200 and 0 V 94
Table 3.4 Ball-on-disk friction test conditions for a-C films deposited by sublimation of C_{60} in EBEP method 101
Table 3.5 Hardnesses and Young's moduli of epoxy resin layer and a-C film deposited by pulsed VAD at 6000 pulses of discharge measured by nanoindentation method 107
Table 3.6 Ball-on-disk friction test conditions for a-C coatings deposited by pulsed VAD method 112

Chapter 4:

Table 4.1 Process parameters and conditions for deposition of a-C coatings on luminescent silica/QD layer 131
Table 4.2 Positions and widths of the D and G bands from the Gaussian peaks fitting of the Raman spectra in Fig. 4.8(b) and (c) as well as ratio of their integrated intensities 144
Table 4.3 Ball-on-disk friction test conditions for a-C coatings with silica/QD underlayer prepared by R.F. magnetron sputtering 146
Table 4.4 Determination of remaining coating thickness after the friction test of a-C/Si/silica/QD coating by luminescent spectroscopy and profilometry 153

CHAPTER 1

INTRODUCTION

1. Introduction

1.1 Friction and wear of tribological coatings

Since it has been realised that friction and wear take considerably large part in the economic and energy losses [1,2], it is a considerable issue to reduce friction and control wear through applying tribological coatings. Tribological coatings are designed to reduce or control friction and wear between two moving surfaces. Furthermore, other issues regarding the growing need of tribological coatings are, for example, to extend the lifetime of machinery or tribosystems, to make engines and devices more efficient, to develop new advanced products, to conserve scarce material resources, and to improve safety.

The most common tribological hard coatings include nitrides (TiN, CrN, etc.), carbides (TiC, CrC, W_2C, WC/C, etc.) oxides (e.g. alumina) or combinations of these. In addition to these material groups, molybdenum disulphide (MoS_2) amorphous carbon (a-C) and diamond have also become successful. Nitrides, carbides and oxides are classified as wear resistance coatings, but their coefficients of friction (COF) values are considerably high in dry sliding. WC/C, MoS_2 and hydrogenated a-C are classified as low friction coatings because of their low COF values in dry sliding. However, the wear resistance is generally inferior to those of previous groups. Exceptions to these classifications are diamond and non-hydrogenated a-C coatings, which combine both low friction and high wear resistance [3,4].

Friction and wear characteristics of the coatings appear to stem from a complex combination of intrinsic and extrinsic factors. Intrinsically, the friction and wear behaviours of the coatings are strongly affected by their chemical and structural natures. This factor can be controlled easily by a proper design and selection of the deposition process. Extrinsically, the servicing or testing conditions, including the nature of substrate,

counterface materials, applied load, sliding velocity, ambient temperature and nature of surrounding atmosphere, play significant roles in tribological characteristics of the coatings [5,6].

For the extrinsic factors, the friction and wear characteristics of tribological coatings are typically obtained from a certain test condition in the experimental scale by keeping one factor constant, while others are varied. However, these factors are not constant in the actual servicing condition and are difficult to be controlled or monitored. As a result, a pre-mature failure of the coating and/or pre-replacement of the parts before coating failure can occasionally occur. In order to avoid these unexpected situations, it would be preferable to have a wear monitoring method that could be applied continuously, producing real-time and/or direct information on the monitored part to provide an indication of remaining coating life and sufficient warning before failure. Wear monitoring of the coatings does not only provide the state of the coating and sufficient warning before failure, but it also allows the user to rely more heavily on the coating. As a result, the degree of over-engineering can be reduced and the pre-replacement due to an uncertainty about the condition of the coating can also be minimised.

1.2 Wear monitoring of tribological coatings

Several approaches have been proposed for monitoring the wear life of the tribological coatings, for example;

1.2.1 Electrical resistivity measurement

This technique has been initially applied to measure the wear of magnetic record head in 1970s-1980s [7]. The sensing element in this test is a thin film of iron-nickel metal alloy (Fe-Ni) deposited onto the surface of a non-conductive ceramic substrate previously

contoured and polished to surface of an actual recording head. Suitable electrical connections are made such that the resistance of the film can be monitored. Wear of the film creates a change in the resistance by interpreting an out-of-balance voltage from a simple bridge circuit. By this technique, the wear depth of recording head can be monitored as a function of the length of magnetic tapes passed over the sensor.

The utilisation of this technique has also been proposed to monitor the wear of bearing case [8,9]. The design of the thin-film wear and temperature sensors involves the lamination of conducting films, such as platinum (Pt) or tantalum (Ta), with insulating layers, such as alumina (Al_2O_3), Glass (SiO_2) and tantala (Ta_2O_5), located parallel to and directly on the bearing surface as represented in Fig. 1.1(a). To reveal the relationship between the change in resistivity and wear amount of thin film, a simple geometry structure coupled with a linear wear rate and the resistivity of the film is considered. Since the initial thickness of each layer in the laminates is known, the progression of wear can be followed as each conducting layer wears through and fails in electrical continuity. The sensor resistance is measured during the test by feeding a constant electric current to the sensor and measuring the change of voltage. Wear through failure of the sensor is indicated by much higher voltage reading. From the coating construction, the change in the resistance of the conductive film as a function of thickness change due to the wear during the test can be modelled by using the relationship

$$R_g = R_0 + R_w \tag{1.1}$$

where R_g is the measured resistance, R_0 is the initial resistance and R_w is the wearing resistance. The wearing resistance may be expressed as

$$R_w = \rho w / lx \tag{1.2}$$

Hence,

$$R_g = R_0 + \rho w / Lx \tag{1.3}$$

where ρ is the measured resistivity, L and w are the length and the width of the wear scar, respectively and x is the instantaneous thickness of the film.

Recently, based on the combination of advanced coating techniques with the MEMs technology, the smart tool with wear detection was realised [10]. Figure 1.1(b) shows an example of smart cutting tool with the wear detection sensor embedded in the insert fabricated by an advanced MEMs technology.

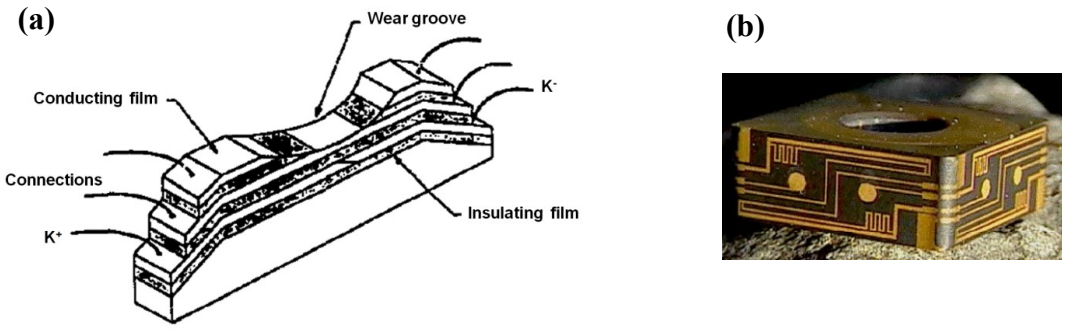

Fig. 1.1 (a) Schematic drawing of the proposed model of wear and temperature sensing layer by resistivity measurement [9], (b) WC insert with Al_2O_3 based coating and sensor level [10]

1.2.2 Acoustic emission analysis

Acoustic emission (AE) can be defined as the transient elastic energy spontaneously released in materials undergoing deformation, fracture or both. The emission signal is usually detected by an instrumentation system (in which transducers are stimulated by the stress waves generated during energy release), amplified and transmitted to an analyser. The emission signal occurs as one of two distinctive types: burst (high amplitude low frequency signal generally associated with surface events such as slip-line

formation and surface microcracks) and continuous (lower amplitude high frequency signal generally associated with internal mechanism activity such as that occurring during tensile tests of specimens) [11].

AE has been investigated for tribological applications, especially used in wear studies of tribomaterials. The research group of Lee, et al. has used the AE analysis to evaluate the wear-life of TiN [12] and CrN [13] coated steel and finally proposed the wear-life diagrams of the coatings, as shown in Fig. 1.2(a), which can be used to predict the safe sliding conditions of the coated specimens.

Kustas, et al. [14] has applied the AE analysis to monitor the damage of a-C:H or DLC films during sliding wear. By measuring both the AE generated and the frictional force produced during sliding friction, it was found that both signals are sensitive indicators of damage to the a-C:H coating, and that these parameters are proportional to each other as can be seen in Fig. 1.2(b). Moreover, AE appears to be a more sensitive, early time indicator of initial DLC degradation than frictional force output.

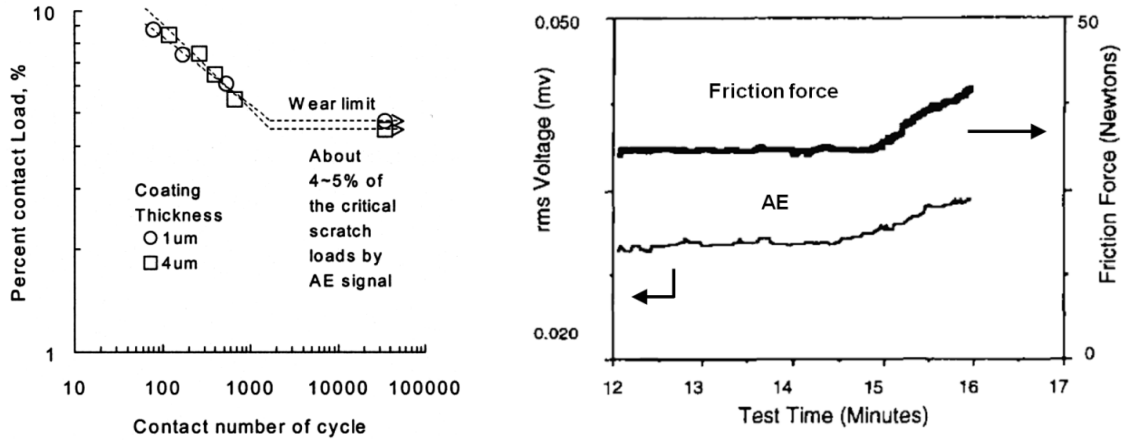

(a) **(b)**

Fig. 1.2 (a) Wear-life diagram of CrN-coated steel disk using AE signal [13], (b) schematic of AE and frictional force vs. test time for a-C:H films delamination [14].

1.2.3 Luminescent spectroscopy

Monitoring the wear life of the coating through luminescent spectroscopy has been systematically studied and proposed for monitor the wear life of thermal barrier coatings (TBC) [15]. Thermal barrier coatings are multilayer systems, which consist of the thermally grown aluminium oxide layer (TGO) formed on the aluminium containing metallic bond coat. The top of the TGO layer is a thermal barrier coating, which commonly is yttria stabilised zirconia (YSZ) or gadolinium zirconate ($Gd_2Zr_2O_7$). The failure mode of the TBC is generally spallation and delamination, especially close to the interface with the TGO layer. In cases where the spall regions are fairly large, they can be seen visually. However, when the spall regions are smaller, they can be visualised by the luminescent spectroscopy. The concept is shown in Fig. 1.3(a) and consists of the sensing layer located adjacent to the TGO and bond coat, in which this layer is buried under the topcoat and can be probed with the laser wavelength to which the coating is transparent. When the topcoat is spalled away or has been eroded, the sensing layer is fully exposed and can be illuminated with a laser excitation. This indicates that the wear sensing capability by this technique does not depend only on the failure mode of the coatings, but also the degree to which the excitation laser energy is absorbed by the top layer.

Recently, there has been a study on applying this technique to monitor the wear life of molybdenum disulphide (MoS_2) tribological coating [16]. The coating structure is shown schematically in Fig. 1.3(b), in which erbium (Er) and samarium (Sm) doped yttria stabilised zirconia (YSZ) layers are used as sensor materials. Wear-sensing capability of the coatings was also demonstrated by measuring the luminescence spectra at the wear track before and after the wear test at a certain test cycles. It was found that after the wear test at 10,000 cycles has reached, the luminescent spectrum matched with the spectrum

line of the Er doped YSZ layer (shown in the inset) as shown in Fig. 1.3(c). This spectrum is observed up to about 25,000 cycles, but its intensity was rapidly reduced until it was no longer detectable after approximately 30,000 cycles. No sensor spectra were detected until approximately 150,000 cycles, in which the spectrum matched again with the Sm doped YSZ layer (shown in the inset) as can be seen in Fig. 1.3(d).

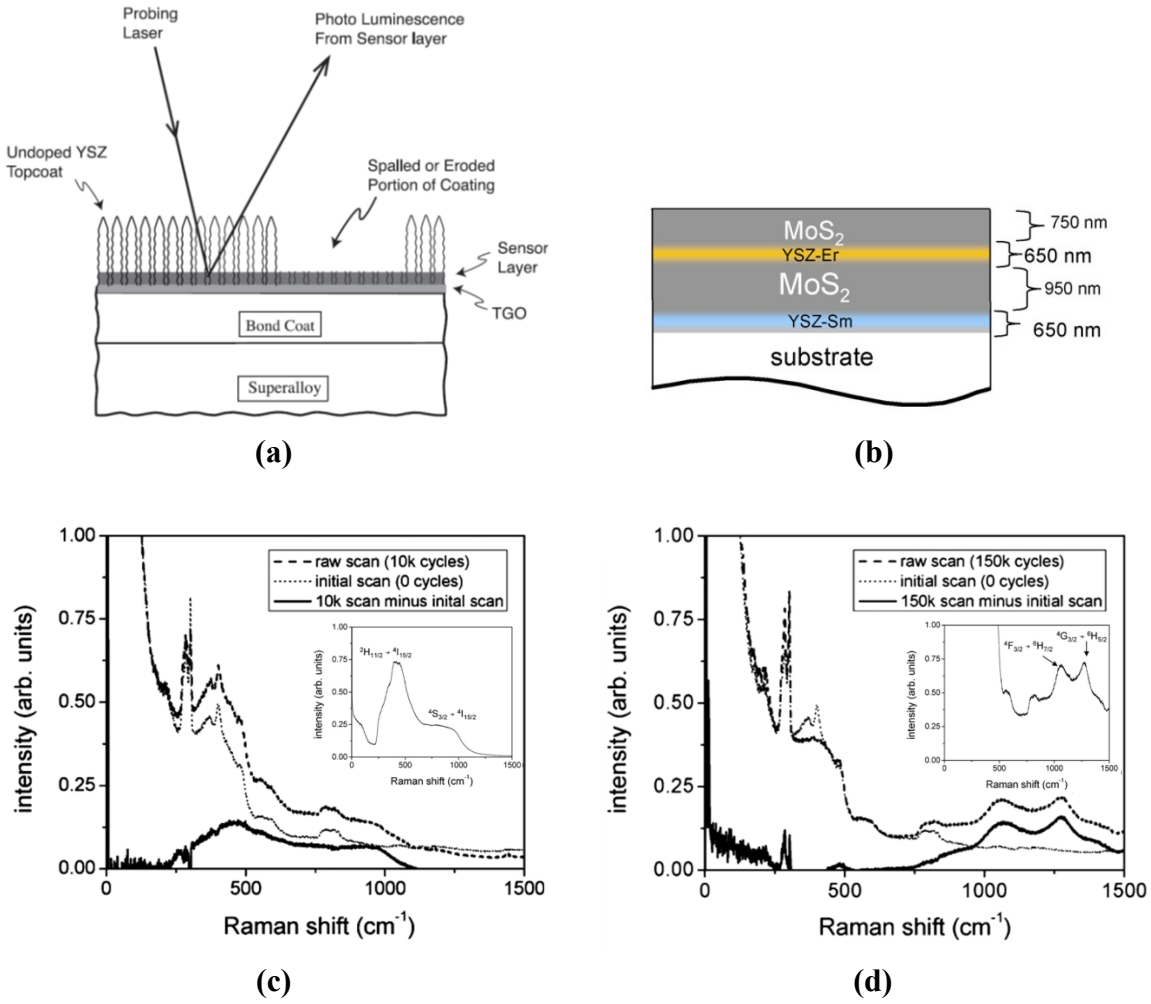

Fig. 1.3 (a) Schematic diagram of the concept of wear monitoring of the thermal barrier coating by luminescent spectroscopy [15], (b) schematic diagram of multilayered MoS_2 coatings with imbedded luminescent (Doped YSZ) wear-sensing layers, (c) optical spectra from the wear track after a wear test at 10,000 cycles and (d) at 150,000 cycles [16]

1.3 Amorphous carbon (a-C) films

1.3.1 Structure and classification of a-C films

Amorphous carbon (a-C) films are commonly accepted as the hard coatings that have similar mechanical, optical, electrical and chemical properties to diamond, but do not have a dominant crystalline structure. Due to the non-crystalline structure, a-C films are smooth and conform to surface roughness of the substrate. In addition, amorphous carbon films can be deposited at room temperature. Because of these and other advantages, a-C films have been attractive for numerous industrial applications.

Carbon can form a variety of both crystalline and amorphous structures because it can form the bonds in three hybridisations, namely, sp^3, sp^2 and sp^1 as shown in Fig. 1.4 [17]. In diamond, carbon has four sp^3 hybridised orbitals, which contribute to the formation of strong covalent σ bonds in tetrahedral structure with four adjacent carbon atoms. In graphite, carbon forms trigonally sp^2 hybridised orbital with covalent σ bonds to the nearest three carbon atoms in plane. Each plane is attracted to one another by weaker π bond to produce a layer structure of graphite. In sp^1 hybridisation, two carbon atoms form a covalent σ bond, while other two atoms form π bonds lie in vertical direction. Amorphous carbon films contain a certain mixture of sp^3 and sp^2 hybridised carbon atoms. Typically, trace amounts of sp^1 bonding are also feasible, but relatively low as it can be neglected when comparing with sp^3 and sp^2 hybridisations in the bulk of total bonds.

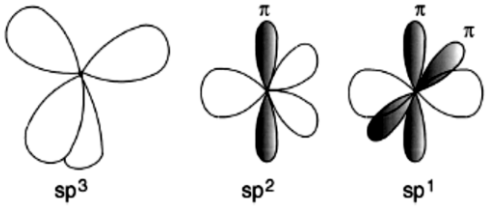

Fig. 1.4 The sp^3, sp^2 and sp^1 hybridised bonding [17]

An a-C film can be classified into several groups, depending on the relative amount of sp^3 and sp^2 hybridised carbons and hydrogen content. The films with a high proportion of sp^2 hybridised carbon atoms are relatively soft and behave more like graphite during tribological tests, while the films with more sp^3 hybridised carbons are more like diamond, and hence they are hard and provide attractive tribological properties. If the films are prepared from a decomposition hydrocarbon source or with the introduction of hydrogen gas during deposition, then a significant amount of hydrogen are also present within the film structures. The compositions of various forms of a-C film were simply displayed by a ternary phase diagram as shown in Fig. 1.5 [18,19]. The three corners correspond to diamond, graphite and hydrogen, respectively. There is an excluded region at high H contents, where molecular solids cannot form. The familiar forms of non-crystalline carbon such as glassy carbon and evaporated a-C lie in the sp^2 corner. Sputtering methods produce hard but predominantly sp^2 bonded a-C. If the fraction of sp^3 hybridised carbon reaches a high level, the films are regarded as tetrahedral a-C (ta-C). The interior of the diagram, where the a-C:H or hydrogenated a-C films with some amounts of hydrogen contents are located. Although an a-C:H film is industrially called diamond-like carbon (DLC), it is seen that the sp^3 content is actually not so large, but hydrogen content is rather large. However, a-C film is called ta-C:H or ta-DLC when the sp^3 bonded carbon content increases with less hydrogen.

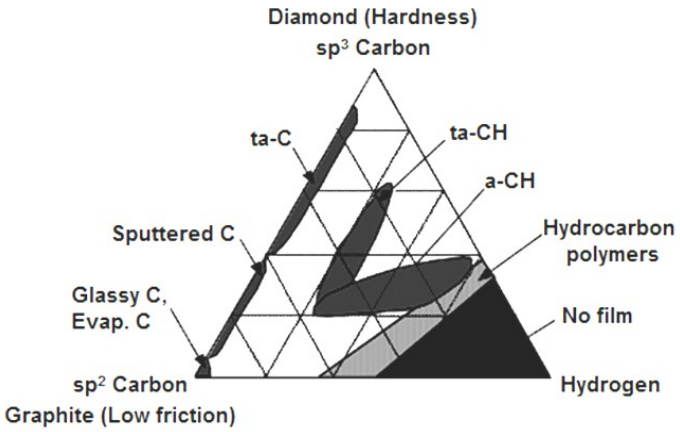

Fig. 1.5 Ternary phase diagram of various a-C films with respect to their sp^2, sp^3 and hydrogen contents [19]

1.2.2 Deposition of a-C films

Currently, a-C films can be deposited by several methods, including both chemical vapour deposition (CVD) and physical vapour deposition (PVD) as illustrated by schematics shown in Fig. 1.6 [17].

In chemical vapour deposition (CVD), the most popular deposition method is plasma-enhanced chemical vapour deposition (PECVD). The main feature of this technique is that a hydrocarbon gas is decomposed or dissociated in a plasma using D.C. or R.F. excitation between parallel electrodes as illustrated in Fig. 1.6(a) [20,21]. The substrates have to be at a negative bias relative to the plasma to achieve ion bombardment against the growing film. The films derived from such hydrocarbon gases contain not only carbon but also considerable amount of hydrogen in their microstructure. The films deposited by this technique are often referred to as hydrogenated a-C film (a-C:H). The amounts of hydrogen contents in the films vary widely with several factors, such as type of hydrocarbon gas [22] and substrate bias voltage [23,24].

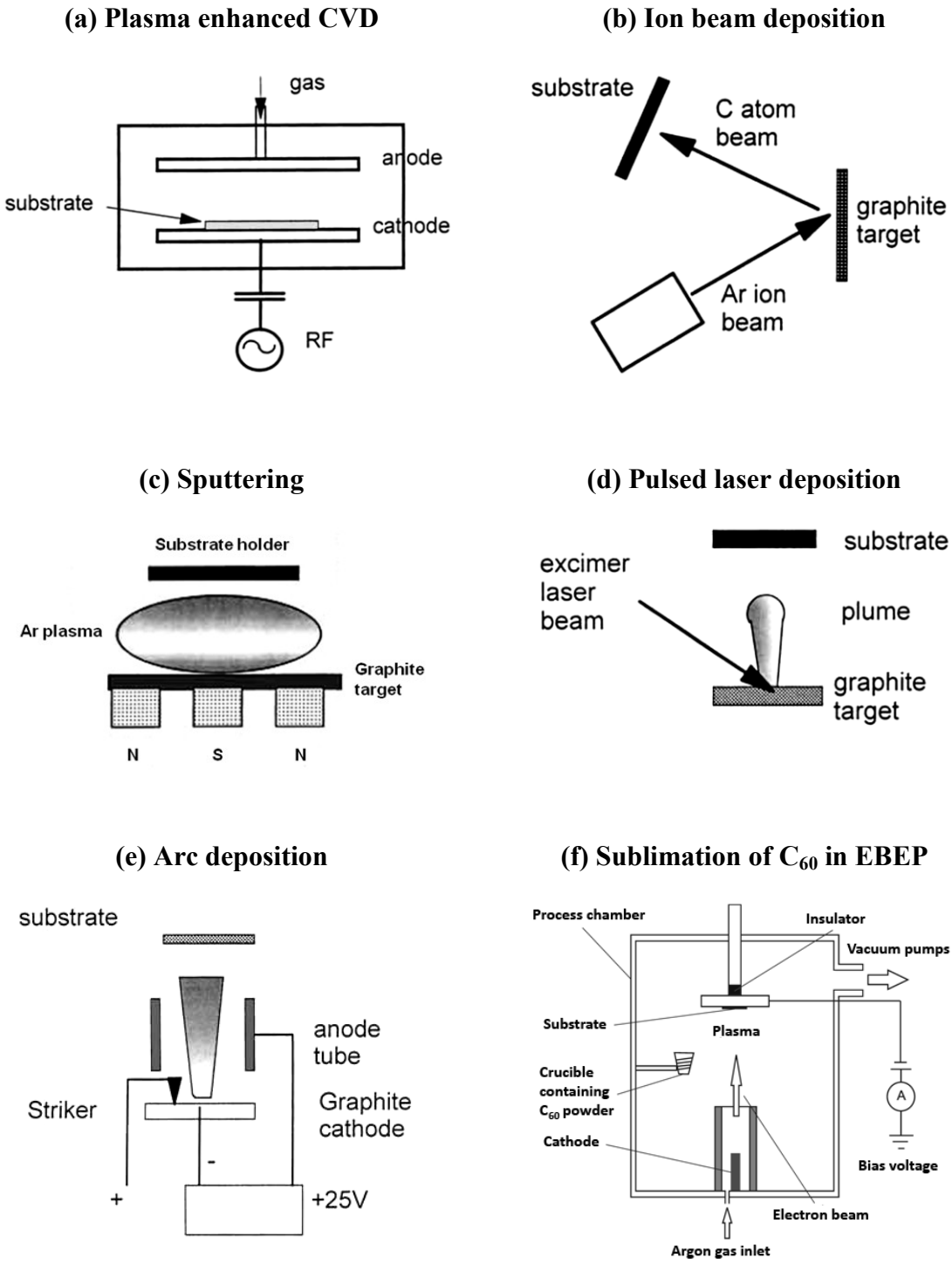

Fig. 1.6 Schematics of various deposition systems for a-C films [17,33]

In physical vapour deposition (PVD), a solid carbon, such as graphite or fullerene, is used as a carbon source. PVD method is preferable for deposition of non-hydrogenated a-C film, resulting in harder film than that deposited by PECVD method. The existent PVD methods for deposition of a-C films are as followed;

- *Ion beam deposition*

The first a-C films were prepared by ion beam deposition [25]. The feature of this technique is that the a-C film is condensed from a beam of carbon ions with the energy of few tens eV up to hundred eV. The impact of these ions on the growing film can physically induce the formation of sp^3 bonding. Carbon ions are produced by sputtering of graphite cathode in an ion source [26] as shown in Fig. 1.6(b). The carbon ions are then accelerated to form the ion beam in a vacuum deposition chamber.

- *Sputtering*

In the sputtering process, as shown in Fig. 1.6(c), the growing film is mainly bombarded by sputtered neutral target atoms with energies of up to 10 eV, and by reflected neutral plasma gas atoms, usually argon, with energies close to the applied voltage. The intensity of this bombardment is determined by the growing conditions. The film deposition resulting from sputtering of a solid carbon target by Ar ions includes three phases: 1) the bombardment of the target by the ions leading to sputtering of target atoms and eventual backscattering and charge neutralisation of the ions, 2) the travelling of sputtered particles and scattering ions through the plasma gas, and 3) their arrival at the substrate. Through energy and momentum transfer, the arriving particles induce modifications of the microstructure of the growing film [27,28].

- *Pulsed laser deposition*

In pulsed laser deposition, the pulsed intense photon energy is focused onto the surface of graphite target located in the vacuum chamber. The impact of the laser radiation on the target results in various complicated processes, including, absorption, melting, evaporation, plasma generation and expansion of the plasma to the substrate as displayed in Fig. 1.6(d). The kinetic energy of the carbon species is proportional to the laser fluence, in which typically high enough to induce the hard ta-C film with high fraction of sp^3 bonded carbons and low hydrogen content [29].

- *Arc deposition*

In this technique, as presented by Fig. 1.6(e), the arc discharge current is concentrated at the cathode surface, forming non-stationary locations or cathode spots of extremely high current density of order 10^{12} A/m^2. The high current density is associated with an extremely high area power density of order 10^{13} W/m^2, which in turn provides the conditions for the localised phase transformation from the solid (cathode material) to a fully ionized plasma [30]. The spot is formed by an explosive emission process, which can also create an undesired particulates or droplets. The particulates can be filtered by several ways [31]. However, this technique can produce highly ionised plasma with energetic species of 30-150 eV, a fairly narrow ion energy distribution [32].

- *Sublimation of fullerene in electron beam excited plasma*

This technique has been recently developed for deposition of a-C film with high density and hardness at high deposition rate and smooth surface [33,34]. As can be seen in Fig. 1.6(f), fullerene powder is sublimated in high density electron beam excited plasma and decomposed into minute carbon species. By applying negative voltage to the substrate,

these carbon species are propelled toward and form dense a-C film on substrate by means of collision and transferring momentum with the energetic Ar ions as well as Ar bombardment to the growing film.

The major properties of a-C films deposited by various methods as described above are summarised in Table 1.1. Due to the nature of each deposition method, the properties of a-C films vary a great deal with it. Furthermore, depending on the method being used, the deposition parameters can be varied over broad ranges, which have to be optimised in order to obtain the properties tailored to the applications.

Table 1.1 Some major properties of various a-C films as well as diamond and graphite [29,33,35]

Material	Preparation technique	Density (g/cm^3)	sp^3 (%)	Hardness (GPa)	Elastic modulus (GPa)
Diamond	Bulk	3.52	100	100	1050
Graphite	Bulk	2.27	0	n/a	n/a
a-C:H	PECVD	1.2-2.2	40-60	10-20	145
a-C	Ion beam	1.8-3.5	n/a	32-75	n/a
a-C	Sputtering	1.9-2.4	2-5	11-24	140
a-C	EBEP	n/a	n/a	12-28	n/a
ta-C	PLD	2.4	70-95	30-60	200-500
ta-C	Arc deposition	2.8-3.0	85-95	40-180	500

Generally, a-C films can be deposited onto many kinds of substrates, but the ability to establish strong adhesion to the substrates can be varied depending on the chemical nature of the substrates. Typically, a-C films form strong adhesion with the carbide- and silicide-forming substrates such as Si, Ti, W and Cr [36]. On the other hand, the adhesion

of a-C films to metallic and ceramic substrates may not be strong, but it can be improved by the addition of bonding or intermediate layer prior to deposition of a-C film. Ideally, the deposition of intermediate layer is carried out in the same deposition chamber. The intermediate layers are also typically selected from the elements that can form a strong carbide- or silicide-compound such as Si, Ti, Cr and W. These elements can chemically react with the atoms of substrate and insure the strong bonding [37-40].

Another feature of a-C films is that they often develop residual compressive stress regardless of the deposition method. The internal stress up to 4 GPa has been measured for a-C:H, while in ta-C even higher stress up to 12 GPa could be obtained [41]. Traditional explanation for the presence of the large internal stress is based upon the assumed sub-implantation mechanism of the growing film by the energetic carbon species bombardment [42]. If the compressive stress is too large to be supported by the adhesive force binding the film and substrate, the films are susceptible to delamination and spalling resulting in the formation of buckling or wrinkle surface topography [43]. The adhesion problem due to the high compressive stress can also be improved by addition of intermediate layer as similar as the already mentioned previously. Another method to reduce the internal stress of a-C films is doping some elements, such as Si, Ti or Cu into a-C films [44].

1.4 Friction and wear of a-C films

The physical and mechanical properties of a-C films make them good candidates for a variety of wear resistant and low friction coatings. Nevertheless, the understanding of their friction and wear properties of a-C films is still required for improvement or expanding the use of a-C films for the tribological applications. The tribological behaviour

of a-C films may vary a great deal from one type to another. In particular, the coefficient of frictions (COF) reported for various types of a-C films span in the wide range 0.007-1.0 [45,46]. It has already been described briefly in section 1.1 that the friction and wear of tribolgical coatings are influenced by two main factors, namely intrinsic and extrinsic factors. In this section, the influences of these factors on the tribological characteristics of a-C films are described as followed;

1.4.1 Intrinsic factors

The intrinsic factors that control friction and wear properties of a-C films are mainly by their nature, for example, the fraction of sp^3, sp^2 bonded carbons as well as the relative amounts of hydrogen and/or other doping or alloying elements in the structure.

The fraction of sp^3 and sp^2 bonded carbons as well as the amount of hydrogen content in a-C structure varies in the wide range depending on the deposition method as described in the previous section and summarised in Table 1.1. Within the same deposition method, the properties of a-C films can also be varied as the deposition parameters are changed. In general and ideal aspect, ta-C coating is harder, denser and more stable by nature due to the high sp^3 bonding and therefore it shows better wear resistance compared to the a-C:H and a-C film [47,48].

In conventional tribological coatings, several types of coating structure are existed as shown in Fig. 1.7 [49]. Most commercial a-C films are made up of single layer containing one structure phase. Recently, the multi-component structure of a-C films, i.e., by doping or composite, has become another choice to provide much improved physical, mechanical and tribological properties. For example, by addition of tungsten (W) with only 2-5 at.%, reduction of friction up to 50% has been observed [50]. In case of multilayer or gradient structure of a-C films, although the main purposes are to improve

the adhesion strength between a-C film to the substrate and reduce the intrinsic stress of a-C films [51,52], these kinds of design can also affect to the friction and wear of a-C films.

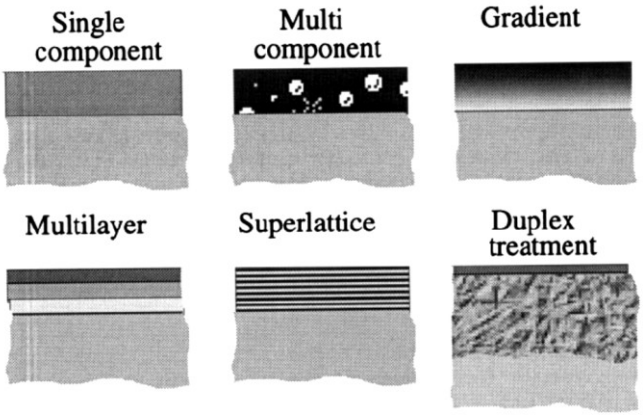

Fig. 1.7 The various structures of conventional tribological coatings [49]

1.4.2 Extrinsic factors

Extrinsically, friction and wear properties of a-C films are influenced by the physical, chemical and mechanical interaction between the rubbing surface of a-C films and their surroundings. In general, they are dependent on, for example, substrate nature, counterface materials, applied load, sliding velocity, environment, etc.

- *Effects of substrate nature*

Experimentally, mirror-polished silicon wafers (Si-wafers) are typically used as the substrate because of the surface smoothness, adhesion, and mechanical strength of Si-wafers. Practically, however, several types of substrate materials have been used, for example, aluminium, titanium and their alloys [53,54], steel, and some ceramics substrates

such as SiC, Si_3N_4, ZrO_2 and SiO_2 [55,56]. As described in the previous section that a-C films adhere well to the silicide- or carbide- forming substrates, a-C films can be deposited directly onto those substrates. In case of other types of materials, the intermediate layer is needed for adhesion improvement and consequently improved friction and wear properties [57].

Another concerning to the nature of substrate is the mechanical properties of substrate. Since a-C films are hard and high elastic modulus, the substrate should ideally have similar properties to the films. When the load is applied to the coating system, deformations of the film and substrate are occurred. The substrate should provide enough deformation in order to maintain the integrity of the film and substrate, otherwise the high wear rate of the films can be occurred [58]. An example of the film failure when it is deposited onto the softer substrate, such as aluminium alloy, is presented in Fig. 1.8 [59]. The a-C:H film deposited on aluminium alloy without any interlayer is removed completely, but the film with a 0.5 μm thick silicon interlayer did not fail after the same period of wear test. Furthermore, a deep wear groove could be observed indicating plastic deformation of the substrate.

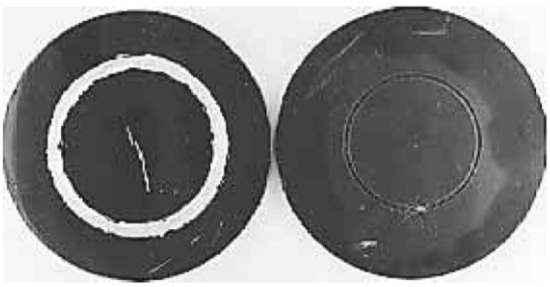

Fig. 1.8 The influence of an intermediate layer on durability of a-C:H films deposited on aluminium alloys [58]

- *Interaction with counterface material*

The interaction between a-C films with the sliding materials is correlated to the presence of material transferred layer on the counterface material surface [60,61]. Further analysis has revealed that the transfer film has disordered graphite-like or disordered graphitic structure, which can be accounted for the reduction of coefficient of friction (COF). In addition, the counterface materials that are known to be able to form carbides (Ti, Si, W, Fe, Al) tend to generate such layer faster with higher degree of coverage and strong bonding. Conversely, non-carbide formers (such as Cu) may not form a strongly bonded layer on their sliding surface, resulting in the higher COF is obtained [62]. It has been found that, the COFs of a-C:H films sliding against stainless steel, Al_2O_3, Si_3N_4, SiC balls in ambient air with 30-36% RH are in the range of 0.1-0.15 with observable transferred layers on the ball surfaces [63]. However, the higher wear rate of a-C:H film was observed when it was rubbed against harder sliding materials as can be seen in Fig. 1.9.

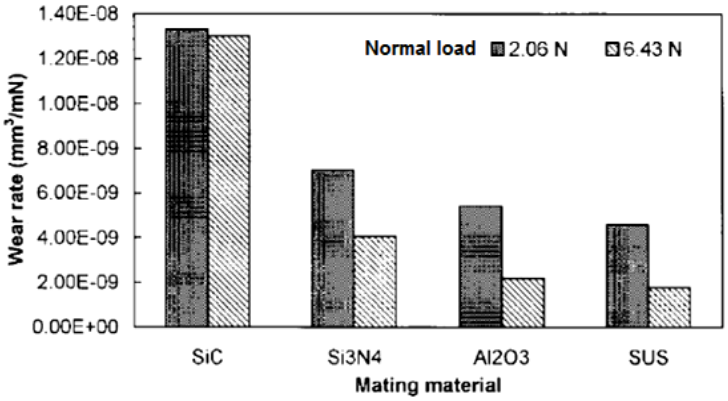

Fig. 1.9 The wear rates of a-C:H films in sliding against different counterface materials and loads [63]

- *Effects of sliding velocity and applied load*

The sliding velocity and the applied load influence the friction and wear of a-C films. For the a-C:H films, the higher applied load and velocity enhances the graphitisation process and therefore influences the friction behaviour. The higher sliding velocity increases the contact frequency and the rate of temperature rise that facilitates the release of hydrogen atoms from the sp^3 structure. Higher loading enhances the shear deformation and transformation of the weakened hydrogen- depleted a-C:H structure into graphite. As a result, the COF of a-C:H has found to decrease as the applied load and sliding velocity increase as shown in Fig. 1.10(a) [48,64]. In contrast to a-C films, as shown in Fig. 1.10(b), the COF of ta-C films is more stable over the wide range of sliding velocities and normal loads. Due to the more stable structure of the hydrogen-free ta-C film, which is highly sp^3 bonded, the shear deformation of the structure and its transformation into the graphitic structure requires more energy compared to the a-C:H coating [48]. Nevertheless, higher wear rate is found to be a consequence of increasing both of sliding velocity and applied load [65].

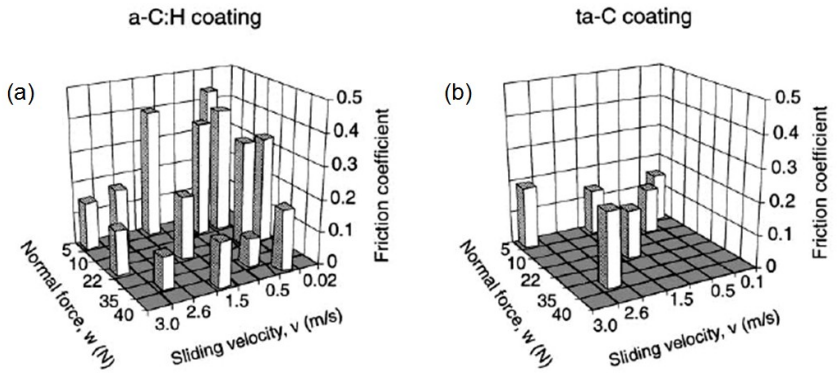

Fig. 1.10 The coefficient of friction values at the end of the tests for (a) a-C:H coating and (b) ta-C coating sliding against stainless steel [48]

- *Effects of environment*

The test environment can have a dramatic effect on the friction and wear of a-C films. In a dry air or inert atmosphere (nitrogen or argon), the COF of a-C:H is as low as 0.003, while the COF of ta-C or hydrogen-free a-C films is 0.7 as shown in Fig. 1.11. However, in humid air atmosphere, the COF of a-C:H is slightly increased to 0.06, while the COF of ta-C is significantly reduced to 0.25 [66-68]. The low friction performance of a:C:H films in dry and inert environments has been attributed to the hydrogen-terminated dangling bonds with weak van der Waals forces acting in the contact between surfaces. In the humid environment, this mechanism will be disturbed by water vapour molecules, which can give rise to capillary forces that increase friction. However, this mechanism is beneficial to the ta-C films, in which the free σ bonds of surface carbon atoms of ta-C film are passivated by water molecules and/or oxygen in air. Even if some of the bonds may have been exposed due to wear and/or thermal desorption, they are instantly re-passivated by these molecules. As a result, the COF of ta-C films became relatively low as soon as moist air was introduced into the test chamber.

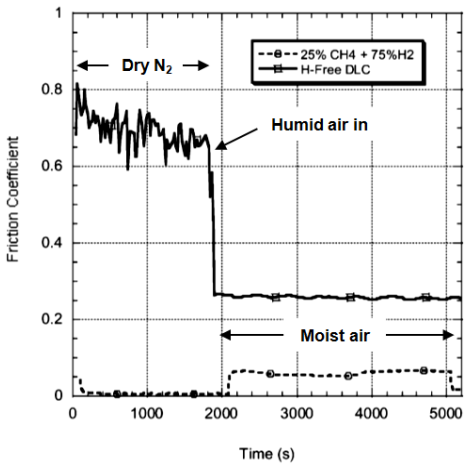

Fig. 1.11 Effect of atmospheres on the friction characteristics of a-C:H and ta-C films [66]

1.4.3 Tribological applications of a-C films

The excellent sliding friction and wear resistance of a-C films makes them good candidates for a variety of tribological applications, typically as wear-resistant protective coatings for metals, optical, or electronic components. The applications of a-C films can be divided into two categories – firstly those based essentially on the undoped single layer of a-C films and secondly those consisting of a-C films with additions of other elements [69]. The former tend to be used when the contact pressures, shear stresses are relatively low and when the heat generated is low. The examples of such applications are found in knives used in the textile industry, dies used in the extrusion of polystyrene for the packaging industry and even in razor blades. For the high contact pressure or shear stress applications, a-C films with intermediate layer and doped a-C films are typically used. Such applications include automotive, aerospace and machinery, such as aircraft landing gear, ball bearing inner races or cages, compressor screws, machining tools and automobile engine components [70-73].

1.5 Potential wear monitoring technique for a-C films

From the proposed wear monitoring techniques for tribological coatings as reviewed earlier, some conclusion remarks regarding the applicability for a-C film should be clarified.

The resistivity measurement technique is applicable for real-time measurement, in which the monitoring can be carried out continuously without interrupting the system during the wear test. In addition, this technique is well applicable for the highly conductive thin films. However, a-C films are generally characterised by high electrical resistivity, in which the values spanned a wide range of 10^{6}-10^{16} Ω.cm [74,75]. In addition, this

technique is limited to the coated parts that are static because the electrical wiring connected to the coating is necessary. Typically, a-C films are applied to the movable parts as the examples given in the section 1.4.3. Therefore, it is apparent that the applicability of this technique to monitor the wear life of a-C films has been limited by the nature mismatch between the technique and characteristics of a-C films.

The real-time analysis can also be accessed by acoustic emission (AE) analysis. However, AE technique seems to be more applicable than the previous technique because it is not limited to the materials that have specific properties. In addition, it is highly sensitive to the damage or failure of the coating. Although this technique has been applied to monitor the wear life of a-C films [14], the sensing capability is limited to only when the film is completely or slightly before failure. In addition, due to the high sensitivity to the damage or failure, the unpleasant signal originated from either substrate or counterface material can be generated and influences the precision of analysis [76].

Luminescent spectroscopy technique has the advantages not only similar to those of the former techniques, but also the signal detected from the coating that is completely isolated from the counterface material and substrate because the luminescent signal can be detected only from the coating section. In addition to this advantage, the wear-sensing capability of this technique does not depend only on the failure mode of the coatings, but also the degree to which the excitation laser energy is absorbed by the top layer. This means that a material which strongly absorbs the laser will have a reduced minimum remaining thickness above the sensing layer at which the luminescence can be activated. This minimum thickness strongly depends on the optical absorption characteristics of the top layer.

Comparing the optical absorption characteristics between MoS_2 that has been used as a tribological layer in the previous review [16] with a-C films, as shown in Fig.

1.12, it is found that MoS_2 has high absorption coefficient to the laser excitation (532 nm or 2.33 eV) [77], which meant that the effective optical penetration depth of the laser was small. Thus the sensing was possible only when the MoS_2 layer has almost worn out until the sensing underlayer appeared. The a-C films have relatively lower absorption coefficient [78] at the same wavelength, which means the penetration of light is higher. Furthermore, due to the high internal stress of the as-deposited a-C film, especially non-hydrogenated type, the thickness is limited to several hundred nanometres. This has led to the possibility that the luminescence from the wear sensing layer can be detected even though the a-C layer is not completely worn out. That is, the detectable luminescence from an incompletely worn a-C layer enables the user to estimate the remaining thickness of the coating, which makes the wear monitoring of a-C film more reliable.

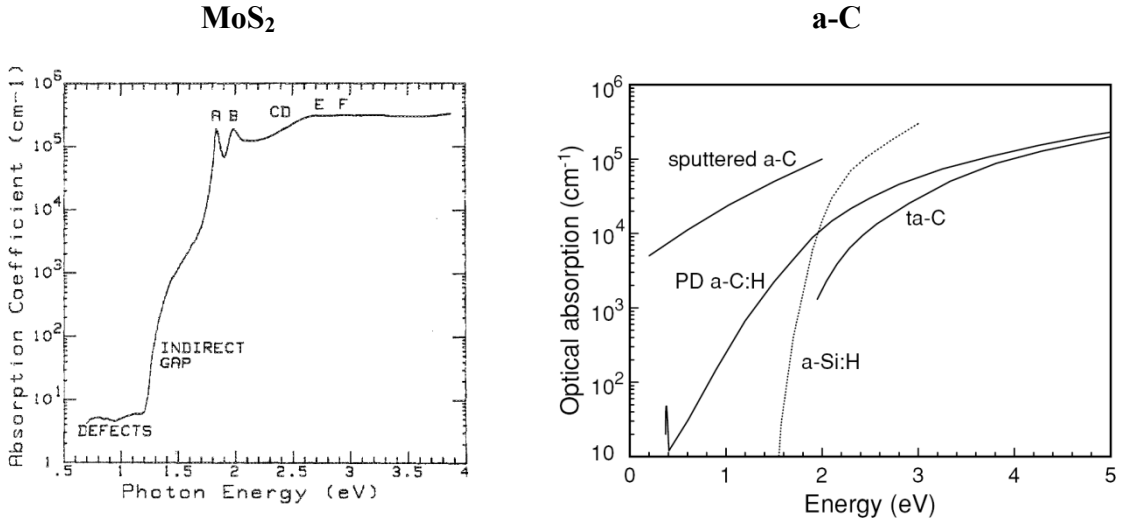

Fig. 1.12 Optical absorption coefficients spectra of MoS_2 and a-C films [77,78]

Another factor that influences the sensing capability is the luminescence intensity. The desired layer should give the strong luminescence and has high sensitivity. Among the existent oxide- and sulphide-based luminescent materials, it has been found that the luminescent properties of ZnS-based materials have gained more interesting for over a century. These materials exhibit several classes of luminescence classified by the types of excitation, such as, cathodoluminescence (CL), electroluminescence (EL), photoluminescence (PL), mechano or triboluminescence (ML or TrL), etc. These have led to the various applications of ZnS materials, especially, in optoelectronic devices, infrared (IR) coatings and scintillators [79,80].

In each class of luminescence mechanism, it has been also found that the luminescence efficiency, which is referred to the ratio of the luminescence energy to the absorbed excitation energy, of ZnS-based materials is higher comparatively with some other luminescent materials as can be given by the examples of CL efficiency (η) [81] and luminescence efficiency as excited by X-ray [82] for some luminescent materials as summarised in Table 1.2. In addition, it has also been found that ZnS-based materials exhibit stronger TrL than other groups of luminescence materials [83] as shown in Table 1.3. Due to these criteria, ZnS-based materials have been primary selected for studying the applicability as the wear sensing layer for wear monitoring of a-C films.

Deposition of a-C films onto ZnS materials has been found to be feasible and the a-C films have been evaluated as protective coatings for ZnS infrared transmitting windows from corrosion [84]. In addition, it has been also reported that the infrared transmission of ZnS coated with a-C film was still as high as 90% [85].

Table 1.2 Energy conversion efficiencies (η) of some typical luminescent materials [81,82]

Material	η_{CL}	$\eta_{excited\ by\ X\text{-}ray}$
ZnS:Ag	0.23	0.20
ZnS:Cu	0.19-0.21	0.17
CaS:Ce		0.22
CaS:Mn		0.16
La_2O_2S:Eu		0.12
Y_2O_2S:Eu	0.13	
Y_2O_3:Eu	0.08	0.07
Zn_2SiO_4	0.08	

Table 1.3 Triboluminescence (TrL) of various materials [83]

Group	**Sample**	**TrL intensity (cps)***
Hexagonal	ZnS	60
	ZnS:Mn	2800
	ZnS:Cu	1100
	Zn_2SiO_4:Mn	57
	ZnO	3
	SiC	4
X_2O_3 (X: Al or Y)	Al_2O_3	10
	Al_2O_3:Mn	60
	Y_2O_3	9
	Y_2O_3:Eu	20
MA_2O_4	$MgAl_2O_4$	31
	$CaAl_2O_4$	14
	$SrAl_2O_4$	36
Fluorite	ZrO_2	8

*TrL intensity was measured as a function of friction applied to the material by a brass rod of 1 mm diameter under a load of 5 N and slide speed of 6.3 cm/s.

1.6 Objectives of this research

It has been shown in the previous reviews that the friction and wear of a-C films, which are extremely promising tribological coating materials, depend strongly on both intrinsic and extrinsic factors. The intrinsic factors, such as microstructure, fraction of sp^3, sp^2 hybridised carbon bonds and H content, are easily controlled by a proper design and selection of deposition process. In contrast, the extrinsic factors, especially, applied load, sliding speed and service environment, are more difficult to be controlled because they are not perfectly constant when the coatings are applied to the actual service. As a result, a pre-mature failure of the coating and/or pre-replacement of the parts before coating failure can occasionally occur. In order to avoid the unexpected failure or uncertainty of the coated parts, it is industrially important to develop a wear monitoring method that provides the information of indication of remaining coating life and sufficient warning before failure.

Based on the proposed technique for wear monitoring of protective coatings as already explained in the section 1.2, the luminescent spectroscopy technique has been found to be more adaptable and more beneficial technique comparing with other two remaining methods, i.e., resistivity measurement and acoustic emission analysis. This technique is not only be able to monitor the wear life in real-time and able to be used with various kind of coating, but it can also allow the user to determine the state of the coating before the failure. This technique has been applied to monitor the wear life of the MoS_2 tribological coating [16], it was found that MoS_2 had high absorption coefficient to the laser excitation [77], which meant that the effective optical penetration depth of the laser was small. Thus the sensing was possible only when the MoS_2 layer has almost worn until the sensing underlayer appeared. Amorphous carbon (a-C) films have relatively lower

absorption coefficient [78], which means the penetration of light is higher. This leads to the possibility that the luminescence from the underlayer can be detected even though the a-C layer is not completely worn out. That is, the detectable luminescence from an incomplete wear of a-C layer enables the user to estimate the remaining thickness of the coating, which allows the wear monitoring of the coating to be more reliable.

Therefore, the objectives of this research are to extend the concept of wear monitoring through luminescent spectroscopy technique to be applicable for a-C coating system. To achieve this applicability, a-C tribological coatings with luminescent wear-sensing underlayer are developed. The expected coating structure of a-C/ZnS-based underlayer is illustrated in Fig. 1.13. Due to the superior luminescent properties of the ZnS-based materials, they are primary selected as the wear-sensing underlayer. It can be in the form of either single layer or composite layer. In addition, a thin Si-intermediate layer can also be added between a-C layer and ZnS-based underlayer for adhesion improvement. Several a-C/ZnS-based coatings systems have been fabricated. Their basic physical, mechanical, luminescent and tribological properties are evaluated, and demonstration of wear-monitoring through luminescent spectroscopy technique is also carried out.

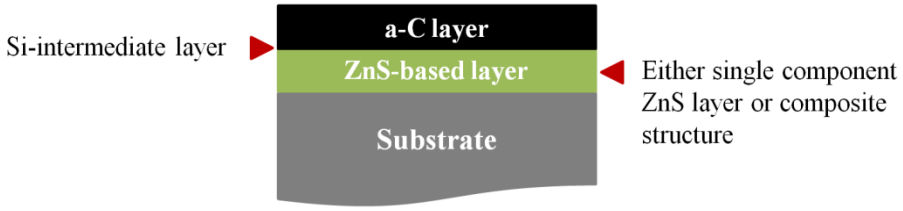

Fig. 1.13 An expected structure of a-C coating with luminescent ZnS-based underlayer

1.7 Structures of thesis

Throughout this study, it can be divided into five chapters composing in this thesis as followed;

Chapter 1 is an introduction that explains briefly about friction and wear of tribological coatings and the proposed wear monitoring techniques. An overview of a-C films, including their general features, deposition methods and their friction and wear characteristics towards the tribological applications is also presented. The potential technique for wear monitoring of a-C films is also discussed. Finally, the reason of selecting the luminescent spectroscopy technique and the research objectives are given.

Chapter 2 presents the fabrication and characteristics of the first coating system. The coating consists of a-C layer deposited on single layer structure ZnS:Mn underlayer fabricated by R.F. magnetron sputtering method.

Chapter 3 deals with the fabrication, characterisation and primary demonstration of wear-sensing capability of a second coating system. In this coating system, epoxy resin coating containing ZnS:Cu phosphor is used as the wear-sensing underlayer. The a-C films are deposited onto it by sublimation of fullerenes in electron beam excited plasma and pulsed vacuum are deposition.

Chapter 4 also copes with the fabrication, characterisation and demonstration of wear-sensing capability of the coatings, but on another a-C coating system. In this chapter, silica coating containing luminescent CdSe/ZnS quantum dots (QD) is used as the wear-sensing underlayer. The a-C film is deposited onto the silica/QD layer by R.F. magnetron sputtering method.

Chapter 5 is the summary of thesis, which includes the general conclusion of this research as well as the remaining issues and suggested further studies.

1.8 References

[1] K.H. Zhum Gahr : *Microstructure and wear of materials,* Tribology Series 10, Elsevier, (1987) 3.

[2] K. Miyoshi : *Solid lubrications: Fundamental and applications,* Marcel Dekker, (2001) 4.

[3] J.E. Sundgren and H.T.G. Hentzell : J. Vac. Sci. Technol. A, **4** (1986) 2259.

[4] C. Donnet and A. Erdemir : Tribol. Lett., **17** (2004) 389.

[5] R.F. Bushan and C.V. Deshpandey : Vacuum, **39** (1989) 955.

[6] K. Holmberg, A. Matthews and H. Ronkainen : Tribol. Int., **31** (1998) 107.

[7] F.W. Hahn Jr : Wear, **74** (1981) 157.

[8] K.G. Kreider and A.W. Ruff :, Surf. Coat. Tech., **86** (1996) 557.

[9] A.W. Ruff and K.G. Kreider : Wear, **203** (1997) 187.

[10] H. Luthje, R. Bandorf, S. Biehl and B. Stint : Sensor Actuator A, **116** (2004) 133.

[11] E. Kannatey-Asibu Jr and D.A. Dornfeld : Wear, **76** (1982) 247.

[12] Y.Z. Lee and K.H. Jeong : Wear, **217** (1998) 175.

[13] C.W. Cho and Y.Z. Lee : Surf. Coat. Tech., **127** (2000) 59.

[14] F.M. Kustas, J.N. Schwartzberg, S.H. Carpenter, C.R. Heiple and D.L. Armentrout : Surf. Coat. Tech., **67** (1994) l.

[15] M.M. Gentleman and D.R. Clarke : Surf. Coat. Tech., **188** (2004) 93.

[16] C. Muratore, D.R. Clarke, J.G. Jones and A.A. Voevodin : Wear, **265** (2008) 913.

[17] J. Robertson : Mat. Sci. Eng. R, **37** (2002) 129.

[18] W. Jacob and W. Moller : Appl. Phys. Lett., **63** (1993) 1771.

[19] J. Robertson : Pure Appl. Chem., **66** (1994) 1789.

[20] C.V. Deshpandey and R.F. Bunshah : J. Vac. Sci. Technol. A, **7** (1989) 2294.

[21] C. Serra, E. Pascual, F. Maass and J. Esteve : Surf. Coat. Tech., **47** (1991) 89.

[22] K.R. Lee, Y.J. Baik and K.Y. Eun : Diam. Relat. Mater., **3** (1994) 1230.

[23] J.W. Zou, K. Schmidt, K. Reichelt and B. Dischler : J. Appl. Phys., **67** (1990) 487.

[24] N. Xu, D. Yin, Z. Liu and X. Zheng : J. Phys. D: Appl. Phys., **30** (1997) 763.

[25] S. Aisenberg and R. Chabot : J. Appl. Phys., **42** (1971) 2953.

[26] F. Rossi, B. Andre, A. vanVeen, P.E. Mijnarends, H. Schut, M.P. Delplancke, W. Gissler, J. Haupt, G. Lucazeau and L. Abello : J. Appl. Phys., **75** (1994) 3121.

[27] J. Ullmann, G. Schmidt and W. Scharff : Thin Solid Films, **214** (1992) 35.

[28] E. Mounier and Y. Pauleau : J. Vac. Sci. Technol. A, **14** (1996) 2535.

[29] A.A. Voevodin and M.S. Donley : Surf. Coat. Tech., **82** (1996) 199.

[30] D.M. Sanders and A. Anders : Surf. Coat. Tech., **133** (2000) 78.

[31] P.J. Martin and A. Bendavid : Thin Solid Films, **394** (2001) 1.

[32] P.J. Fallon, V.S. Veerasamy, C.A. Davis, J. Robertson, G.A. Amaratunga, W.I. Milne and J. Koskinen : Phys. Rev. B, **49** (1994) 4777.

[33] H. Vaez-Taghavi and A. Hirata : Mater. Lett., **64** (2010) 83.

[34] H. Vaez-Taghavi and A. Hirata : Diam. Relat. Mater., **20** (2011) 1036.

[35] J. Robertson: Surf. Coat. Tech., **50** (1992) 185.

[36] A. Erdemir and C. Donnet : J. Phys. D: Appl. Phys., **39** (2006) R311.

[37] G. Capote, L.F. Bonetti, L.V. Santos, V.J. Trava-Airoldi and E.J. Corat : Thin Solid Films, **516** (2008) 4011.

[38] H. Ronkainen, S. Varjus and K. Holmberg : Wear, **222** (1998) 120.

[39] C.C. Chen and F.C.N. Hong : Appl. Surf. Sci., **243** (2005) 296.

[40] T. Takeno, T. Sugawara, H. Miki and T. Takagi : Diam. Relat. Mater., **18** (2009) 1023.

[41] G.A. Abbas, J.A. McLaughlin and E. Harkin-Jones : Diam. Relat. Mater., **13** (2004) 1342.

[42] Q. Wei, A.K. Sharma, J. Sankar and J. Narayana : Composites Part B, **30** (1999) 675.

[43] X.D. Zhu, K. Narumi and H. Naramoto : J. Phys.: Condens. Matter, **19** (2007) 236227.

[44] Q. Wei, R.J. Narayana, A.K. Sharma, J. Sankara and J. Narayan : MRS Symp. Proc., **498** (1997) 61.

[45] A. Grill : Surf. Coat. Tech., **94** (1997) 507.

[46] A. Gangopadhyay : Tribol. Lett., **5** (1998) 25.

[47] B.K. Gupta and B. Bhushan : Wear, **190** (1995) 110.

[48] H. Ronkainen, S. Varjus, J. Koskinen and K. Holmberg : Wear, **249** (2001) 260.

[49] S. Hogmark, S. Jacobson and M. Larsson : Wear, **246** (2000) 20.

[50] B. Podgornik, D. Hren and J. Vizintin : Thin Solid Films, **476** (2005) 92.

[51] J. Deng and M. Braun : Diam. Relat. Mater., **4** (1995) 936.

[52] B.H. Lung, M.J. Chiang and M.H. Hon : Mater. Chem. Phys., **72** (2001) 163.

[53] R. Wei, P.J. Wilbur, A. Erdernir and F.M. Kustas : Surf. Coat. Tech., **51** (1992) 139.

[54] A. Dorner, C. Schurer, G. Reisel, G. Irmer, O. Seidel and E. Muller : Wear, **249** (2001) 489.

[55] A. Erdemir, M. Switala, R. Wei and P. Wilbur : Surf. Coat. Tech., **50** (1991) 17.

[56] G. Zhang, L. Wang, P. Yan and J. Zhang : *Proceedings of CIST2008 and ITS-IFToMM 2008*, (2010) 816.

[57] O.L. Eryilmaz, J.A. Johnson, O.O. Ajayi and A. Erdemir: J. Phys.: Condens. Matter, **18** (2006) S1751.

[58] T. Staedler and K. Schiffmann : Surf. Sci., **482** (2001) 1125.

[59] A.K. Gangopadhyay, P.A. Willermet, W.C. Vassell and M.A. Tamor : Tribol. Int., **30** (1997) 19.

[60] A. Erdemir, C. Bindal, J. Pagan and P. Wilbur : Surf. Coat. Tech., **76** (1995) 559.

[61] Y. Liu, A. Erdemir and E.I. Meletis : Surf. Coat. Tech., **82** (1996) 48.

[62] E. Konca, Y. T. Cheng and A.T. Alpas : Diam. Relat. Mater., **15** (2006) 939.

[63] H. Liu, A. Tanaka and T. Kumagai : Thin Solid Films, **352** (1999) 145.

[64] Y. Liu, A. Erdemir and E.I. Meletis : Surf. Coat. Tech., **86** (1996) 564.

[65] A. Erdemir, C. Bindal, G.R. Fenske, C. Zuiker and P. Wilbur : Surf. Coat. Tech., **86** (1996) 692.

[66] A. Erdemir : Surf. Coat. Tech., **146** (2001) 292.

[67] J. Andersson, R.A. Erck and A. Erdemir : Wear, **254** (2003) 1070.

[68] H.I. Kim, J.R. Lincea, O.L. Eryilmaz and A. Erdemir : Tribol. Lett., **21** (2006) 53.

[69] H. Ronkainen : *Tribological properties of hydrogenated and hydrogen-free diamond-like carbon coatings,* VTT Publications, **434** (2001) 3.

[70] A. Matthews and S.S. Eskildsen : Diam. Relat. Mater., **3** (1994) 902.

[71] R. Hauert : Tribol. Inter., **37** (2004) 991.

[72] A. Vanhulsel, F. Velasco, R. Jacobs, L. Eersels, D. Havermans, E.W. Roberts, I. Sherrington, M.J. Anderson and L. Gaillard : Tribol. Inter., **40** (2007) 1186.

[73] G.W. Malaczynski, A.H. Hamdi, A.A. Elmoursi and X. Qiu : Surf. Coat. Tech., **93** (1997) 280.

[74] B. Meyerson and F.W. Smith : J. Non-Cryst. Solids, **35** (1980) 435.

[75] M. Chhowalla, J. Robertson, C.W. Chen, S.R.P. Silva, C.A. Davis, G.A.J.

Amaratunga and W.I. Milne : J. Appl. Phys., **81** (1997) 139.

[76] M. Lohr, D. Spaltmann, S. Binkowski, E. Santner and M. Woydt : Wear, **260** (2006) 469.

[77] C.B. Roxlo, R.R. Chianelli, H.W. Deckman, A.F. Ruppert and P.P. Wong : J. Vac. Sci. Technol. A, **5** (1987) 555.

[78] J. Robertson : Semicond. Sci. Technol., **18** (2003) S12.

[79] M.Y. Nadeem, A. Waqas and M.F. Wasiq : Journal of Research (Science), **16** (2005) 105.

[80] P.F. Smet, I. Moreels, Z. Hens and D. Poelman : Materials, **3** (2010) 2834.

[81] L. Ozawa : *Cathodoluminescence and photoluminescence; theories and practical applications,* CRC press, (2007) 37.

[82] C.R. Ronda : *Luminescence; from theory to applications,* Wiley-VCH Verlag, (2008) 24.

[83] C.N. Xu, T. Watanabe, M. Akiyama and X.G. Zheng : Mater. Res. Bull., **34** (1999) 1491.

[84] F. Davanloo, T.J. Lee, D.R. Jander, H. Park, J.H. You and C.B. Collins : J. Appl. Phys., **71** (1992) 1446.

[85] G.F. Zhang and X. Zheng : Surf. Coat. Tech., **82** (1996) 110.

CHAPTER 2

AMORPHOUS CARBON COATINGS WITH ZnS:Mn UNDERLAYER

2. Amorphous carbon coatings with ZnS:Mn underlayer

2.1 Introduction

From the coating structure as proposed in Chapter 1, the coating structure consists of ZnS-based layer as a wear-sensing layer and amorphous carbon (a-C) layer as a top tribological layer. Initially, the luminescent ZnS-based layer should be fabricated. It has been found that several techniques can be used to fabricate ZnS coatings, for example, screen printing method [1], chemical bath deposition (CBD) [2,3], metal-organic chemical vapour deposition (MOCVD) [4,5], vacuum evaporation [6,7], pulsed laser deposition (PLD) [8,9] and sputtering method [10,11]. The strong and weak points of each technique depend on the applications of the final coating. For applications in the field of display panel or solar cell, screen printing, CBD, vacuum evaporation are the candidates due to their common strong points in the cost effectiveness, large area deposition. However, for the high quality with low contamination and well-controlled stoichiometric ZnS films, MOCVD, PLD and sputtering methods are more beneficial. More specifically, although the ZnS films obtained by MOCVD method have high crystallinity and high smoothness due to the nature of the thermal CVD process, high operating temperature is needed for decomposition of metal-organic compounds. In addition, the toxicity of the precursor can be the issue in case of environmental consideration. For the sputtering method, the high quality ZnS films with well-controlled stoichiometric and high growth rate could be obtained as similar as obtained by PLD method. Furthermore, sputtering method gains more advantages over the PLD in case of adhesion strength and smoothness of the final coatings. These qualities of the coatings are well known as the basic requirement for the coating applied in the tribological applications. These have led to the selection of sputtering process to fabricate the luminescent ZnS layer.

Deposition of a-C films can also be achieved by several techniques as already explained and summarised in Chapter 1. In general, a-C films are widely applied in the tribological applications. Most of the substrates are mainly the engineering parts. Besides, due to its infrared (IR) transparency, a-C can be used for optical applications, such as antireflective and scratch resistant wear protective coatings for IR optical materials, such as ZnS and ZnSe [12,13]. Furthermore, it has been also found that the adhesion between the ZnS substrate and the as-prepared DLC film is poor, but can be improved by the addition of Si or Ge intermediate layer [14]. Though these researches on deposition of a-C film have existed, all results mainly focused on the optical characteristics of the final coatings. The results on tribological characteristics have not been revealed yet.

In this study, a-C coatings with luminescent ZnS:Mn underlayer are fabricated. The luminescent ZnS:Mn layers are fabricated by R.F. magnetron sputtering method. To minimise the number of deposition process, a-C films are also deposited onto the luminescent ZnS layers by the same sputtering method. The coatings properties, such as physical, mechanical, tribological properties are analysed as well as the luminescent characteristics toward the wear-sensing capability is also investigated.

2.2 Experimental

2.2.1 Fabrication of ZnS:Mn layers

Manganese-doped zinc sulphide (ZnS:Mn) films were fabricated by R.F. magnetron sputtering method. The schematic diagram of the sputtering system is illustrated in Fig. 2.1. The target material is placed at the bottom of the chamber, which is connected to the vacuum pumps, R.F. power supply and argon gas flow controller. The ZnS:Mn films were prepared by sputtering from the hot-pressed ZnS:MnS target with the

amount of Mn 5 at.% onto Si-wafers, soda-lime glasses and sapphires. It was suggested that the luminescent property could be enhanced by thermal annealing at the optimum temperature of 700°C [11,15]. Therefore, the as-deposited films were subsequently annealed at this temperature for 60 min in an argon (Ar) atmosphere. The detail of fabrication processes and conditions are listed in Table 2.1.

Table 2.1 Process parameters for fabrication of ZnS:Mn layer by R.F. magnetron sputtering and post-annealing

Process	**Parameter**	**Corresponding value**
Chamber condition	Target	ZnS:Mn (Mn: 5 at.%)
	Plasma gas	Argon (99.995% purity)
	Base pressure (Pa)	Less than 1.5×10^{-3}
Plasma surface treatment of substrate	R.F. power (W)	100
	Pressure (Pa)	1
	Time (min)	10
Deposition of ZnS:Mn films	R.F. power (W)	50
	Pressure (Pa)	1
	Time (min)	60
	Electrodes distance (mm)	50
	Substrate temperature (°C)	Room temperature
Annealing	Temperature (°C)	700
	Time (min)	60
	Atmosphere	Argon flow
	Pressure (Pa)	+0.02 MPa

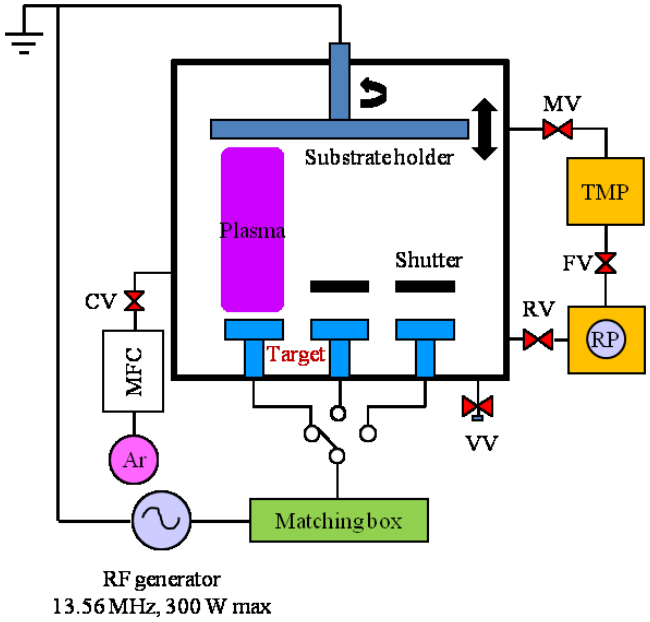

Fig. 2.1 Schematic diagram of the R.F. magnetron sputtering system

2.2.2 Deposition of amorphous carbon (a-C) films

Prior to deposition of amorphous carbon (a-C) onto the luminescent ZnS:Mn layer, the preliminary study on preparation of a-C films by sputtering method has been carried out to determine the deposition rate as well as physical and tribological properties. Amorphous carbon films were deposited onto Si-wafer and soda-lime glass by using the same R.F. sputtering method as shown in Fig. 2.1. The sputtering was carried out at R.F. power of 100 W for 60 min at several deposition pressures. The process parameters and conditions are summarised in Table 2.2. The obtained optimum condition was subsequently used for deposition of a-C films onto the luminescent ZnS:Mn layers.

Table 2.2 Sputtering conditions to determine the deposition rate of a-C films

Process	Parameter	Corresponding value
Chamber condition	Target	Graphite
	Plasma gas	Argon (99.995% purity)
	Base pressure (Pa)	Less than 1.5×10^{-3}
Plasma surface treatment of substrate	R.F. power (W)	100
	Pressure (Pa)	1
	Time (min)	10
Deposition of a-C films	R.F. power (W)	100
	Pressure (Pa)	10.0, 1.0 and 0.4
	Time (min)	60
	Electrodes distance (mm)	50
	Substrate temperature (°C)	Room temperature

2.2.3 Coating characterisations

Thickness of the coatings was measured with a scanning electron microscope (SEM) at the fractural surface. Structure of ZnS:Mn thin film was analysed with an x-ray diffractometer (XRD), while the structure of a-C film was analysed by Raman spectroscopy. Photoluminescence (PL) investigation of the coatings was carried out by irradiating with a UV lamp at the excitation wavelength of 365 nm. The PL spectrum was collected through an optical fibre to a polychromator connected with a multichannel analyser and a personal computer. Surface morphology of a-C coatings were observed with an optical microscope and an atomic force microscope (AFM). The tribological properties of the coatings were analysed with a ball-on-disk friction tester. The coatings were rubbed against stainless steel (SUS 440C) balls 4.8 mm in diameter with a normal force of 0.3 N. The rotational speed was 50 rpm, which corresponded to the sliding speed of 13 mm/s. The

test was carried out in ambient atmosphere. Finally, the hardness of the coating was measured by nanoindentation method.

2.3 Results and discussion

2.3.1 A preliminary study on deposition of a-C films by R.F. magnetron sputtering

The deposition rate of amorphous carbon (a-C) films deposited by R.F. magnetron sputtering at various argon pressures has been firstly determined. The films obtained from all conditions were deposited for 60 min. It is assumed that the thicknesses of a-C films increase linearly with time. Therefore, the deposition rate was determined by measuring the film thickness and then dividing by the deposition time. The results of both thicknesses measured by SEM at the fractural surfaces and corresponding deposition rates are presented in Table 2.3. It can be seen that the deposition rate increases as the argon pressure decreases.

Table 2.3 Thickness and corresponding deposition rate of a-C films deposited at various pressures measured by SEM at fractural surfaces

Pressure (Pa)	Thickness (nm)	Deposition rate (nm/min)
10.0	30	0.5
1.0	85	1.4
0.4	144	2.4

The optical microscopic images observed on the surfaces of the as-deposited a-C films are shown in Fig. 2.2. The a-C films deposited at the argon pressure at 10.0 and 1.0 Pa show the smooth surface without any cracks or defects formed on the surface as shown

in Fig. 2.2 (a) and (b), while the a-C films deposited the pressure of 0.4 Pa shows a buckling or wrinkle texture after being taken out from the process chamber for a few hours. The formation of the wrinkle is due to compressive stress relief. In most cases, the compressive stress is too large to be supported by the adhesive force binding the film and substrate, which gives rise to the buckling and delamination of films, even cracks [16,17]. However, no cracks were observed on the surface.

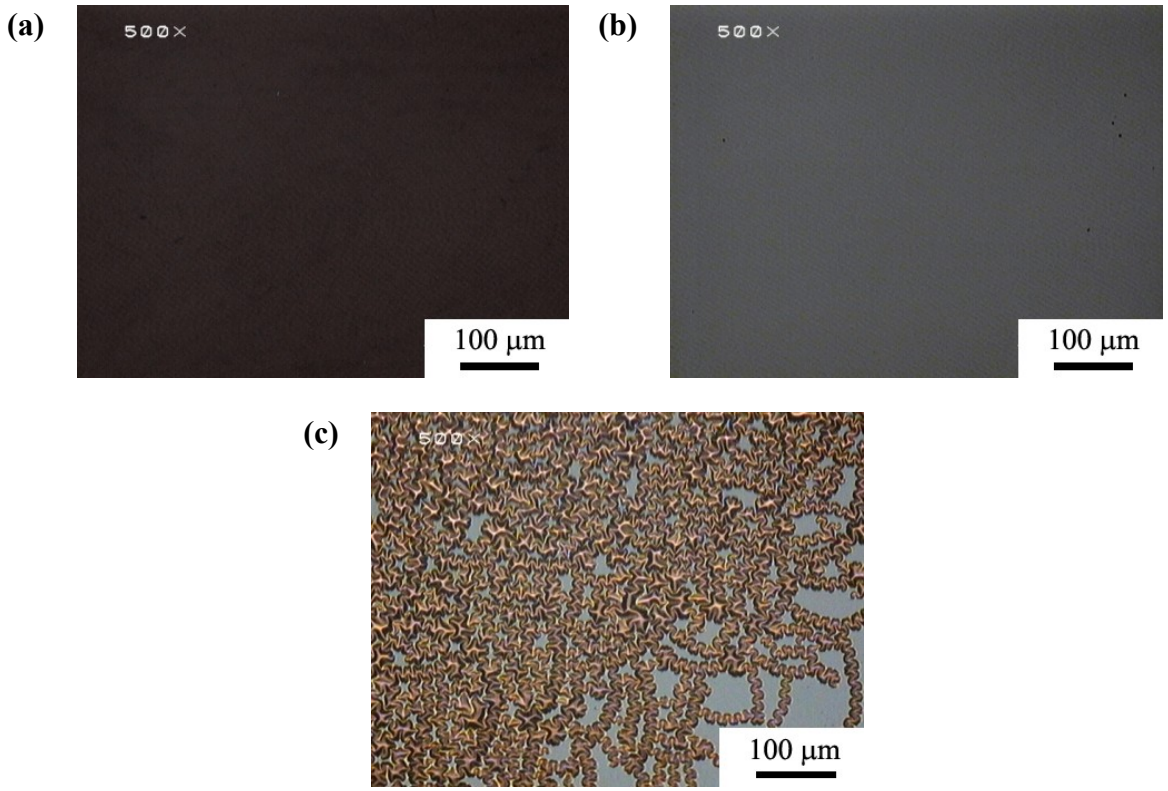

Fig. 2.2 Optical microscopic images observed on the surfaces of a-C films deposited by R.F. magnetron sputtering at Ar pressure of (a) 10.0 Pa, (b) 1.0 Pa and (c) 0.4 Pa

The structural investigation was carried out by Raman spectroscopy. Typically, the Raman shift of a-C film is in the range of 1000-1800 cm^{-1}. Figure 2.3 shows the Raman spectra of a-C films deposited by R.F. magnetron sputtering at various Ar pressures. For

a-C films deposited at Ar pressure of 10.0 Pa, a broad peak at 1550 cm^{-1} with a shoulder at 1360 cm^{-1} accompanying with a slope background is obtained as shown in Fig. 2.3(a). This slope background is correlated to the photoluminescence from the a-C film [18,19]. As the Ar pressure decreases, a shift of the Raman peak at 1550 cm^{-1} to the lower frequency as well as a flatten background is observed. The a-C film deposited at Ar pressure 1.0 Pa, the Raman peak at 1535 cm^{-1} with a shoulder at 1350 cm^{-1} is obtained, while a-C film deposited at Ar pressure 0.4 Pa has the Raman peak at 1520 cm^{-1} and 1340 cm^{-1} as shown in Fig. 2.3 (b) and (c), respectively.

For a-C films, Raman spectra with two broad bands are usually present. The G band at 1550 cm^{-1} is due to the bond stretching of all pairs of sp^2 carbon atoms in both rings and chains, while the D band at 1360 cm^{-1} is due to the breathing modes of sp^2 carbon atoms in rings. The shift of the G band as well as the relative integrated intensity of D and G bands (I_D/I_G) gives also the information of bonding within the films [20,21]. The spectra were simply decomposed into two Gaussian curves with a linear background. The peak position and width of D and G bands as well as the ratio of their integrated intensities were obtained as can be seen in Table 2.4.

Table 2.4 Positions and widths of the D and G bands from the Gaussian peaks fitting of the Raman spectra in Fig. 2.3 as well as ratio of their integrated intensities

Deposition pressure (Pa)	**D band**		**G band**		I_D/I_G
	Position (cm^{-1})	**FWHM (cm^{-1})**	**Position (cm^{-1})**	**FWHM (cm^{-1})**	
10.0	1372	277.9	1556	124.0	1.33
1.0	1367	286.9	1542	159.8	1.23
0.4	1361	288.2	1537	163.7	1.01

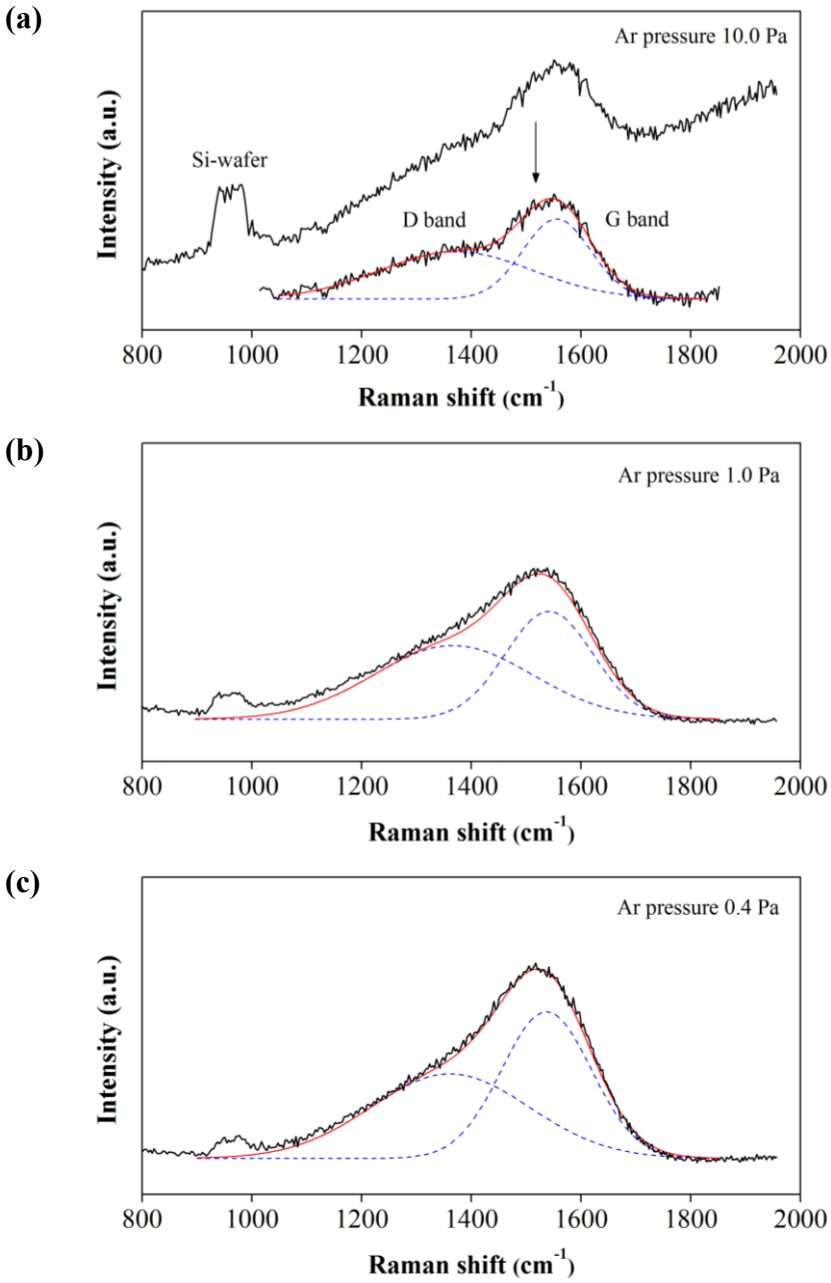

Fig. 2.3 Raman spectra of a-C films deposited on Si-wafers by R.F. magnetron sputtering at Ar pressure of (a) 10.0 Pa, (b) 1.0 Pa and (c) 0.4 Pa

From the results on the physical properties of a-C films deposited by R.F. magnetron sputtering at various Ar pressures, the effect of the Ar pressure during sputtering on the deposition rate of a-C films can be explained on the basis of the mean

free path of the sputtered C atoms travelling through the plasma [22,23]. In deposition at high pressure (10.0 Pa), the mean free path of both sputtered C atoms and Ar atoms is relatively shorter than deposition in lower pressure. This results in scattering and thermalisation of these species by collisions with the background gas and therefore leads to lower energy deposition conditions. On the other hand, as the deposition pressure decreases, the mean free path of both species becomes longer. In this case, the C atoms can reach the substrate with less energy loosing. This might account for higher deposition rate of the resultant film as shown in Table 2.3.

It is apparent that Ar pressure influenced not only the deposition rate, but also the structure of a-C films. Considering the three-stage model of graphitisation trajectory interpreted from the Raman spectra of a-C film [21], the reduction of I_D/I_G ratio as well as a downshift of the G band position is found in the stage of nanocrystalline graphite to a-C trajectory. By comparing with the present results shown in Table 2.4, the similar trend is obtained that the ratio of I_D/I_G decreases and the peak position of G band is downshift as the deposition pressure decreases. This suggests that the number and clustering of sp^2 carbon sites become smaller for films grown at lower pressures. This can be explained by the increase of the bombardment intensity on the growing film, which would prevent the formation of bigger and/or more ordered carbon clusters, such as olefinic chains or aromatic rings.

A ball-on-disk friction test was used to investigate the tribological properties of a-C films. The test condition is shown in Table 2.5. It is also noted that a-C film deposited at Ar pressure of 0.4 Pa was unable to test due to the wrinkle surface formation (Fig. 2.2(c)). The friction behaviours of the films are shown in Fig. 2.4. The a-C film deposited at Ar pressure of 10.0 Pa shows the coefficient of friction (COF) 0.2 at the starting and fluctuating in the range of 0.2-0.3. After 5 metres of sliding distance, the films show a sign

of failure, as shown in Fig. 2.4(a), by the increasing of COF and finally accompanying with a large fluctuation at the COF of 0.5-0.7. In contrast, a-C film deposited at 1.0 Pa slightly increase of COF to 0.2 after the initial COF at 0.15 is observed. However, the COF has trend to decrease again after 5 metres of sliding distance and finally reach the steady state at the value of 0.1.

Table 2.5 Ball-on-disk friction test condition for a-C film deposited by R.F. magnetron sputtering at various Ar pressures

Ball:	Stainless steel (SUS 440C) (∅ 4.8 mm)
Normal load (N):	0.3
Sliding speed (mm/s):	13
Atmosphere:	Ambient air

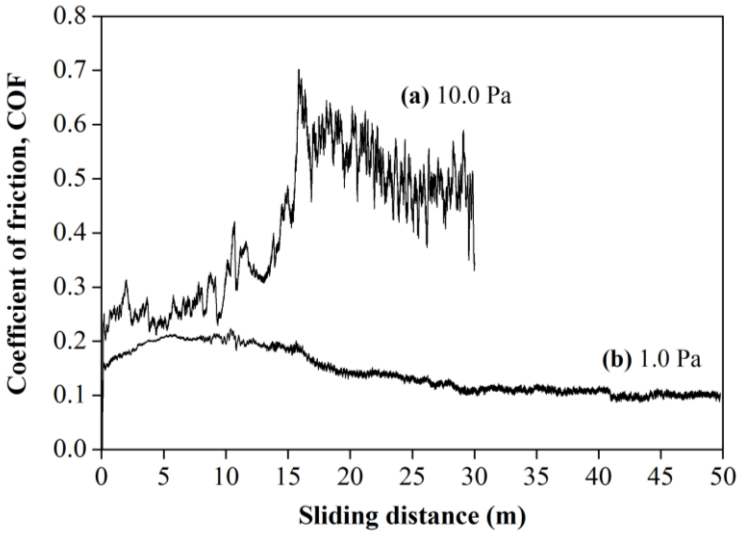

Fig. 2.4 Friction behaviours of a-C films deposited on Si-wafers by R.F. magnetron sputtering at Ar pressure of (a) 10.0 Pa and (b) 1.0 Pa

The optical microscopic image observed on the wear tracks of a-C films deposited at Ar pressure of 10.0 Pa is presented in Fig. 2.5(a). It shows clearly that a-C film is completely removed from the substrate, resulting in the exposure of Si-wafer substrate. On the other hand, the wear track of a-C film deposited at Ar pressure of 1.0 Pa is hardly observed, as shown in Fig. 2.5 (b). These results suggest that a-C film deposited at lower Ar pressure is harder and more wear resistant than the film deposited at higher Ar pressure.

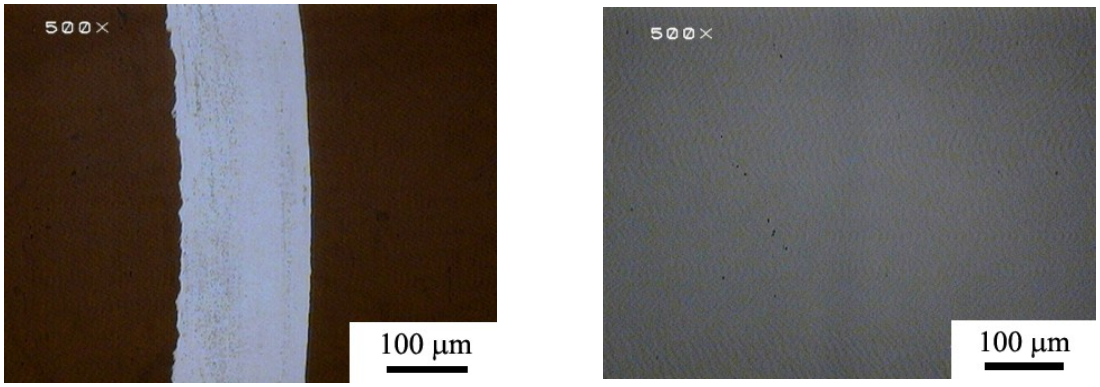

(a) 10 Pa **(b)** 1.0 Pa

Fig. 2.5 Wear tracks formed on a-C films deposited by R.F. magnetron sputtering at Ar pressure of (a) 10.0 Pa and (b) 1.0 Pa after the friction tests

The properties of a-C films are closely related to the energy of the incoming species bombarding the growing film, which is also dependent on the pressure of Ar during depostion [24,25]. Two competitive deposition mechanisms are considered to explain the growing mechanism. The first one corresponds to the diffusive deposition mechanism, in which the sputtered C atoms are thermalised and diffuse through the plasma gas and eventually reach the film. The contribution of the diffusive mechanism is predominant for higher deposition pressure, resulting in a gentle deposition. Therefore, the obtained film

has low density and mechanical properties, which is similar to the a-C film deposited at 10.0 Pa in this study. Another mechanism corresponds to the ballistic deposition, in which a C atom ejected from the target transfers a significant amount of energy and momentum to the growing film. This is predominant for films grown in low pressure, leading to strong bombardment of C atoms to form a dense and hard a-C film, which is in agreement with a-C film deposited at Ar pressure 1.0 Pa in this study. In addition to the strong bombardment, a more disordered structure is obtained as well as a compressive intrinsic stress is also developed. This is also consistent with the Raman spectra results and the wrinkle formation on the surface of a-C film deposited at the lowest Ar pressure (0.4 Pa) as obtained in this study.

In conclusion, deposition of a-C film by R.F. magnetron sputtering at the R.F. power of 100 W with the deposition pressure of 1.0 Pa is found to be the optimum condition to obtain the film with reasonable hard and low COF with a smooth surface (no wrinkle formation).

2.3.2 Luminescent ZnS:Mn layers

The manganese doped zinc sulphide (ZnS:Mn) films were fabricated into a single layer for the first candidate of luminescent wear-sensing layer. The films were deposited by R.F. magnetron sputtering method onto soda-lime glass, silicon wafer and sapphire. The deposition condition has been shown previously in table 2.1. It is well-known that post-annealing enhances the luminescent property of the as-deposited films. The physical, mechanical and optical properties of ZnS:Mn film both as-deposited and after post-annealing are shown and discussed in this section.

The optical microscopic images observed on the surface of ZnS:Mn films deposited on soda-lime glass and silicon wafer before (as-deposited) and after annealing at 700°C for 60 min are shown in Fig. 2.6. ZnS:Mn films deposited on glass substrates show a smooth surface without any defects or cracks generated in either as-deposited or after post-annealing as illustrated in Fig. 2.6(a). In contrast, cracks are observed on the surface of ZnS:Mn films deposited on Si-wafer after post-annealing as shown in Fig. 2.6(b), while they are not observed in the as-deposited films. The cracks generated on ZnS:Mn films deposited on Si-wafer after post-annealing at 700°C may be related to the large coefficient of thermal expansion (CTE) mismatch between ZnS:Mn film and Si-wafer substrates. The thermal expansion coefficients of ZnS, Si and soda-lime glass as well as sapphire are listed in Table 2.6. It can be seen that the percentage mismatch in CTE between ZnS to Si is significantly larger than to glass. To support the idea, ZnS:Mn films were also deposited on sapphire and subsequently annealed at 700°C. The obtained films exhibited the smooth surface without cracks and defects (not shown here), which also corresponded to the less mismatch of CTE between ZnS films and sapphire substrate. Therefore, soda-lime glasses are used as the substrates for deposition of ZnS:Mn films for the entire study.

Table 2.6 Thermal expansion coefficients of ZnS and a few other materials used as substrates for deposition of ZnS films [9,26]

Material	**Structure**	**CTE ($\times 10^{-6}$ K^{-1})**	**% mismatch**
Zinc sulphide (ZnS)	Cubic and Hexagonal	6.4	0
Silicon (Si)	Cubic	2.5	61
Soda-lime glass	Amorphous	7.7	20
Sapphire (Al_2O_3)	Hexagonal	5.8	9

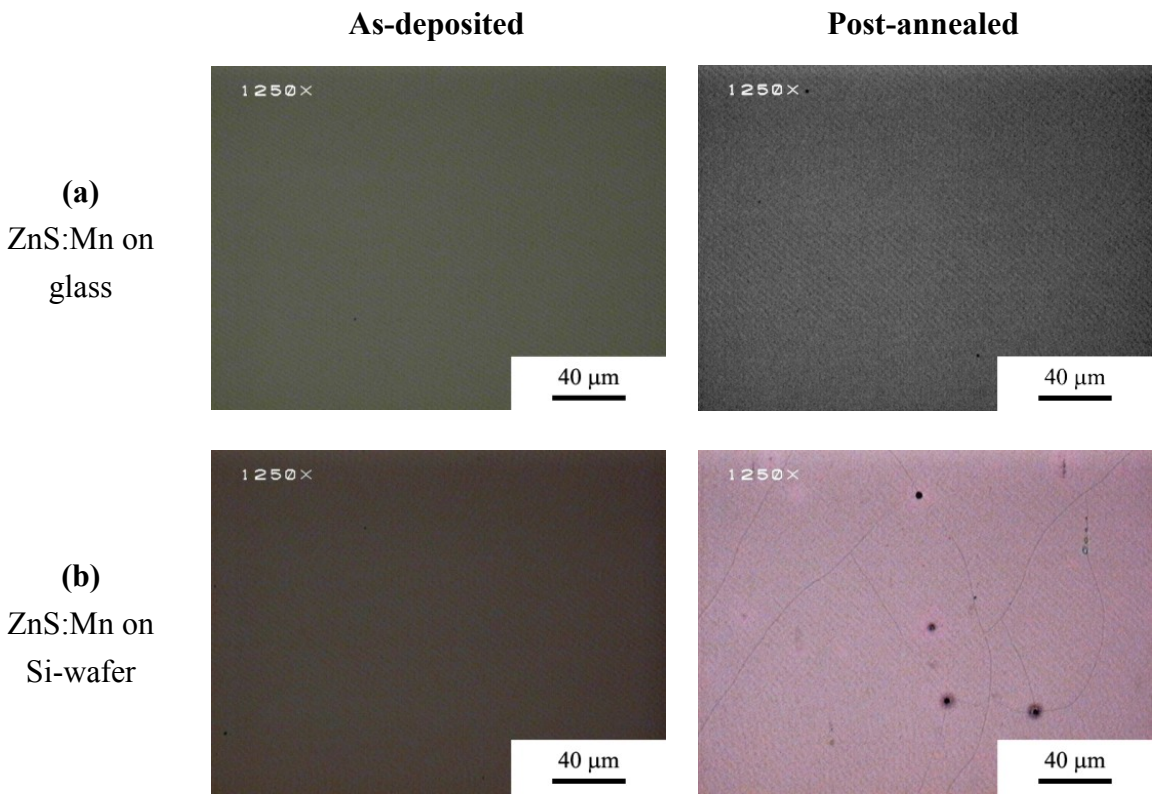

Fig. 2.6 Optical microscopic images observed on the surfaces of as-deposited and post-annealed ZnS:Mn films deposited on (a) soda-lime glass and (b) Si-wafer

The torn cross-sections of as-deposited and post-annealed ZnS:Mn films on glass substrate observed by SEM are shown in Fig. 2.7. The as-deposited ZnS:Mn film exhibits the compact columnar grains growing along the thickness of the film as shown in Fig. 2.7(a), which is typical structure of the ZnS film deposited by sputtering method [27,28]. After post-annealing at 700°C, the grain structure becomes more random orientation instead of columnar shape as presented in Fig. 2.7(b), suggesting the atomic rearrangement occurs during the annealing process. The thickness of ZnS:Mn film as measured from this cross-section is 830 nm. Furthermore, no delamination or cracks are observed along the interface between ZnS:Mn films and substrates.

The surface morphologies of the as-deposited and post-annealed ZnS:Mn films measured by AFM are also presented in Fig. 2.7. As-deposited ZnS:Mn film exhibits fine grains as shown in Fig. 2.7(c), which relates to the columnar grains as observed previously by SEM. The average surface roughness (R_a) is 1.3 nm. During post-annealing, the growing of the grain size occurs, as can be seen in Fig. 2.7(d). As a result, the average surface roughness (R_a) increases to 6.5 nm. The similar phenomenon on increasing of the surface roughness due to the grain growth influenced by post-annealing of ZnS was also observed in another literature [29] as well as other materials, which are in the same class of ZnS, such as ZnSe [30], and ZnO [31].

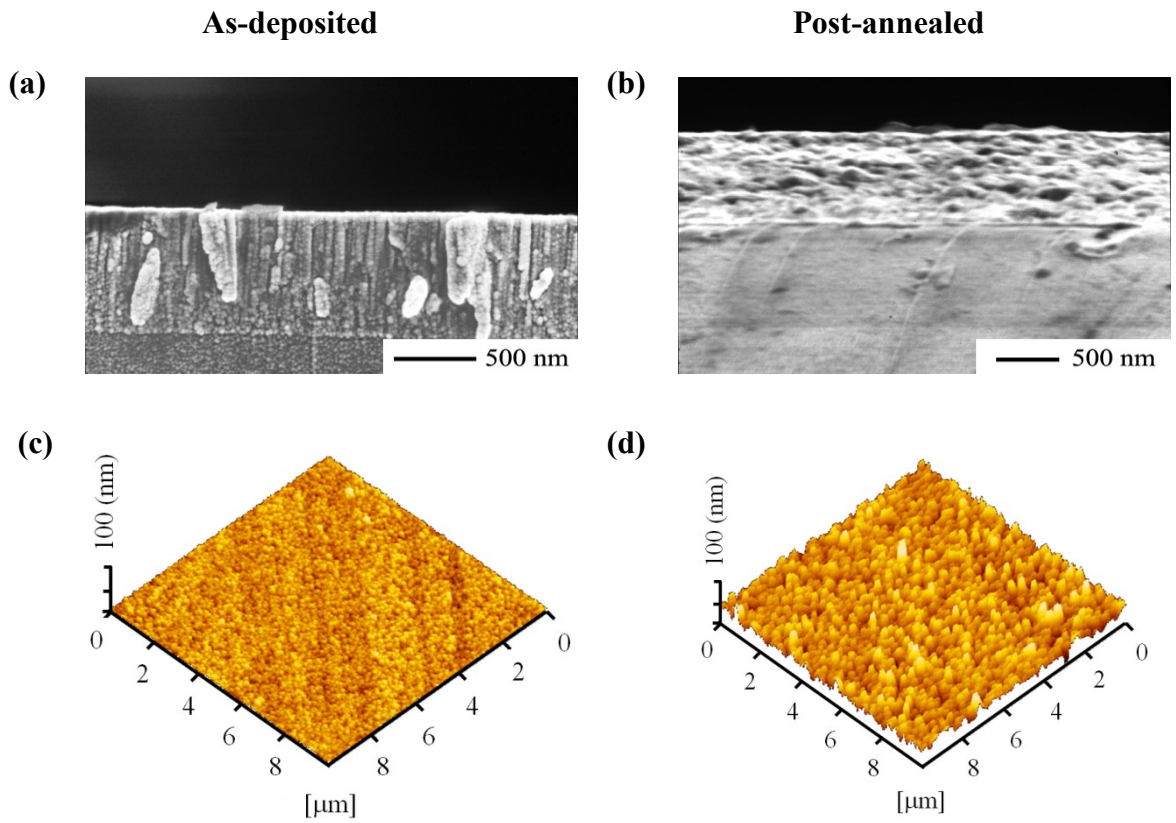

Fig. 2.7 (a, b) SEM images of the fractured cross-section and (c, d) AFM images showing the surface morphologies of as-deposited and post-annealed ZnS:Mn films

The structure of ZnS:Mn films were analysed with an x-ray diffractometer (XRD) in order to reveal the crystal structure and the phase existing in the films. Figure 2.8(a) shows the XRD pattern of ZnS:Mn plate using as the sputtering target. Several peaks from (100), (002), (101), (102), (110), (103), (200), (112), (201), (004) and (202) planes of ZnS are obtained, which correspond to the diffraction pattern of hexagonal structure of ZnS. For the as-deposited ZnS:Mn film, a strong peak at 28.54° is observed as shown in Fig. 2.8(b), which corresponds to the peak from (111) plane of cubic ZnS. Similar XRD pattern is also obtained for ZnS:Mn films after post-annealing at 700°C as shown in Fig. 2.8(c). A strong peak located at 28.58° corresponds to the diffraction form (111) plane of cubic ZnS. The noticeable broad peaks, but negligibly small intensity located at 45-60° could also be observed in the ZnS:Mn obtained from both conditions. These peaks have the peak position comparable with the ZnS:Mn target, indicating that the film could also contain some amount of hexagonal phases.

In general, ZnS films would crystallize in both cubic and/or hexagonal structure depending on the deposition condition [32]. The formation of cubic structure is more preferable at lower temperature even though the ZnS target has hexagonal structure, but the structure can transfer to hexagonal structure after heating to 800°C in ambient pressure [33,34]. In the present study, ZnS:Mn films are also deposited at room temperature, in which the structure is more preferable in cubic phase and the annealing temperature is not as high as to change the structure from cubic ZnS to hexagonal one. Furthermore, it is found that the diffraction peak from (111) plane of ZnS after post-annealing is more intense with narrower width, suggesting the improvement of crystallinity and increasing of the grain size [35,36], which is consistent with the results obtained by SEM and AFM as already presented in Fig. 2.7.

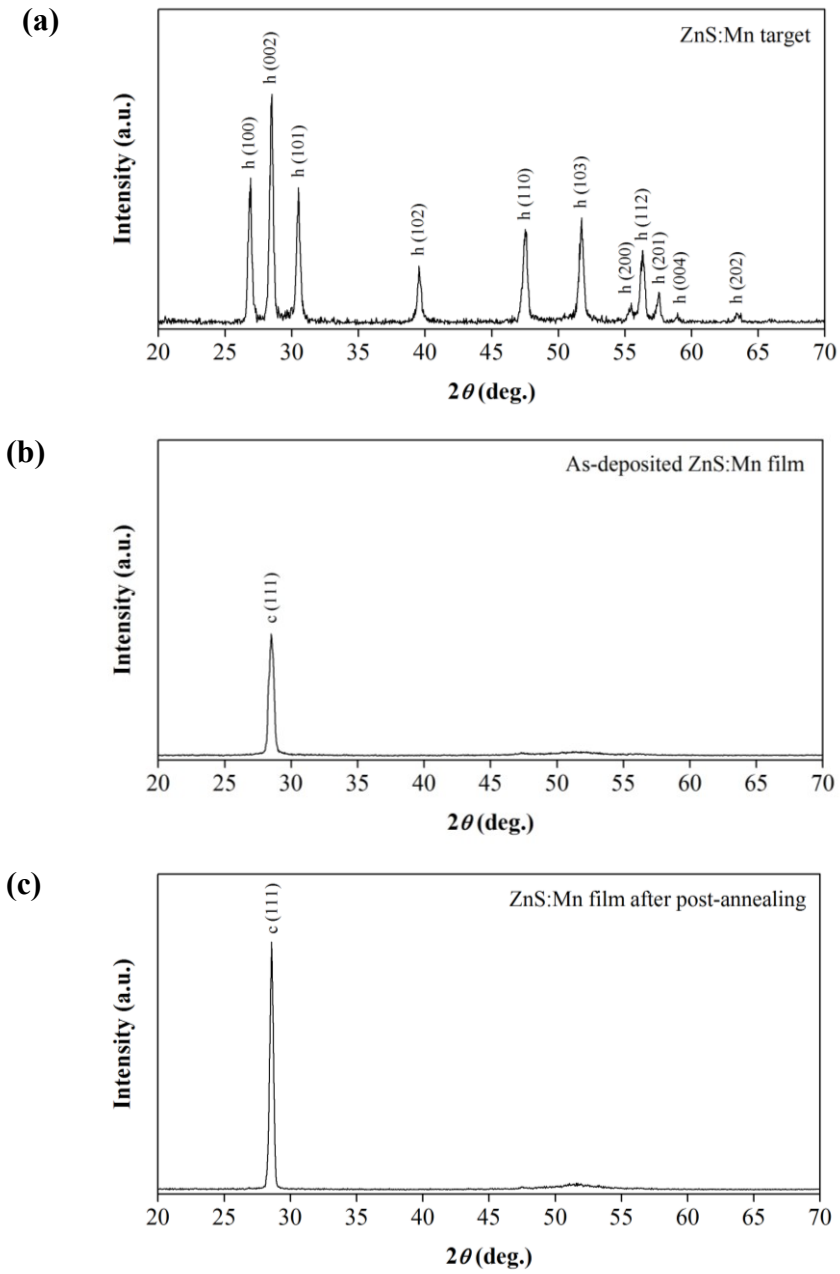

Fig. 2.8 XRD patterns of (a) ZnS:Mn target, (b) as-deposited ZnS:Mn film and (c) ZnS:Mn film after post-annealing at 700°C

The structural parameters, such as interplanar spacing (d), lattice constant (a), grain size (L), internal stress (σ_s) and dislocation density (δ), could be determined from the XRD pattern by using the equations as followed [37,38];

The average grain size (L) for ZnS films is calculated from the width of (111) peak at half maximum intensity (β) using Debye–Scherrer formula given by

$$L = \frac{0.9\lambda}{\beta\cos\theta} \tag{2.1}$$

where θ is the diffraction angle and λ is the X-ray wavelength (1.542 Å).

The inter planar spacing (d) is evaluated using the standard Bragg's relation,

$$d = \frac{n\lambda}{2\sin\theta} \tag{2.2}$$

The lattice constant (a) for the cubic phase of ZnS is determined by the expression given by

$$a = d(h^2 + k^2 + l^2)^{1/2} \tag{2.3}$$

where h, k and l denotes the lattice planes.

The intrinsic stress (σ_s) developed in the film due to the deviation of measured lattice constant of ZnS over the bulk is calculated using the relation,

$$\sigma_s = \frac{Y}{2\gamma}\frac{(a-a_0)}{a_0} \tag{2.4}$$

Here, Y is the Young's modulus of ZnS (75 GPa), a the lattice constant measured from the XRD data, a_0 the bulk lattice constant (5.406 Å) and γ is the Poisson's ratio (0.28) for ZnS.

The dislocation density (δ) in the grown films was determined using the expression

$$\delta = \frac{15\beta\cos\theta}{4aL} \tag{2.5}$$

These structural parameters are summarized in Table 2.7. It can be seen that the grain size of ZnS:Mn film after post-annealing is larger than that of as-deposited, which is in agreement with the result obtained by the AFM in Fig 2.7 (c) and (d). In addition, the lattice parameters of both as-deposited and post-annealed ZnS:Mn films are found to be higher than the bulk constant of ZnS, which reveal that the crystallites were under tensile stress. However, the intrinsic tensile stress of the film was reduced after post-annealing.

Table 2.7 Structural parameters of as-deposited and post annealed ZnS:Mn films determined from the XRD patterns in Fig. 2.8 using Eq. (2.1)-(2.5)

ZnS:Mn	**As-deposited**	**Post-annealed**
2θ (deg.)	28.50	28.58
FWHM, β (deg.)	0.471	0.310
(h k l)	(111)	(111)
Lattice spacing, d (Å)	3.132	3.124
Lattice parameter, a (Å)	5.425	5.411
Grain size, L (nm)	17.4	26.5
Internal stress, σ_s (GPa)	0.474	0.124
Dislocation density, δ ($\times 10^{15}$ lin/m^2)	3.16	1.37

The hardness and elastic modulus of the ZnS:Mn films were evaluated by means of a typical load-displacement curve via nanoindentation analysis. In order to obtain the true hardness of the film without the influence of substrate, it is generally assumed that the indentation depth should not exceed 10% of the film thickness. For the ZnS:Mn film with the thickness of 830 nm in the present study, it was found that the optimum indentation load that the indenter penetrates within that allowable range of thickness was 1.5 mN. The load-displacement curves for both as-deposited and annealed ZnS:Mn films are presented in Fig. 2.9. It can be seen that the penetration depth of post-annealed ZnS:Mn film was higher than the depth of as-deposited film with the same amount of load. This suggests that the annealed film is softer than the as-deposited film. The indentation was carried out for three times, in which the hardness (H) and elastic modulus (E) as well as the indentation depth of the ZnS:Mn films both as-deposited and post-annealed are given in Table 2.8. The hardness of as-deposited ZnS:Mn film is in the range of 6.2-6.6 GPa, while the hardness of post-annealed film is 5.3-5.7 GPa.

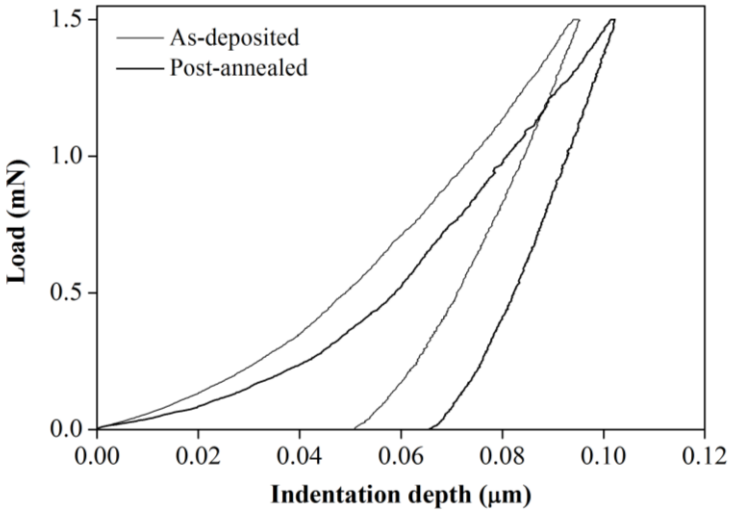

Fig. 2.9 Nanoindentation load-displacement curves for the as-deposited and post-annealed ZnS:Mn films

Table 2.8 Hardness, elastic modulus and indentation depth of as-deposited and post-annealed ZnS:Mn films indented at 1.5 mN load

ZnS:Mn film	Hardness H (GPa)	Elastic Modulus E (GPa)	Indentation depth (nm)
As-deposited	6.2-6.6	97.8-101.3	50.0-51.5
Post-annealed	5.3-5.7	92.6-104.7	57.0-71.0

Generally, the hardness of the thin solid film has a close correlation with the intrinsic or residual stress of that film. Huang et al. have found that the mechanical properties of SiN films obviously varied with residual stresses, especially with the tensile stresses [39]. With decreasing compressive stress towards increasing tensile stress, the hardness and modulus decreased respectively from maximum values for the film containing the largest residual compressive stress to minimum value for the film with the largest tensile stress. Chang et al. also found the same similar relationship for the metallic

titanium film [40]. These could be implied that the film with higher intrinsic tensile stress should have lower mechanical properties than the film with lower one, which seems to be contrary to the result found in the present study. The as-deposited ZnS:Mn film contains higher intrinsic tensile stress accompanying the higher hardness than the post-annealed film. However, the elastic modulus measured from ZnS:Mn films from both conditions are in the same range. In this case, another factor that causes the reduction of hardness should be account.

Nose et al. have studied the influence of Si contents on the structure and mechanical properties of Ti-Si-N thin films [41]. It was found that the Ti-Si-N film showed the higher hardness than the typical value at the amount of Si 5% at. due to the formation of columnar crystal grains and lattice distortion. Increasing the content of Si, the hardness was reduced to the typical value, which attributed to the formation of nanocomposite TiN/Si_3N_4 film structure. In addition, Kim et al. studied on the effects of substrate temperature on the mechanical properties of TiN film [42]. Their results revealed that the TiN films deposited at substrate temperature 450°C had the maximum hardness with a dense columnar structure. When the substrate temperature increased to 600°C, the films showed a granular structure with reduced hardness. These findings compare well with the result obtained in the present study, in which the reduction of the hardness for the post-annealed film is attributed to the change of microscopic structure from dense columnar to the granular structure.

Photoluminescence (PL) spectra of ZnS:Mn films were measured from the surface of ZnS:Mn films under irradiating with the UV light at the excitation of 365 nm. Figure 2.10(a) displays the PL emission from both as-deposited and post-annealed ZnS:Mn film. It is apparent that the as-deposited film does not exhibit PL under irradiating with a UV light, while the film after post-annealing at 700°C exhibits the intense yellowish-orange PL

emission. The PL spectra of the as-deposited and post-annealed ZnS:Mn after subtracting the substrate background is also illustrated in Fig. 2.10(a). The PL spectrum of the as-deposited film shows only a flat spectrum without any distinct peak, while the post-annealed film exhibits strong peak at the centre of 587 nm. The emission peak at 587 nm is a characteristic emission of Mn^{2+} ions in ZnS crystals [43,44].

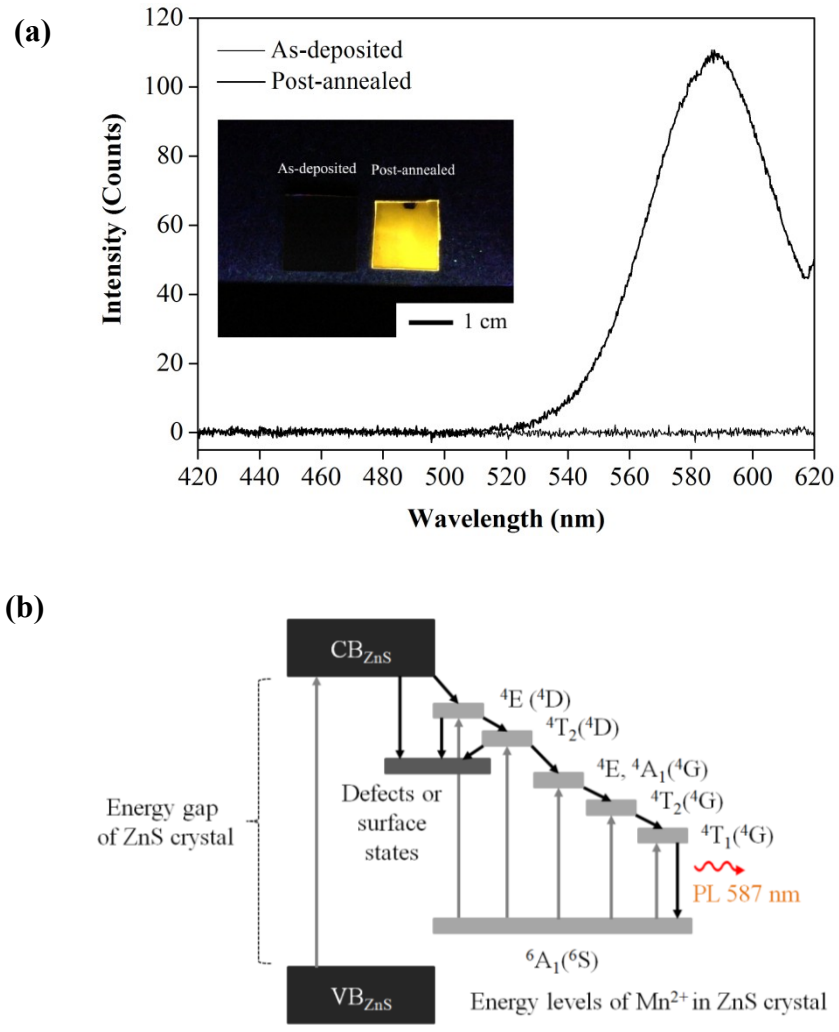

Fig. 2.10 (a) Photoluminescence (PL) investigation and PL spectra of as-deposited and post-annealed ZnS:Mn films under irradiating with a UV light at 365 nm and (b) a schematic luminescence process in ZnS:Mn crystal [45]

The luminescence process of ZnS:Mn materials can be represented via band diagram as shown in Fig. 2.10(b). It is suggested that the excitation mechanism of Mn^{2+} ions in ZnS crystals can be achieved by two ways [45,46]. One is indirect excitation, i.e., interband excitation of the ZnS host crystal (valence band to conduction band), followed by energy transfer from the host to the Mn^{2+} ions inducing the luminescence. The other one is direct excitation of the Mn^{2+} ions, in which the excitation energy is lower than the energy gap of ZnS crystal. In both cases, the excitation energy will transfer from the excited states through the $^4E(^4D)$, $^4T_2(^4D)$, ^4E, $^4A_1(^4G)$, and $^4T_2(^4G)$ to the emitting state, i.e., $^4T_1(^4G)$ states and subsequently transfer radiatively to the ground state at $^6A_1(^6S)$. Therefore, the yellowish-orange emission at 587 nm from ZnS:Mn crystals can be excited by several excitation wavelengths, i.e., less than 335 nm (indirect excitation) [47], 392, 430, 463, 468, 492, and 530 nm (direct excitation) [45,46].

Figure 2.11 shows the UV/VIS absorption spectra of both as-deposited and post-annealed ZnS:Mn films. The inset of Fig. 2.11 shows the corresponding relationships of $(\alpha.hv)^2$ versus hv of both films in order to determine the band gap energies of both films [48]. It is apparent that the absorption spectrum of the as-deposited ZnS:Mn film has a slope band edge with the tail extends to around 380 nm. The corresponding energy gap of the film is 3.41 eV. For the post-annealed ZnS:Mn film, the absorption spectrum has a sharper band edge at the cut-off wavelength at 340 nm. The corresponding energy gap of the film is 3.66 eV, which is shifted to the higher energy (blue shift) as compared with the as-deposited films.

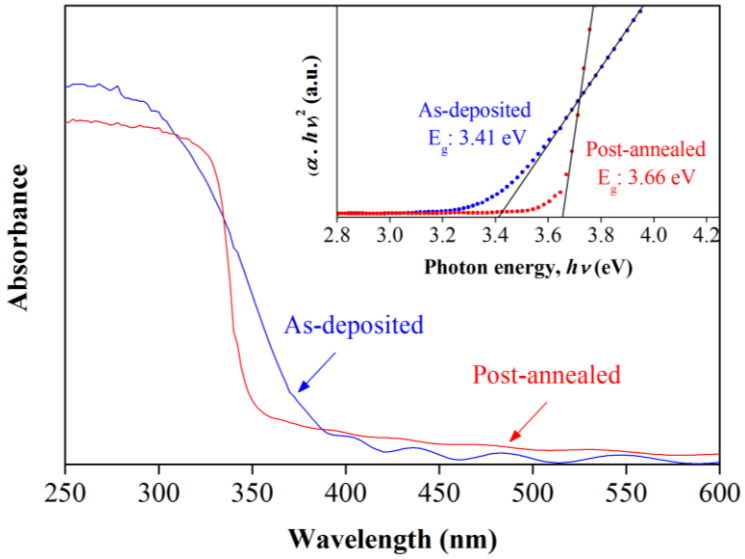

Fig. 2.11 UV-VIS absorption spectra of as-deposited and post-annealed ZnS:Mn films and the relationship between $(\alpha.h\nu)^2$ and $h\nu$ of both films for determining the energy gap (inset)

Su, et al. also found the shift of the energy gap with the sharper absorption edge in the SiO_2 encapsulated ZnS nanoparticles (ZnS/SiO_2) [49]. The blue shift of the energy gap with the sharper absorption edge was found for the ZnS/SiO_2 structure compared to the bare ZnS nanoparticles. It was explained that due to the size of ZnS nanoparticles decreased, the surface-to-volume ratio increased, which resulted in an increase in the number of the broken and dangling bonds. Therefore, the microstructure of the bare ZnS nanocrystals was more disordered and highly defected to give sub-bands of defects in the gap of the crystals. These defect sub-bands in the gap of nanocrystals would result in an optical absorption with smaller energies than the gap. On the other hand, ZnS nanocrystals in ZnS/SiO_2 nanostructures were fully encapsulated by the SiO_2 layer, which would decrease the number of broken and dangling bonds and reduced the influence of defect states on the optical absorption. As a result, the energy gap was blue shifted to be closed to the energy gap of the bulk ZnS crystal with the significantly enhanced luminescence

performance. This is found to be in agreement with the result found in this study, the blue shift of the energy gap closely to the bulk energy gap of ZnS (3.7 eV) with the shaper absorption edge for the post-annealed ZnS:Mn film compared to the as-deposited films. This indicates that the numbers of the defect states are decreased in the post-annealed ZnS:Mn film. Moreover, this is also consistent with the XRD results as described previously, in which the crystalinity was improved and the numbers of defects were reduced by the post-annealing process. As a result, the luminescence property was significantly improved.

Figure 2.12 shows the Raman spectra of as-deposited and post-annealed ZnS:Mn films as excited by the green laser with the wavelength 532 nm or photon energy of 2.33 eV. The as-deposited ZnS:Mn film shows only an observable peak at the Raman shift of 351 cm^{-1} with a flat spectrum. This peak is corresponded to the longitudinal optical (LO) mode of Raman vibration of cubic ZnS crystal [50]. In contrast, the Raman spectrum with a strong luminescent background was detected for the post-annealed ZnS:Mn film. These results indicate that the existence of Mn ions in the post-annealed ZnS film is more optically active or has contribution for the luminescence emission than those in the as-deposited. This is because the Raman spectroscopic investigation simulates the luminescence process by direct excitation of Mn ions in ZnS crystals since the excitation energy is lower than the energy gap of ZnS [45,46].

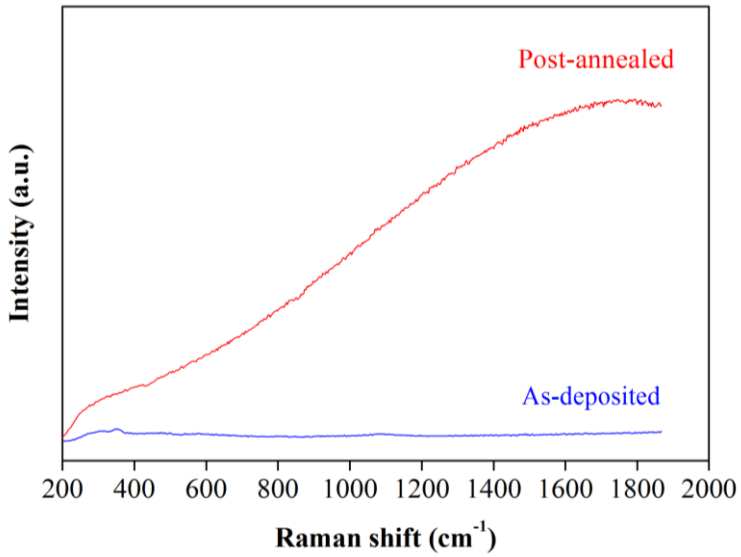

Fig. 2.12 Raman spectra of as-deposited and post-annealed ZnS:Mn films excited by a green laser with the wavelength 532 nm

The homogeneous distribution of Mn^{2+} ions in a ZnS crystal lattice is also considerably important for highly efficient luminescence. For the inhomogeneous distribution of Mn^{2+} ions, local Mn^{2+}-Mn^{2+} pairs or clusters can be formed in the ZnS crystals, which interact and lead to non-radiative relaxation under excitation [51]. On the other hand, although the Mn^{2+} ions incorporate homogeneously in ZnS crystals, if the crystals still contain some defects and they are located close to each another in the ZnS crystals, non-radiative relaxation can also be occurred through the defects states as can also be seen in Fig. 2.10(b). These result in low luminescence efficiency [52].

During the sputtering process, ZnS forms the main phase while Mn^{2+} is present as an impurity and can gradually be incorporated into the ZnS crystal lattice, depending on process conditions. Since the deposition of ZnS:Mn film was carried out at the room temperature, the atomic mobility is not high enough to diffuse freely on the substrate surface to form a high quality crystalline structure as well as to eliminate the defects. Mn^{2+}

might also have not been effectively incorporated into the ZnS crystal lattices, probably existing near the ZnS crystal surfaces. However, a significant enhancement of the crystallinity is obtained by the post-annealing. The growing of the crystal as evidenced by the AFM image (Fig. 2.7) as well as the reduction of defect density as calculated from the XRD (Table 2.7) indicates that a significant enhancement in the movement of Mn^{2+} and Zn^{2+} ions and rearrangements of crystal structure. Mn^{2+} can effectively diffuse into the ZnS lattice, forming a homogeneous solid solution throughout the crystals. This is beneficial to the spatial isolation or homogenisation of Mn^{2+} ions as well as the elimination of crystal defects. As a result, both crystallinity and photoluminescence property are significantly improved.

2.3.3 Deposition of a-C films on ZnS:Mn layers by R.F. magnetron sputtering method

In previous section, the luminescent ZnS:Mn films (as-fabricated ZnS:Mn film hereafter in this section) were prepared by R.F. magnetron sputtering and post-annealing at 700°C. Furthermore, the optimum condition for deposition of a-C film by R.F. magnetron sputtering was also obtained in the section 2.3.1. Therefore, a-C films were subsequently deposited on the luminescent ZnS:Mn by using the optimum condition as summarised in Table 2.9. The additional Si-intermediate layer was also deposited onto the ZnS:Mn layer prior to the deposition of a-C film for comparison the adhesion properties. The physical, mechanical and tribological properties of the a-C coatings without and with Si-intermediate layer on ZnS:Mn layers are characterised and discussed in this section. From the deposition condition as shown in Table 2.9, a-C film deposited on ZnS:Mn film directly without Si-intermediate layer (a-C/ZnS:Mn coating) had the thickness of 85 nm,

while a-C film deposited with Si-intermediate layer (a-C/Si/ZnS:Mn coating) had total thickness of 109 nm.

Table 2.9 Process parameters and conditions for deposition of a-C film on ZnS:Mn layer by R.F. magnetron sputtering method

Process	Parameter	Corresponding value
Chamber condition	Target	Graphite
	Plasma gas	Argon (99.995% purity)
	Base pressure (Pa)	Less than 1.5×10^{-3}
Plasma surface treatment of substrate	R.F. power (W)	100
	Pressure (Pa)	10
	Time (min)	10
Deposition of Si-intermediate layer	R.F. power (W)	50
	Pressure (Pa)	1
	Electrodes distance (mm)	50
	Time (min)	3
	Thickness (nm)	24
Deposition of a-C films	R.F. power (W)	100
	Pressure (Pa)	1
	Time (min)	60
	Electrodes distance (mm)	50
	Substrate temperature (°C)	Room temperature
	Thickness (nm)	85

The structure of a-C film deposited on the ZnS:Mn layer was confirmed by Raman spectroscopy as shown in Fig. 2.13. It has been found that the Raman spectrum detected from a-C film deposited on as-fabricated (post-annealed) ZnS:Mn layer accompanies with a strong luminescence background as shown in the inset of Fig. 2.13. Compared with the

Raman spectrum from the post-annealed ZnS:Mn as already shown in Fig. 2.12, a clear but indistinct spectrum with the peak at the Raman shift around 1520 cm^{-1} could be observed. This spectrum corresponds to the Raman spectrum of a-C film. However, it is difficult to distinguish the Raman spectrum of a-C film from the spectrum of ZnS:Mn layer. Therefore, the Raman spectrum was measured from the a-C film deposited on the as-deposited ZnS:Mn layer, in which the Raman spectrum was obtained clearly without the luminescent background of ZnS:Mn layer because the layer was not luminous. The spectrum is also shown in Fig. 2.13, in which the Raman spectrum of a-C film shows the typical Raman spectrum of a-C film and is similar to the Raman spectrum of a-C film deposited on Si-wafer as already presented in Fig. 2.3(b). The spectrum is composed of two bands as can be decomposed by simple Gaussian spectra, revealing the corresponding D band at 1362 cm^{-1} and G band at 1534 cm^{-1}.

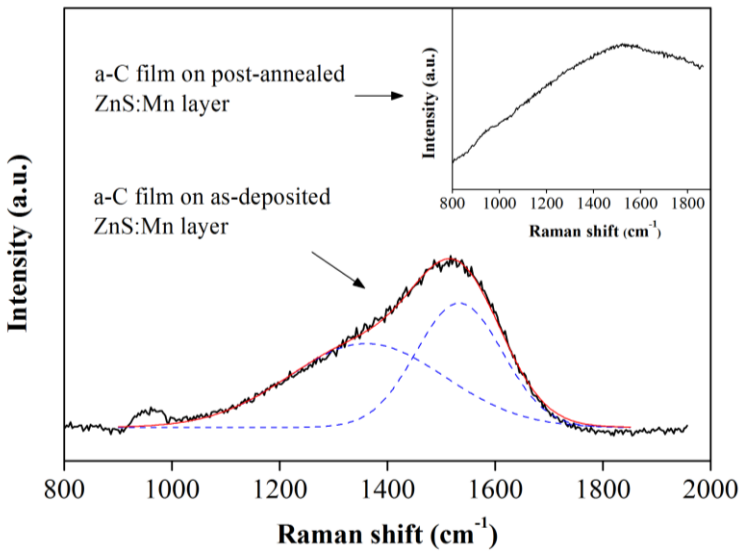

Fig. 2.13 Raman spectrum of a-C film deposited on as-deposited ZnS:Mn layer, while the inset showing the Raman spectrum of a-C film deposited on post-annealed ZnS:Mn layer

The optical microscopic images of the a-C/ZnS:Mn and a-C/Si/ZnS:Mn coatings are shown in Fig. 2.14(a) and (b), respectively. The a-C films obtained from both conditions show the clear surface morphology in macroscopic level without cracks or wrinkle formation. In microscopic scale as analysed by AFM, the surface morphology of a-C/ZnS:Mn coating is shown in Fig. 2.14(c). The surface topology appears to be conformable to the surface topology of the as-fabricated ZnS:Mn underlayer as shown in Fig. 2.7(d). The average surface roughness (R_a) is 6.1 nm, which is slightly lower than the R_a of ZnS:Mn layer as prior to a-C film deposition (R_a: 6.5 nm). In case of a-C/Si/ZnS:Mn coating, the surface roughness evolution has different topology from the ZnS:Mn layer since the total thickness is thicker due to the addition of Si-intermediate layer as shown in Fig. 2.14(d). The average surface roughness (R_a) is 6.8 nm, which is slighly higher than a-C film deposited without Si-intermediate layer. The change in surface morphology as well as the evolution of surface roughness is influenced by the initial surface morphology of the substrate and the thickness of a-C coating [53]. Since the mean roughness depth (R_z) of ZnS:Mn film was found to be 64 nm, which is slightly lower than the thickness of a-C film (85 nm). Therefore, the slightly lower R_a for a-C/ZnS:Mn coating corresponds to the initial smoothening process. However, as the thickness of a-C coating increases due to the addition of Si-intermediate layer (109 nm), the slight increase in the R_a corresponds to the roughening stage. The valley has been filled by growing film and form the island on the valley as the island grows bigger and the peak-to-valley distance gets larger. However, the R_a of a-C coating (R_a: 6.8 nm) increases slightly from the R_a of ZnS:Mn layer (R_a: 6.5 nm), indicating the islands coalesening or merging is also occurred. As a result, the surface morphology of a-C/Si/ZnS:Mn coating has been different from the a-C/ZnS:Mn coating.

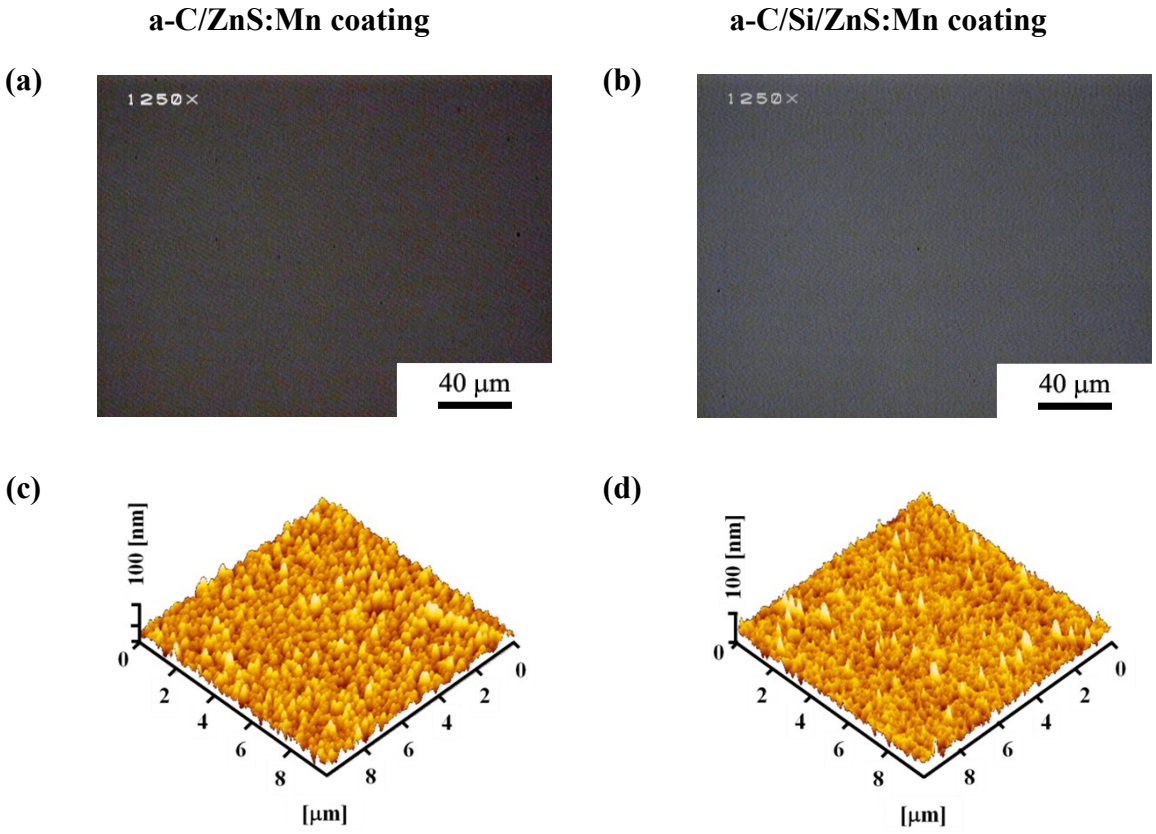

Fig. 2.14 (a) and (b) showing the optical microscopic images, while (c) and (d) showing the AFM images of a-C/ZnS:Mn and a-C/Si/ZnS:Mn coatings, respectively

Photoluminescence (PL) investigations of ZnS:Mn layers after being deposited with a-C films were carried out by irradiating with a UV light at 365 nm. Figure 2.15(a) shows the PL spectrum measured from a-C/ZnS:Mn coating. The spectrum is plotted comparatively with the PL spectrum of ZnS:Mn layer before being deposited with a-C film. The as-fabricated ZnS:Mn layer shows a strong yellowish-orange emission as obtained in this study. After a-C film was deposited onto the ZnS:Mn layer, the luminescence was nearly disappeared. This can also be confirmed by the PL spectrum of a-C coated ZnS:Mn layer, in which the PL intensity is drastically dropped. In case of a-C/Si/ZnS:Mn coating, the luminescence from the coating was completely disappeared. The PL spectrum shows

only a flat luminescence spectrum without any distinct peak as illustrated in Fig 2.15(b). The amount of luminescent intensity was analysed by the Gaussian fitting of the PL spectra. The peak positions as well as intensities of each coating system are summarised in the inset table. It can be seen that for the a-C/ZnS:Mn coating, the relative PL intensity of 1.7% could be detected, while the zero PL intensity was detected for the a-C/Si/ZnS:Mn coating. This indicates that a-C film can prevent the luminescence process of ZnS:Mn layer to occur.

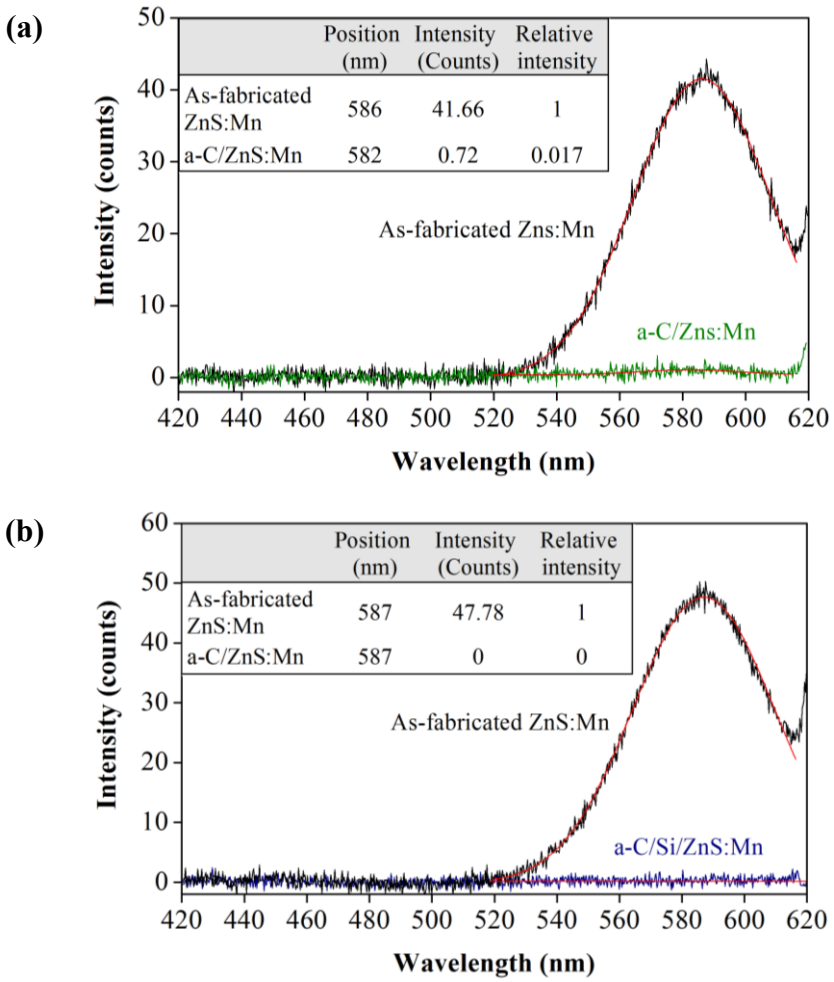

Fig. 2.15 Photoluminescence spectra of (a) a-C/ZnS:Mn and (b) a-C/Si/ZnS:Mn coatings compared with the as-fabricated ZnS:Mn layers

Considering the absorbance of a-C films deposited on glass substrates without and with Si-intermediate layers as shown in Fig. 2.16, the absorption of the coating at the excitation wavelength (UV light at 365 nm) is higher than at the emission spectrum (587 nm). Furthermore, the absorption at the excitation wavelength becomes stronger when the Si-intermediate layer is added. Therefore, it can be stated that the reduction of luminescent intensity from the ZnS:Mn layer is caused by the a-C film in which a portion of excitation ray was absorbed by a-C film. In case of a-C films with Si-intermediate layer, the excitation ray was completely absorbed, resulting in no excitation and emission occurred for ZnS:Mn layer.

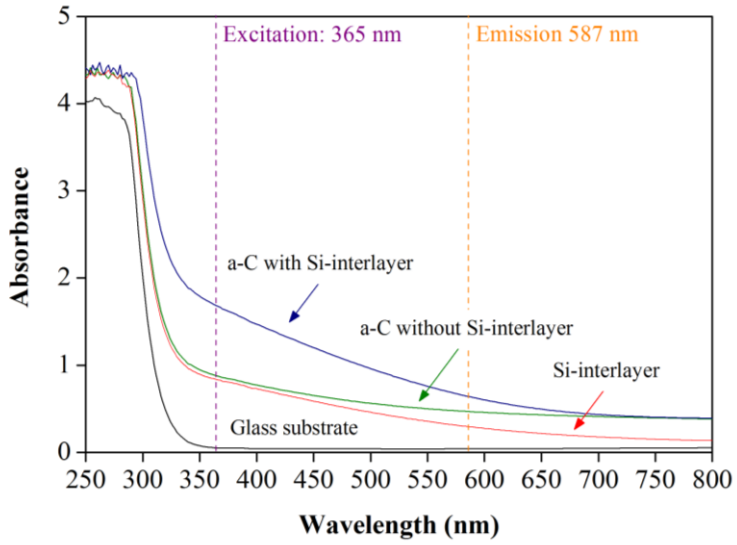

Fig. 2.16 UV-VIS absorbance spectra of a-C film deposited on soda-lime glasses without and with Si-intermediate layers

The tribological properties of the coatings were analysed by a ball-on-disk friction test with the testing conditions summarised in Table 2.10. The friction characteristics of both a-C/ZnS:Mn and a-C/Si/ZnS:Mn coatings are illustrated in Fig. 2.17. The

a-C/ZnS:Mn coating shows the coefficient of friction (COF) at around 0.25 at the beginning of the test and keeps the COF value between 0.25-0.3 for a few metres of sliding distance. Then the COF gradually increases to the higher value with a large fluctuation, indicating a sign of coating failure. The similar friction behaviour is also obtained for a-C/Si/ZnS:Mn coating, in which the coating shows the COF in the range of 0.25-0.30 for a few metres of sliding distance and followed by an unstable COF, which might indicate the coating failure has occurred.

Table 2.10 Ball-on-disk friction test conditions for a-C/ZnS:Mn and a-C/Si/ZnS:Mn coatings fabricated by R.F. magnetron sputtering

Ball:	Stainless steel (SUS 440C) (∅ 4.8 mm)
Normal load (N):	0.3
Sliding speed (mm/s):	13
Atmosphere:	Ambient air

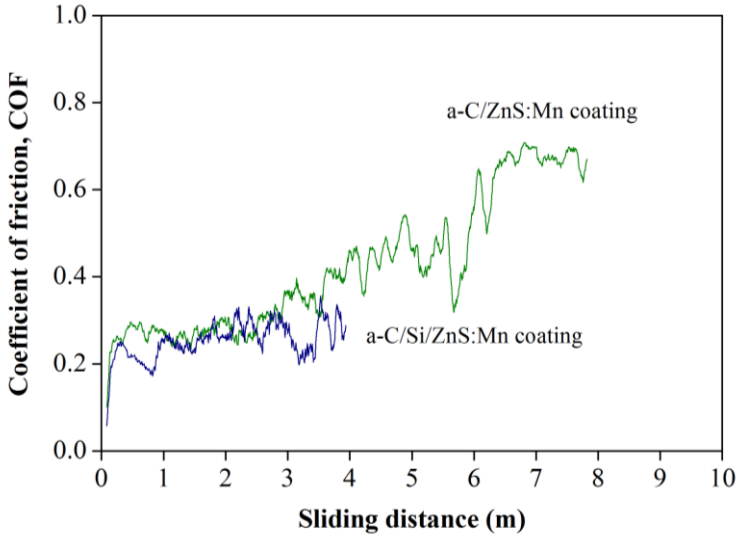

Fig. 2.17 Friction behaviours of a-C/ZnS:Mn and a-C/Si/ZnS:Mn coatings

The optical microscopic images observed on the wear tracks formed both coatings and the surfaces of the counterface balls after the friction test are shown in Fig. 2.18. For the a-C/ZnS:Mn coating, a-C film is completely worn revealing the ZnS:Mn underlayer as can be seen in Fig. 2.18(a). It is also observed that the wrinkles are formed at the edge of the wear track. The contact surface of stainless steel ball is shown nearby, in which the transferred material and debris are accumulated at one side of the sliding direction. There is also no transferred film formed on the contact area of the ball surface. In addition, the width of the real contact area of the ball is smaller than the width of the wear track formed on the a-C coating. In case of a-C/Si/ZnS:Mn coating, the wear track shows the slightly improved wear characteristic of a-C film as shown in Fig. 2.18(b). This might be because the shorter sliding distance compared with the previous condition. No wrinkles are formed at the edge of the wear track. At the contact ball surface, there is a transferred film partially formed on the surface as well as accumulated at one side of sliding direction. Moreover, the width of the contact area on the ball surface is equal to the width of the wear track formed on the coating.

Considering the mechanical response of the coatings when they are subjected to the applying load by using nanoindentation analysis, the coatings are indented at the same amount of load. Figure 2.19 shows the typical load-displacement curves of the various coatings indented at a normal load of 0.5 mN. Compared with a-C film deposited on Si-wafer substrate, the a-C/ZnS:Mn coating shows higher maximum indentation depth, indicating that the coating becomes softer due to the effect of ZnS:Mn underlayer as shown in Fig. 2.19(a). In addition, the small but clear discontinuous pop-in step during loading is observed at the critical load of 0.3 mN and indentation depth of 35 nm, which can be attributed to the formation of the cracks on a-C film due to the large deformation of the softer substrate [54,55]. In case of a-C/Si/ZnS:Mn coating, the mechanical response is

remarkably improved as can be seen in Fig. 2.19(b). Although the maximum depth is slightly higher, which means softer, as compared with the a-C film deposited on Si-wafer, the load-unloading curve is similar to the a-C film deposited on Si-wafer. This indicates the less effect of ZnS:Mn layer substrate on the mechanical response of the a-C film. Furthermore, the total thickness of coating is thicker than the previous condition. This might also affect the improved properties. However, the removal of a-C film reaching to the ZnS:Mn underlayer is still observed as shown in Fig. 2.18(b), indicating that the adhesion between the tribological layer and the luminescent layer is not strong enough.

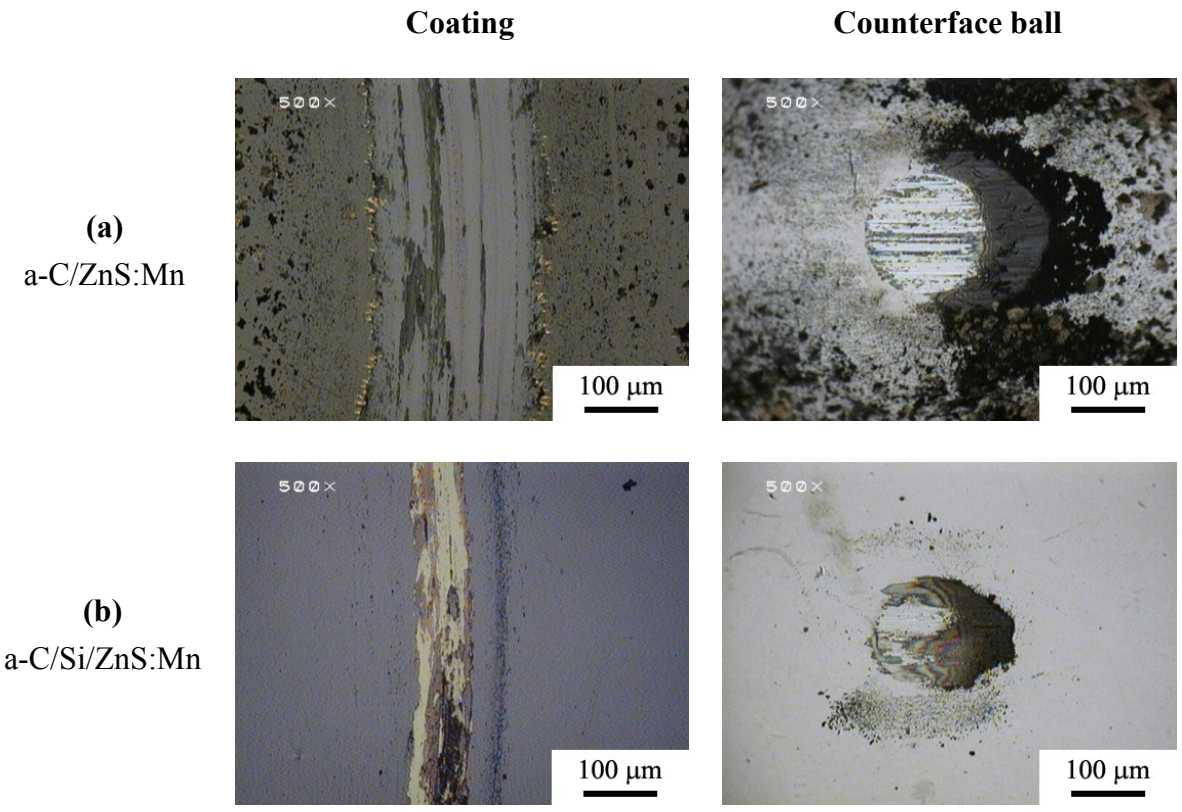

Fig. 2.18 Optical microscopic images observed on the wear tracks formed on (a) a-C/ZnS:Mn and (b) a-C/Si/ZnS:Mn coatings and the contact ball surfaces

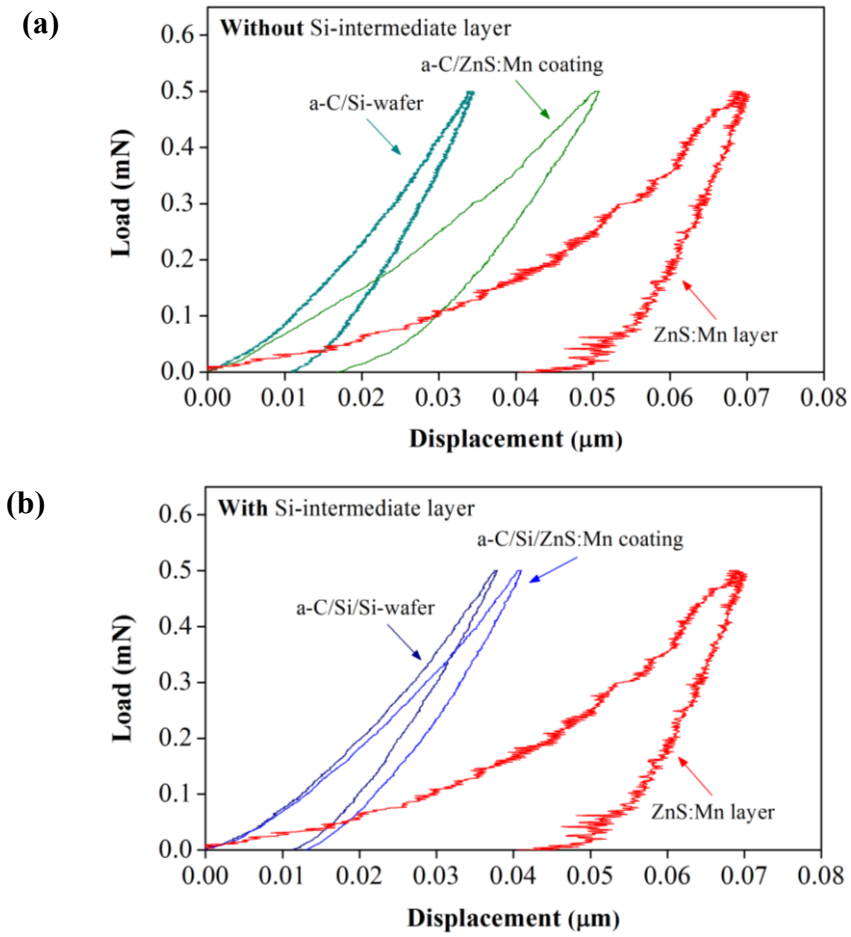

Fig. 2.19 Load-displacement curves of (a) a-C/ZnS:Mn and (b) a-C/Si/ZnS:Mn coatings as well as a-C films coated on Si-wafers and bare ZnS:Mn layer analysed by nanoindatation at the indented load 0.5 mN

Typically, strong interfacial bonding or adhesion can be attained easily between a-C and carbide- and silicide-forming substrates (such as Si, Ti, W and Cr). The adhesion of a-C coatings to other metallic and ceramic substrates may not be as strong but can be improved by the deposition of an intermediate layer as a bonding layer on these substrates prior to a-C deposition. The intermediate layers are typically selected from those elements that are known to be strong carbide- or silicide-formers such as Si, Ti, Cr and W. These elements can chemically react with the atoms of the substrate materials and thus insure

strong bonding [56]. In case of using Si-intermediate layer, it has been revealed that SiC was formed at the interface between a-C and Si-intermediate layer [57]. SiC shows strong chemical bonding and this result suggests that it was responsible for the good a-C film adherence on the silicon interlayer. Moreover, at the interface between substrate and Si-intermediate layer, the metallic silicide compound is formed, if the metallic substrate is used [58]. However, for ZnS:Mn layer substrate, the mutual solubilities of Si and Zn in the solid state are negligible as well as they do not unite to form a silicide [59]. In addition, though Si and S can form the sulphide compound, the bond energy of Si-S is found to be less than that of Si-C [60]. These can be probably accounted for the low adhesion between the coating and the ZnS:Mn layer.

After the friction test, the luminescence from the wear track was measured in order to demonstrate the wear-sensing capability. The photoluminescence (PL) spectra were measured from the wear tracks of both a-C/ZnS:Mn and a-C/Si/ZnS:Mn coatings. Figure 2.20(a) shows the PL spectrum detected from the wear track of a-C/ZnS:Mn coating. The single yellowish orange peak with the centre at 587 nm could be detected, which is similar to the spectrum of the as-fabricated ZnS:Mn layer. The similar spectrum is also obtained from a-C/Si/ZnS:Mn coating, in which the PL spectrum with the peak centre at 587 nm could be detected as shown in Fig. 2.20(b). The PL intensity of the spectrum detected from a-C/ZnS:Mn coating is higher than the intensity detected from the a-C/Si/ZnS:Mn coating, which is in agreement with the size of their wear tracks as shown in Fig. 2.18. It is also noted here that the PL spectra detected from the wear tracks correspond to the ZnS:Mn underlayer, but their intensity are less than the as-fabricated ZnS:Mn layer, if they are compared with the PL spectra in Fig. 2.15. This is because the exposure area to the excitation source (UV light) is different. The as-fabricated ZnS:Mn layer has larger exposure area since the whole surface of the coating is exposed to the UV light as already

presented in Fig. 2.10(a). After it is deposited with a-C film and subsequently subjected to the friction test until the wear reaching to the ZnS:Mn underlayer, the exposure area is confined to the wear track.

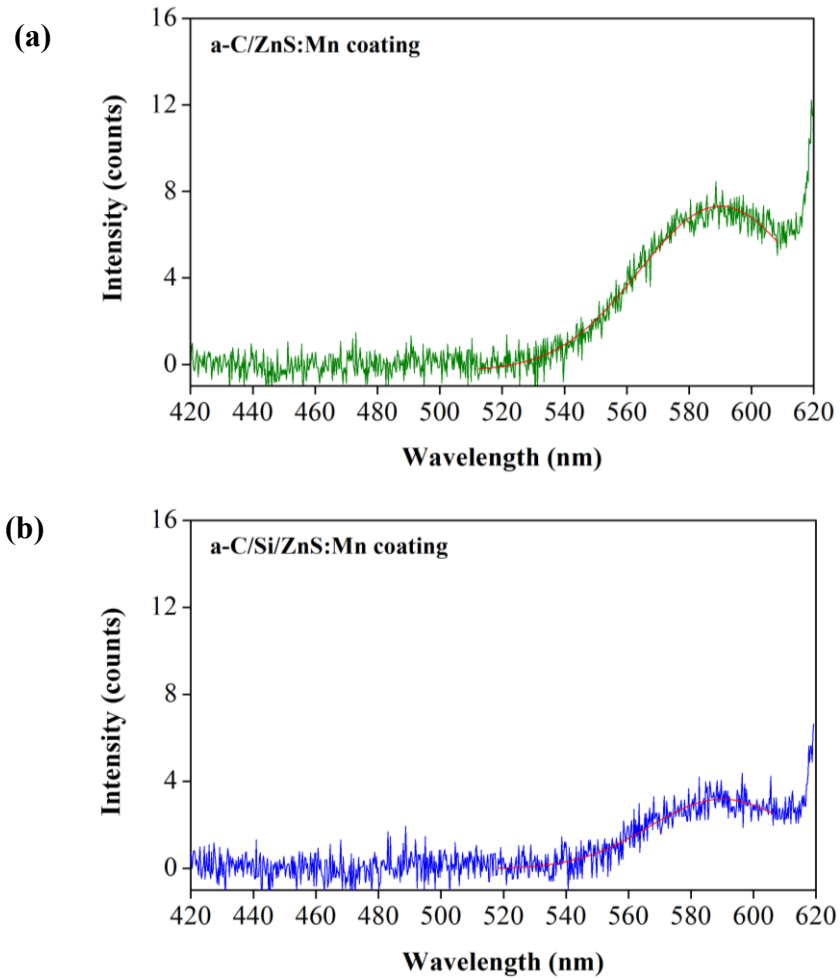

Fig. 2.20 Photoluminescence spectra measured from the wear tracks of (a) a-C/ZnS:Mn and (b) a-C/Si/ZnS:Mn coatings

2.4 Conclusion

In this chapter, the deposition of a-C films on Si-wafers by R.F. magnetron sputtering has been initially studied in order to determine the deposition rates by changing the Ar pressure during deposition. It was found that the deposition rate increased as the Ar pressure decreased from 10.0, 1.0 to 0.4 Pa, respectively. Moreover, the pressure during deposition influenced the physical and tribological properties of a-C films. The a-C films deposited at highest Ar pressure are softest and lowest wear resistant. As the Ar pressure decreased (1.0 Pa), the a-C films becomes harder and the wear resistant property was improved. However, the a-C films deposited at the lowest Ar pressure (0.4 Pa) shows the wrinkled surface, indicating the high residual compressive stress of the films. Therefore, the optimum condition for a-C deposition was at the Ar pressure of 1.0 Pa with the R.F. power of 100 W.

The luminescent ZnS:Mn films were also prepared by R.F. magnetron sputtering in order to fabricate the wear-sensing layer. The as-deposited ZnS:Mn films did not show luminescence due to the ineffective incorporation of Mn atoms in ZnS crystal. However, after the films were annealed at 700°C for 60 min in Ar atmosphere, the strong yellowish-orange luminescence could be detected. The luminescent property was enhanced because the post-annealing promoted the homogeneous incorporation of Mn atoms in the ZnS crystal and also improved the crystallinity by crystalline growth and elimination of the defects.

Finally deposition of a-C films onto the luminescent ZnS:Mn layer was carried out under the optimum conditions obtained from the early study. It was found that a-C films could be deposited onto the ZnS:Mn with the surface morphology conforming to the ZnS:Mn layer without any cracks or wrinkles formed on the surface. The structure of

a-C/ZnS:Mn coating was also similar to the typical a-C film as it was deposited on Si-wafer. The luminescence detected from the a-C/ZnS:Mn coating was almost disappeared due to the absorption of the excitation ray by a-C film. The similar results were also obtained for a-C/Si/ZnS:Mn coating. The friction test result of a-C/ZnS:Mn coating, even when a Si-intermediate layer was added, showed that a-C films completely worn out in the short sliding distance, indicating the adhesion strength between a-C film and ZnS:Mn layer was not sufficient. However, the luminescence was detected again from the wear track formed on the coating, which demonstrated the wear-sensing capability. It was found that the luminescence spectrum was similar to the spectrum measured from the as-fabricated ZnS:Mn layer, which correlated to the removal of a-C film.

2.5 References

[1] V. Kumar, M.K. Sharma, J. Gaur and T.P. Sharma : Chalcogenide Lett., **5** (2008) 289.

[2] M. Ladar, E.J. Popovici, I. Baldea, R. Grecu and E. Indrea : J. Alloys Compd., **434** (2007) 697.

[3] A. Goudarzi, G.M. Aval, S.S. Park, M.C. Choi, R. Sahraei, M.H. Ullah, A. Avane and C.S. Ha : Chem. Mater., **21** (2009) 2375.

[4] T. Shibata, K. Hirabayashi, H. Kozawaguchi and B. Tsujiyama : Jpn. J. Appl. Phys., **26** (1987) L1664.

[5] L.V. Zavyalova, A.K. Savin, and G.S. Svechnikov : Displays, **18** (1997) 73.

[6] H.F. Huang : Vacuum, **55** (1999) 127.

[7] B.P. Singh, V. Singh, R.C. Tyagi and T.P. Sharma : Appl. Surf. Sci., **254** (2008) 2233.

[8] M. McLaughlin, H.F. Sakeek, P. Maguire, W.G. Graham, J. Molloy, T. Morrow, S. Laverty and J. Anderson : Appl. Phys. Lett., **63** (1993) 1865.

[9] Z.J. Xin, R.J. Peaty, H.N. Rutt and R.W. Eason : Semicon. Sci. Technol., **14** (1999) 695.

[10] T.E. Varitimos and R.W. Tustison : Thin Solid Films, **151** (1987) 27.

[11] O. Agyeman, C.N. Xu, I. Usui, X.G. Zheng and M. Suzuki : Proc. SPIE, **4220** (2000) 350.

[12] A.H. Lettington and C. Smith : Diam. Relat. Mater., **1** (1992) 805.

[13] G.F. Zhang and X. Zheng : Surf. Coat. Tech., **82** (1996) 110.

[14] M.J. Mirtich, D. Nir, D. Swec and B. Banks : J. Vac. Sci. Technol. A, **4** (1986) 2680.

[15] A.F. Cattell and A.G. Cullis : Thin Solid Films, **92** (1982) 211.

[16] H.Y. Yu, C. Kim and S.C. Sanday : Thin Solid Films, **196** (1991) 229.

[17] X.D. Zhu, K. Narumi and H. Naramoto : J. Phys.: Condens. Matter, **19** (2007) 236227.

[18] K. Nimura, M. Nishimura, Y. Kashiwakura, Y. Itoh, A. Kumagai, A. Ueda, M. Ohsawa and K. Ozawa : IEEE Transl. J. Magn. Jpn., **9** (1994) 56.

[19] B. Marchon, J. Gui, K. Grannen and G.C. Rauch : IEEE Trans. Magn., **33** (1997) 3148.

[20] A.C. Ferrari and J. Robertson : Phys. Rev. B, **61** (2000) 14095.

[21] P.K. Chu and L. Li : Mater. Chem Phys., **96** (2006) 253.

[22] S.M. Rossnagel, M.A. Russak and J.J. Cuomo : J. Vac. Sci. Technol. A, **5** (1987) 2150.

[23] J.L. Andujar, F.J. Pino, M.C. Polo, A. Pinyol, C. Corbella and E. Bertran : Diam. Relat. Mater., **11** (2002) 1005.

[24] E. Mounier and Y. Pauleau : J. Vac. Sci. Technol. A, **14** (1996) 2535.

[25] L.G. Jacobsohn and F.L. Freire Jr : J. Vac. Sci. Technol. A, **17** (1999) 2841.

[26] M. Wang and J. Cheng : J. Alloys Compd., **504** (2010) 273.

[27] D. Theis, H. Oppolzer, G. Ebbinghaus and S. Schild : J. Cryst. Growth, **63** (1983) 47.

[28] J.M. Blackmore and A.G. Cullis : Thin Solid Films, **199** (1991) 321.

[29] X. Wu, F. Lai, Y. Lin, Z. Huang and R. Chen : Proc. SPIE, **6722** (2007) 67222L.

[30] M. Ashraf, S.M.J. Akhtar, A.F. Khan, Z. Ali and A. Qayyum : J. Alloys Compd., **509** (2011) 2414.

[31] M.K. Puchert, P.Y. Timbrell and R.N. Lamb : J. Vac. Sci. Technol. A, **14** (1996) 2220.

[32] T. Matsuoka, J. Kuwata, M. Nishikawa, Y. Fujita, T. Tohda and A. Abe : Jpn. J. Appl. Phys., **27** (1988) 592.

[33] T. Kryshtab, V.S. Khomchenko, J.A. Andraca-Adame, V.B. Khachatryan, M.O.

Mazin, V.E. Rodionov and M.F. Mukhlio : J. Cryst. Growth, **275** (2005) 1163.

[34] P.K. Ghosh, Sk.F. Ahmed, S. Jana and K.K. Chattopadhyay : Opt. Mater., **29** (2007) 1584.

[35] O. Agyeman, C.N. Xu, M. Suzuki and X.G. Zheng : J. Mater. Res., **17** (2002) 959.

[36] L.X. Shao, K.H. Chang and H.L. Hwang : Appl. Surf. Sci., **212** (2003) 305.

[37] Y.P. Venkata Subbaiah, P. Prathap and K.T. Ramakrishna Reddy: Appl. Surf. Sci., **253** (2006) 2409.

[38] N.J. Suthan Kissinger, N. Velmurugan and K. Perumal : J. Korean Phys. Soc., **55** (2009) 1577.

[39] Y.C. Huang, S.Y. Chang and C.H. Chang : Thin Solid Films, **517** (2009) 4857.

[40] R.C. Chang, F.Y. Chen, C.T. Chuang and Y.C. Tung : J. Nanosci. Nanotechnol., **10** (2010) 4562.

[41] M. Nose, Y. Deguchi, T. Mae, E. Honbo, T. Nagae and K. Nogi : Surf. Coat. Tech., **174** (2003) 261.

[42] S.H. Kim, H. Park, K.H. Lee, S.H. Jee, D.J. Kim, Y.S. Yoon and H.B. Chae : J. Ceram. Process Res., **10** (2009) 49.

[43] I. Yu, T. Isobe and M. Senna : J. Phys. Chem. Solids, **57** (1996) 373.

[44] T.T.Q. Hoa, N.D. The, S. McVitie, N.H. Nam, L.V. Vu, T.D. Canh and N.N. Long : Opt. Mater., **33** (2011) 308.

[45] W. Chen, R. Sammynaiken and Y. Huang : J. Appl. Phys., **88** (2000) 5188.

[46] B.H. Van, P.V. Ben, T.M. Thi and H.N. Nhat : Journal of Materials, (2013) 716452.

[47] R.N. Bhargava, D. Gallagher, X. Hong and A. Nurmikko : Phys. Rev. Lett., **72** (1994) 416.

[48] J.P. Borah and K.C. Sarma : Acta. Phys. Pol. A., **114** (2008) 713.

[49] Y. Su, G. Li, X. Bo and L. Li : Nanotechnology, **18** (2007) 485602.

[50] O. Brafman and S.S Mitra : Phys. Rev., **171** (1968) 931.

[51] M.D. Bhise, M. Katiyar and A.H. Kitai : J. Appl. Phys., **67** (1990) 1492.

[52] U. Kaiser, L. Chen, S. Geburt, C. Ronning and W. Heimbrodt : Nanoscale Res. Lett., **6** (2011) 228.

[53] M. Zhong, C. Zhang and J. Luo: Appl. Surf. Sci., **254** (2008) 6742.

[54] X. Li, D. Diao and B. Bhushan : Acta Mater., **45** (1997) 4453.

[55] O. Borrero-Lopez, M. Hoffman, A. Bendavid and P.J. Martin : Diam. Relat. Mater.,

19 (2010) 1273.

[56] A. Erdemir and C. Donnet : J. Phys. D: Appl. Phys., **39** (2006) R311.

[57] G. Capote, L.F. Bonetti, L.V. Santos, V.J. Trava-Airoldi and E.J. Corat : Thin Solid Films, **516** (2008) 4011.

[58] A. Grill, B. Meyerson and V. Patel : J. Mater. Res., **3** (1988) 214.

[59] R.W. Olesinski and G.J. Abbaschian : Bull. Alloy Phase Diagr., **6** (1985) 545.

[60] A. Haas : Angew. Chem. Int. Ed., **4** (1965) 1014.

CHAPTER 3

AMORPHOUS CARBON COATINGS WITH EPOXY RESIN UNDERLAYER CONTAINING ZnS:Cu PHOSPHOR

3. Amorphous carbon coatings with epoxy resin underlayer containing ZnS:Cu phosphor

3.1 Introduction

According to the experimental results presented in Chapter 2, it has been shown that the wear-sensing capability of a-C coatings with ZnS:Mn underlayer was feasible. The characteristic luminescence from the ZnS:Mn underlayer could be detected again when a-C films were completely worn out. However, the friction test result showed that the adhesion between a-C layer and ZnS:Mn layer was insufficient even though the Si-intermediate layer was added between them. This issue has led to the modification of luminescent ZnS-based layer with an improved adhesion property to a-C film. This can be feasibly achieved by utilising a composite structure, in which the luminescence ZnS particles are embedded in a transparent matrix coating.

Epoxy resin are a class of thermoset materials used extensively in structural and special composite applications because they offer a unique combination of properties such as high strength, low shrinkage, excellent adhesion to various substrates, effective electrical insulator, chemical and solvent inertness, low cost and low toxicity [1]. Furthermore, due to their chemical compatibility with most substrates and tendency to wet surface easily, these make them well suited to composites applications. Because of its high transparency especially in the visible region of the electromagnetic wave, epoxy resins have been also applied as an encapsulated matrix for the luminescence materials, such as CdSe/CdS/ZnS [2], ZnO [3] and YAG:Ce [4] for solid-state lighting. In mechanical applications, filling epoxy resin with hard materials, such as SiO_2 [5,6], TiO_2 [7], seems to be an attractive option for wear resistant material. In addition, filling the epoxy with carbon based fillers can enhance the tribological properties [8,9].

Deposition of a-C film onto polymer substrates is of interest for industrial applications since the applications of the polymer in the tribological applications have increased not only in the mechanical field [10,11], but also in the biomedical field [12,13], in which the wear resistant or chemical degradation improvement is enhanced. For epoxy resin substrates, plasma enhanced chemical vapour deposition (PECVD) [11] and plasma source ion implantation (PSII) [14] have been found to be the major methods for deposition of a-C films. Since these techniques are mainly based on chemical vapour deposition (CVD) process, it has been revealed that strong chemical reaction between the polymer substrate and deposited a-C layer was occurred [15,16] resulting in the change in structure of the final a-C coating. Therefore, this has led to the more beneficial gained by the physical vapour deposition (PVD) processes.

Through the PVD techniques, deposition of a-C film on epoxy resin by sputtering method has been studied [17]. However, the flake and spallation of a-C film are observed, indicating a poor adhesion of a-C film to the epoxy resin. Another method for a-C film deposition based on the PVD technique, which is by sublimation of fullerene (C_{60}) powder in electron beam excited plasma (EBEP) process [18,19]. In this technique, the fullerene powder is sublimated in argon plasma into the active carbon species. These species are accelerated by the negative bias voltage toward substrates and form a dense carbon film with good adhesion on the substrates. Furthermore, this technique is beneficial in high deposition rate as similar to another method like vacuum arc deposition.

Accordingly, the use of epoxy resin containing luminescent ZnS-based material powder (EP/ZnS:Cu) as a luminescent wear-sensing layer is studied in this chapter. Subsequently, a-C films are deposited onto the EP/ZnS:Cu layers by sublimation of C_{60} powder in EBEP method and pulsed vacuum arc deposition. The physical, tribological properties and wear-sensing capability are analysed and investigated.

3.2 Experimental

3.2.1 Fabrication of epoxy resin coatings containing ZnS:Cu phosphor (EP/ZnS:Cu)

Epoxy resin containing phosphor powder as a luminescent underlayer has been initially fabricated. As-purchased ZnS:Cu phosphor powder was used as a dispersive material. Fig. 3.1 shows the scanning electron microscopic (SEM) image of the ZnS:Cu phosphor powder. The powder has a rounded shape and shows agglomeration. The powder size as individual is found to be 10-20 μm. Epoxy resin used for the coating fabrication is Epofix from Struers. The base resin is composed of bisphenol-A, epichlorohydrin and oxirane, mono [(c12-14-alkyloxy) methyl] derivatives, whereas the hardener is mainly triethylenetetramine. ZnS:Cu powder was initially mixed with the base resin by simply stirring for 6 min. The weight ratio of ZnS:Cu powder to the base resin was 5 wt.%. The hardener with the weight ratio to the base resin of 3:25 was then added to the mixture and subsequently mixed for 6 min. The temperature during the mixing step was kept at 35°C. After that, the mixture was vacuum-degassed to remove the entrapped air for 15 min. A drop of the EP/ZnS:Cu mixture with an average weight of 30 mg was delivered onto the 15 mm × 15 mm silicon wafer (100) substrates. The mixture was then spread on the whole substrate surface by covering with polystyrene film. The coatings were finally cured in a hot-air rapid-drying oven at 40°C for 12 hr.

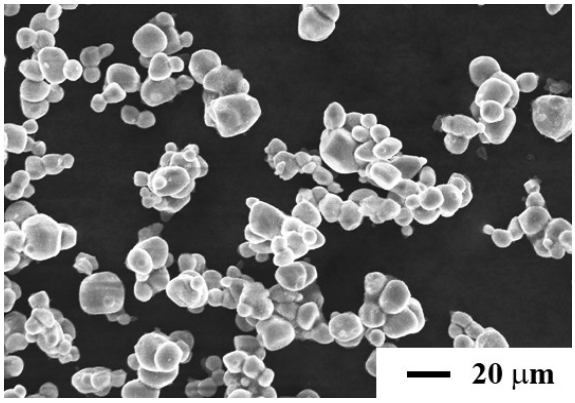

Fig. 3.1 SEM image of the as-purchased ZnS:Cu phosphor powder

3.2.2 Deposition of amorphous carbon (a-C) films

Amorphous carbon (a-C) films were deposited onto the EP/ZnS:Cu coatings by two deposition methods, namely, sublimation of fullerene (C_{60}) powder in electron beam excited plasma (EBEP) and pulsed vacuum arc deposition (VAD). For the EBEP technique, the deposition system is illustrated in Fig. 3.2. The C_{60} powder is sublimated in the high density argon plasma into the minute and active carbon species. These species are transported to and deposited on the substrates by negative bias voltage. The deposition conditions are summarised in Table 3.1. The main parameter in this study is substrate bias voltages (V_b), which are 0 and -200 V. For the VAD technique, the arc plasma gun unit consists of a graphite cathode, a trigger electrode and a cylindrical anode arranged coaxially as displayed in Fig. 3.3. The carbon plasma generated by the pulsed arc discharge on the cathode was moved forwardly to the grounded substrates along a concentric circular magnetic field around the anode induced by an arc current [20,21]. The deposition conditions are summarised in Table 3.2. For structural comparison, a-C films were also deposited onto the bare silicon wafer substrates by two deposition methods under the same conditions.

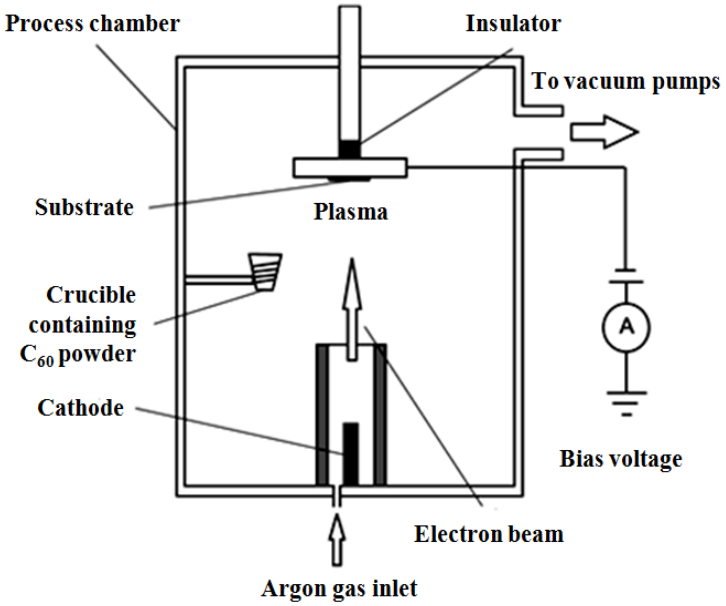

Fig. 3.2 Schematic diagram of the electron beam excited plasma (EBEP) deposition system for a-C films

Table 3.1 Deposition conditions for a-C films deposited by sublimation of C_{60} powder in electron beam excited plasma (EBEP) method

Parameters	**Corresponding values**
Substrate	EP/ZnS:Cu coated substrate, Si-wafer
Plasma gas	Argon (99.9999% purity)
Base pressure (Pa)	6.0×10^{-4}
Pressure during deposition (Pa)	6.0×10^{-2}
Discharge voltage (V)	55-60
Discharge power (kW)	1.8-2.0
Substrate position	350 mm above the plasma source
Argon plasma treatment	None
C_{60} sublimation temperature (°C)	850-900
Substrate bias voltage (V)	0 and -200
Deposition time (min)	60

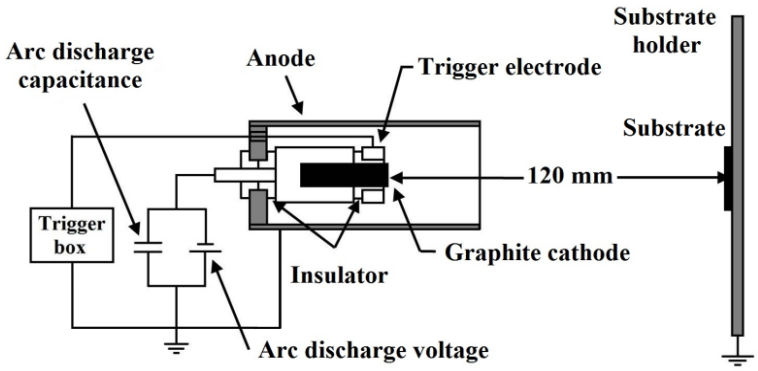

Fig. 3.3 Schematic diagram of vacuum arc deposition set-up for amorphous carbon films

Table 3.2 Deposition conditions for a-C films deposited by pulsed vacuum arc deposition (VAD) method

Parameters	**Corresponding values**
Substrate	EP/ZnS:Cu coated substrate, Si-wafer
Base pressure (Pa)	4×10^{-4}
Arc discharge voltage (V)	100
Capacitance of capacitor (μF)	720
Arc discharge frequency (Hz)	1.0
Numbers of discharges (Counts)	1000, 2000, 4000 and 6000
Substrate bias voltage (V)	None
T-S distance (mm)	120

3.2.3 Coating characterisations

Thickness of the coatings was measured with a scanning electron microscope (SEM) at a fractured surface. Structure of the coatings was analysed by Raman spectroscopy. The green laser with a wavelength of 532 nm was focused onto the coating surface with ×100 objective lens. Photoluminescence (PL) investigation of the coatings

was carried out by irradiating with a UV lamp at the excitation wavelength of 365 nm. The PL spectrum was collected through an optical fibre to a polychromator connected with a multichannel analyser and a personal computer. The tribological properties of the coatings were analysed with a ball-on-disk friction tester. The coatings were rubbed against stainless steel (SUS 440C) and alumina (Al_2O_3) balls 4.8 mm in diameter with a normal force of 0.77 N. The rotational speed was 50 rpm, which corresponded to the sliding speed of 13 mm/s. The sliding distance was kept at 50 m and the test was carried out in ambient atmosphere. Finally, wear track formed on coatings as well as the surface morphology was observed with an optical microscope equipped with a laser profilometer.

3.3 Results and discussion

3.3.1 As-fabricated EP/ZnS:Cu layers

As mentioned earlier in the experimental section that the method to fabricate the luminescent layers was by simply dropping the mixture of epoxy resin coatings containing ZnS:Cu phosphor powders (EP/ZnS:Cu) with a certain amount onto the Si-wafer substrates and covering with a polystyrene film. Fabrication of this coating by spin coating has also been tried beforehand. Although this technique can fabricate a thin coating, however, it was difficult to obtain the coating with smooth and flat surface because of the high viscosity of the epoxy resin and the agglomeration of the phosphor powder. To solve the problem of large surface roughness, the fabrication method as explained in the previous section was used. This method allows the mixture to spread freely throughout the surface of substrate with the flatness and surface morphology similar to the polystyrene film.

The thickness of the as-fabricated EP/ZnS:Cu coating measured by SEM at a fractured surface is shown in Fig. 3.4(a). As can be seen, the thickness of the coating is found to be 45-50 μm. The epoxy resin structure showed the homogenous layer without any defects, such as voids or entrapped air bubbles formed in the epoxy structure. Furthermore, no delamination of the epoxy resin coating from the substrate is observed along the interface, which suggested the well adhesion of the coating. The embedded ZnS:Cu particles could also be observed in the epoxy matrix. However, the agglomeration of the particles was still observed. Due to the fact that the coating was prepared by using the as-purchased powder as well as gentle mixing the powder and epoxy resin, the agglomeration of the particle could be sustained. In addition, the coating was also carried out by allowing the mixture to spread throughout the substrate surface freely under the covering with a polystyrene film. The thickness of the coating reduced gradually as the mixture was spreading. Finally it would be possible that the thickness was reduced to certain thickness at which was limited by the arrangement of the ZnS:Cu particles in the epoxy matrix. Fig. 3.4(b) shows the optical microscopic image of the as-fabricated EP/ZnS:Cu coating after curing and removing of the polystyrene film. Because of the high transparency of epoxy resin, the distribution of the ZnS:Cu particles can be observed. Moreover, the surface of the coating after curing was flat and smooth conformed to the covering films as evidenced by the surface profile measured with a laser profilometer shown in Fig. 3.4(c). The profile along the surface shows the flat profile with an average surface roughness of 0.04 μm, although it is scanned across the area that covers the ZnS:Cu particles.

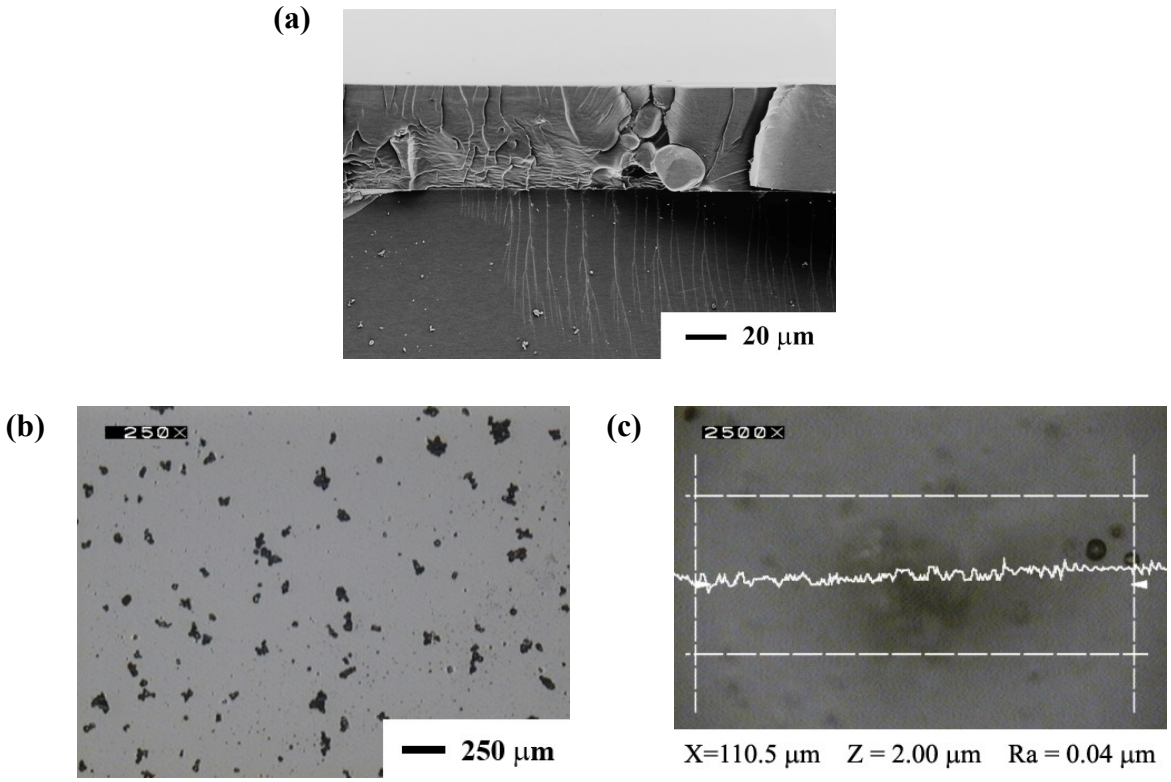

Fig. 3.4 (a) SEM image at the fractural surface of the as-fabricated EP/ZnS:Cu coating, (b) optical microscopic image of EP/ZnS:Cu coating after curing and removing of polystyrene and (c) surface profile of the coating measure by laser profilometer

The structure of EP/ZnS:Cu layer was analysed by Raman spectroscopy. Due to epoxy resin was the main composition of the coating as well as it was assumed that the chemical reaction between epoxy resin and the ZnS:Cu particles was not occurred because the powder was mixed physically with the resin, Raman spectrum was mainly taken from the epoxy resin region and the result is shown in Fig. 3.5. The strong peaks at 821, 1119, 1187, 1231, 1298, 1453 and 1603 cm^{-1} can be assigned to (CCH) aromatic ring, (CH) aromatic stretching, (CC) backbone stretching, (CO) stretching, (CH_2) twisting, (CH_2) scissoring and (C=C) aromatic ring buckling, respectively. These molecular bonds have been found to be the typical component in epoxy resin [22-24].

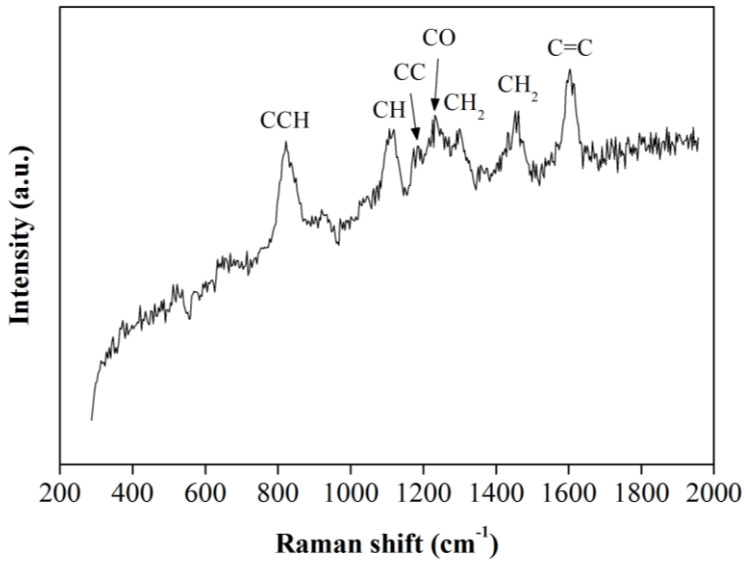

Fig. 3.5 Raman spectrum of the as-fabricated EP/ZnS:Cu coating

Photoluminescence (PL) from the coating was measured by irradiating the EP/ZnS:Cu coating with a UV light at the excitation wavelength of 365 nm. The luminescent spectra were collected directly from the coating surface with an optical fibre to the spectrometer. The PL spectrum of the coating is illustrated in Fig. 3.6(a). The emission spectrum shows the broad peak at 525 nm (green) and a shoulder at around 450 nm (blue), which is similar to emission characteristic of ZnS:Cu powders that were dispersed in epoxy resin [25,26] as shown in Fig. 3.6(b). The PL spectrum shows asymmetric shape indicating that the spectrum is a superposition of several peaks. Therefore, the spectrum has been deconvoluted using Gaussian curve fitting to reveal the spectra involved in the emission spectrum. The fitting results reveal that three main spectra located at 450 nm (blue), 515, and 528 nm (green) are involved. The fitted and summarised spectra are also plotted together with the measured spectrum in Fig. 3.6. The origin of luminescence mechanism from both green and blue peaks from ZnS:Cu phosphor

is explained due to the recombination of electron-hole between donor and acceptor pairs. In this study, the luminescent ZnS powder is doped with Cu and Al. Therefore, the green emission can be assigned to the Cu-Al pairs in ZnS crystals, while the blue emission has been occurred due to the self-activated centre or in the present of defect centres such as Zn or S vacancies [26,27].

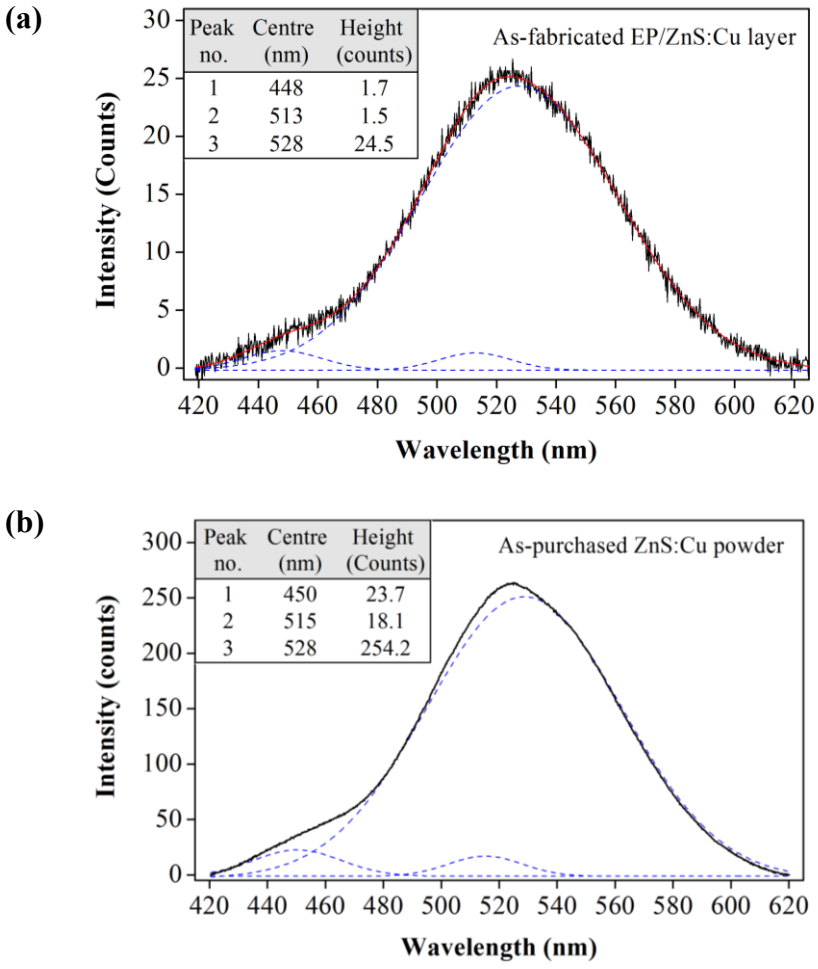

Fig. 3.6 Photoluminescence spectra of (a) as-fabricated EP/ZnS:Cu coating and (b) as-purchased ZnS:Cu phosphor powder under irradiated with UV light at 365 nm

3.3.2 a-C coatings with EP/ZnS:Cu underlayer deposited by sublimation of fullerene (C_{60}) powder in electron beam excited plasma (EBEP) method

As mentioned in the experimental section that a-C films were deposited onto the EP/ZnS:Cu coating layer by two deposition methods, i.e., sublimation of fullerene (C_{60}) powder in electron beam excited plasma (EBEP) and pulsed vacuum arc deposition (VAD) methods, respectively. In this section, sublimation of C_{60} powder in EBEP method is firstly focused. For this technique, it was suggested that the mechanical and tribological properties of a-C films were influenced by the substrate bias voltage (V_b) during depositing step [19]. Therefore, the deposition has been carried out at two bias voltages, namely 0 and -200 V.

The thicknesses of a-C films measured by SEM at the torn cross-section of the coatings are illustrated in Fig. 3.7. For the a-C films deposited at V_b of -200 V, the SEM images are shown in Fig. 3.7(a), while the films deposited at V_b of 0 V are shown in Fig. 3.7(b). For comparison, the thicknesses of a-C films deposited under both conditions on Si-wafers were also measured and their SEM images are displayed on the right side in each condition. The thicknesses of a-C films are summarised in Table 3.3. As can be seen from the results that the thickness of a-C films deposited by sublimation of C_{60} in EBEP at V_b of -200 V on EP/ZnS:Cu layer is significantly lower than the films deposited on Si-wafer, although both coatings were obtained from the same batch of deposition. In contrast, a-C films deposited on EP/ZnS:Cu layer at V_b of 0 V has nearly the same thickness to the films deposited on Si-wafer. The results published in the literature [19] show the thickness of a-C films increases when the V_b decreases from 0 V to -200 V and has a trend to decrease again when the V_b is lower than -200 V. This is found to be consistent with the results obtained in the present study, especially a-C films deposited on Si-wafers.

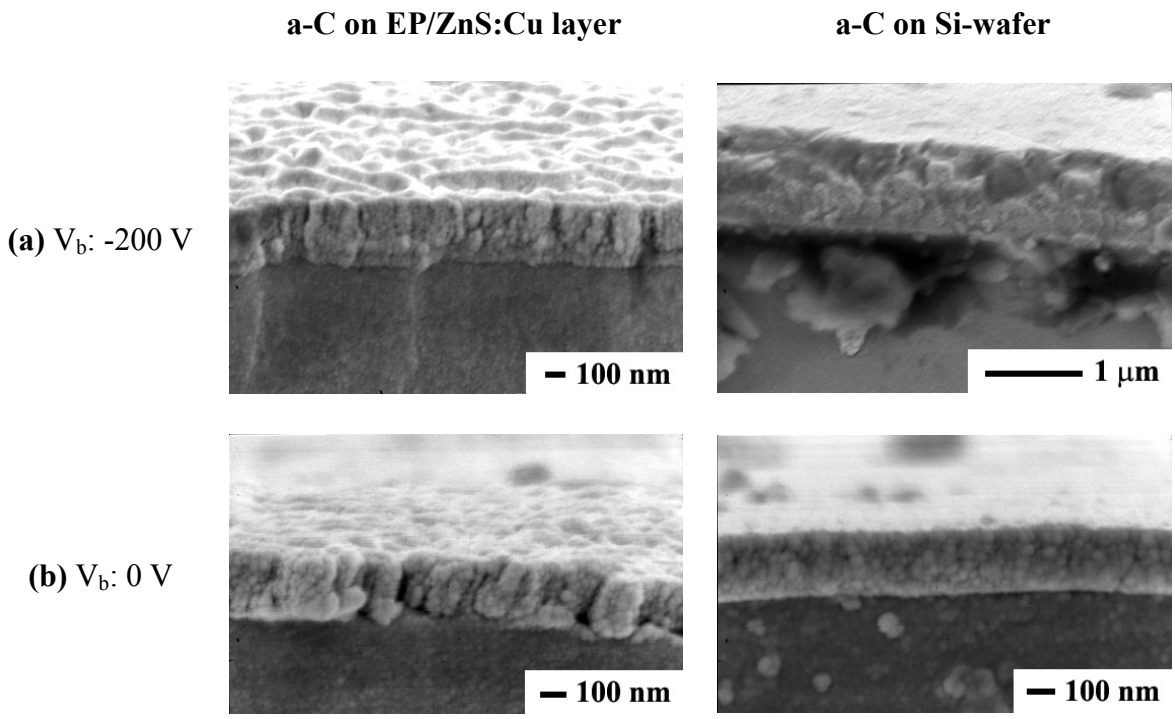

Fig. 3.7 SEM images at the fractured surfaces of a-C films deposited on EP/ZnS:Cu layer (left) and Si-wafer (right) by sublimation of C_{60} in EBEP method at bias voltage (V_b) of (a) -200 V and (b) 0 V

Table 3.3 Thicknesses of a-C films deposited on EP/ZnS:Cu layers and Si-wafers by sublimation of C_{60} in EBEP at bias voltages (V_b) of -200 and 0 V

Bias Voltage (V)	On EP/ZnS:Cu layers (nm)	On Si-wafers (nm)
-200	300	900
0	260	240

Surface topography of a-C film deposited on EP/ZnS:Cu layer at the V_b of -200 V observed with an optical microscope is displayed in Fig. 3.8(a). The surfaces of the coatings exhibit blistering and cratering texture. The similar result could also be observed for a-C film deposited on EP/ZnS:Cu at the V_b of 0 V as shown in Fig. 3.8(b). The surface

profiles scanned across the defects formed on both coatings are shown in Fig. 3.8(c). There are two types of defects formed on the coatings, large blistering and small cratering. For a-C films deposited on EP/ZnS:Cu layer at the V_b of -200 V, both types of textures are formed, whereas the films deposited at the V_b of 0 V show mainly a small cratering texture. It was found that the objects that located under the large blister were the ZnS:Cu particles observed by focusing the objective lens through sublayer. For the cratering surface, nothing could be seen beneath the surface. In contrast, a-C films deposited on Si-wafers show a smooth surface without defects.

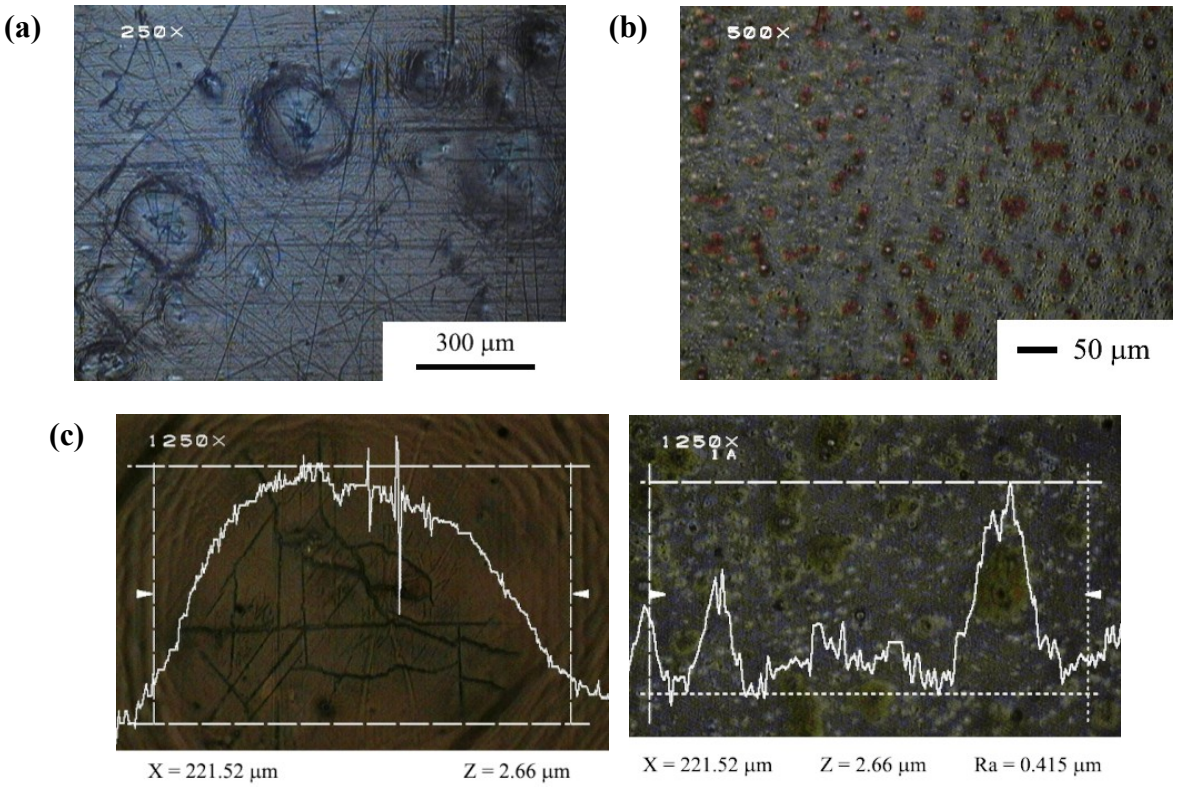

Fig. 3.8 Optical microscopic images observed at surfaces of a-C coatings with EP/ZnS:Cu underlayer deposited by sublimation of C_{60} in EBEP method at V_b of (a) -200 V and (b) 0 V as well as (c) defective surface profiles formed on the coatings

From both SEM images at the cross-sections and optical microscopic images at the surfaces of a-C films deposited on EP/ZnS:Cu layers, it is likely that the formation of defective textures occurs during the deposition process. This is evidenced by comparison with the surface texture of the as-fabricated EP/ZnS:Cu, which is flat and smooth, although the profile was scanned across the position that contained the phosphor particle at subsurface as shown in Fig. 3.4(c). It seems that there is an interaction between plasma, coating species and surface of EP/ZnS:Cu layer. To prove this hypothesis, the structural analyses of the a-C films deposited on EP/ZnS:Cu layers were carried out and compared with a-C films deposited on Si-wafers.

Structures of a-C films deposited on EP/ZnS:Cu layer and Si-wafer at the V_b of -200 V analysed by Raman spectroscopy are shown in Fig. 3.9(a). The Raman spectrum of a-C film deposited on Si-wafer exhibits a broad band with the highest peak at 1540 cm^{-1} (G band) and a shoulder at 1380 cm^{-1} (D band), which is similar to the Raman spectrum of general hard a-C film [18, 28-30]. In contrast, Raman spectrum of a-C film deposited on EP/ZnS:Cu layer exhibits only a strong luminescent background without an observable or identical peak of a-C structure. For the a-C film deposited on EP/ZnS:Cu layer at V_b of 0 V, although a strong luminescent background is also obtained, an observable peak located at 1560 cm^{-1} can be observed as shown in Fig. 3.9(b). Comparison with a-C film deposited on Si-wafer under the same condition, a similar peak at 1560 cm^{-1} was also observed. However, due to a strong luminescent background obtained in the spectrum of a-C deposited on EP/ZnS:Cu layer, the shape of spectrum is not clearly obtained. In addition to the Raman spectrum of a-C film deposited on Si-wafer at V_b of 0 V, the additional peak at 1440 cm^{-1}, which can be assigned as the A_g active mode peak of fullerene (C_{60}) can also be observed [31]. This indicates that the degree of C_{60} decomposition was not enough during deposition. As a result, C_{60} molecules still maintain their structure in the film. However,

when the deposition was carried out at V_b of -200 V, this peak is disappeared and the structure approaches to the typical a-C structure as shown in Raman spectrum of a-C film deposited on Si-wafer in Fig. 3.9(a). The structural change of a-C films due to the bias voltage can be correlated with the deposition energy of the incident ions [30,32]. Therefore, it can be stated that the stronger interaction between plasma, ion species and the substrate was occurred for the deposition at the V_b of -200 V than at 0 V.

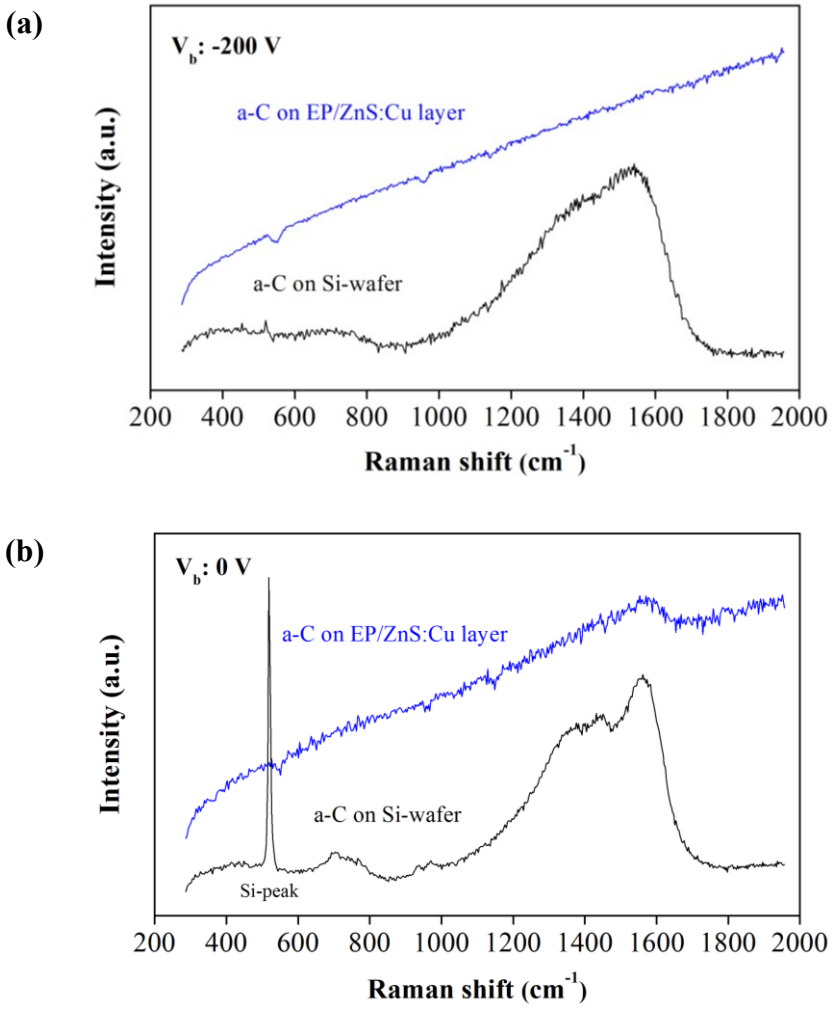

Fig. 3.9 Raman spectra obtained from a-C coatings with EP/ZnS:Cu underlayer and on Si-wafers deposited by sublimation of C_{60} in EBEP method at V_b of (a) -200 V and (b) 0 V

According to the results on Raman spectrum of a-C film deposited on EP/ZnS:Cu layer at V_b of -200 V shown in Fig. 3.9(a), the strong luminescent background is appeared without the identical peaks that indicate the structure of a-C films. The strong luminescent background in Raman spectra of a-C films is generally found in the soft a-C films with high content of hydrogen or so called "polymer-like carbon" [33-35]. In contrast, this luminescent background peak is not observed on the Raman spectrum of a-C film on Si-wafer, which is deposited in the same batch. The similar results are also obtained on the Raman spectra of a-C film deposited at V_b of 0 V as shown in Fig. 3.9(b). In addition, the hydrogen gas was not supplied during deposition in this study. Therefore, it is possibly that the source of hydrogen atoms that were contained in the a-C films is from the epoxy resin substrate.

Jones and Ojeda [16], has demonstrated the effects of the epoxy resin as the intermediate layer on the surface structure of a-C films deposited by plasma-enhanced chemical vapour deposition (PECVD). It was found that the main atomic components of epoxy resin, such as carbon, oxygen, calcium, nitrogen, and sodium measured by XPS analysis, were found as the additional composition in the deposited a-C films. The presence of these elements in the film is related to the degree of migration through the deposited films. Furthermore, other interactions, such as outgassing, heating and sputtering of the epoxy resin, could also occur within the plasma during the coating process. These processes result in the subsequent deposition of those elements concurrently with a-C films. This suggestion is well consistent with the results found in this study, although the hydrogen atoms could not be traced by the XPS analysis. However, due to the fact that epoxy resin is the hydrocarbon compound, it is presumable that the hydrogen can also migrate or transfer to the deposited a-C films during deposition. Since the a-C films deposited at V_b of -200 V, the degree of interaction between the argon ions in the plasma

and the substrates is considerably stronger than the a-C films deposited at V_b of 0 V. As a result, the degree of surface damage becomes more severe as shown in Fig. 3.8 as well as the structure of the final coating is not a typical hard a-C film as evidenced by Raman spectra shown in Fig. 3.9.

Photoluminescence (PL) characteristics of the coatings after deposition of a-C films were investigated by irradiating with a UV light at 365 nm. The PL spectra from the coatings deposited under two conditions are plotted in Fig. 3.10. It is noted that the luminescence was measured at the same EP/ZnS:Cu layer sample before and after it had been deposited with a-C films. The spectrum of the coating after being coated with a-C film was plotted relatively to the spectrum obtained before being coated with a-C film. As can be seen from the PL spectra, the as-fabricated EP/ZnS:Cu layer exhibits a strong green luminescence similar to a spectrum shown in Fig. 3.6. After a-C films have been deposited onto the EP/ZnS:Cu layer at both conditions, the luminescence from the coatings disappears as evidenced by the PL spectra that show only a flat background without any observable peaks.

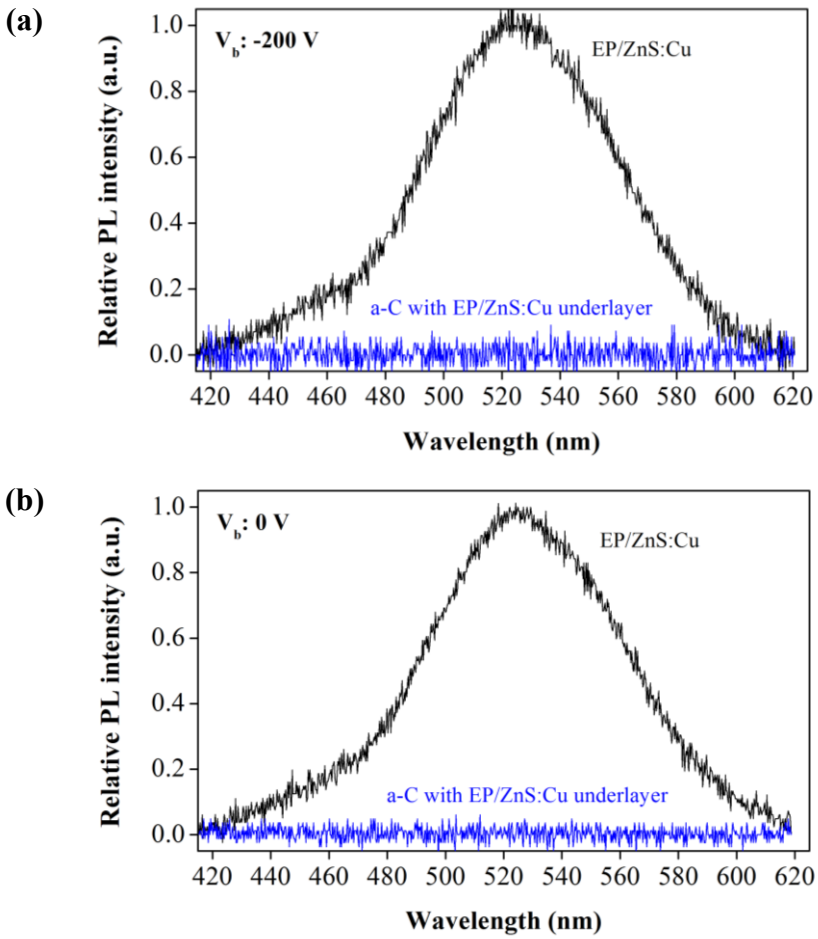

Fig. 3.10 Photoluminescence spectra of EP/ZnS:Cu before and after being deposited with a-C films by sublimation of C_{60} in EBEP method at V_b of (a) -200 V and (b) 0 V

The wear-sensing capability of a-C coatings with EP/ZnS:Cu underlayer is subsequently investigated by generating a wear track on the coating and then measuring the intensity of luminescence from the wear track. The wear track was generated through a friction test with a ball-on-disk friction tester. The testing conditions are listed in Table 3.4. From the friction test, not only the wear track is formed on the coating, but also the friction characteristic of the coating can also be determined.

Table 3.4 Ball-on-disk friction test conditions for a-C films deposited by sublimation of C_{60} in EBEP method

Ball:	Stainless steel (SUS 440C) (∅ 4.8 mm)
Normal load (N):	0.3
Sliding speed (mm/s):	13
Atmosphere:	Ambient air

Figure 3.11(a) illustrates the friction characteristics of a-C films with EP/ZnS:Cu underlayer deposited by sublimation of C_{60} in EBEP at V_b of -200 V. The friction tests were also carried out on a-C films deposited on Si-wafers deposited under the same conditions for comparison. The coefficients of friction (COF) of a-C film with EP/ZnS:Cu underlayer reaches to the steady stage at higher value of 0.7 quickly in the beginning of the test, while a-C film deposited on Si-wafer shows a stable COF value at 0.2 entire the test. Similar low friction behaviour of a-C film deposited on Si-wafer is found in the literatures [18], suggesting the typical characteristic of hard a-C film. However, a totally different behaviour is obtained for a-C film with EP/ZnS:Cu underlayer. In case of a-C film with EP/ZnS:Cu underlayer deposited at V_b of 0 V, the COF gradually increases from 0.2 in the beginning to 0.5 in the first 10 metres of sliding distance. Then the COF further increased and quickly reached a steady stage at the value of 0.7 until the test was finished as shown in Fig. 3.11(b). For the a-C film deposited on Si-wafer under this condition, the coating presents a low COF at around 0.1 at the beginning and early stage of the test. The fluctuation of the COF within the range of 0.1-0.2 is then observed after a few metres of sliding distance. Finally, after the sliding distance has reached to 25 m, the low COF at 0.1 is obtained and kept stable at this value until the test is finished.

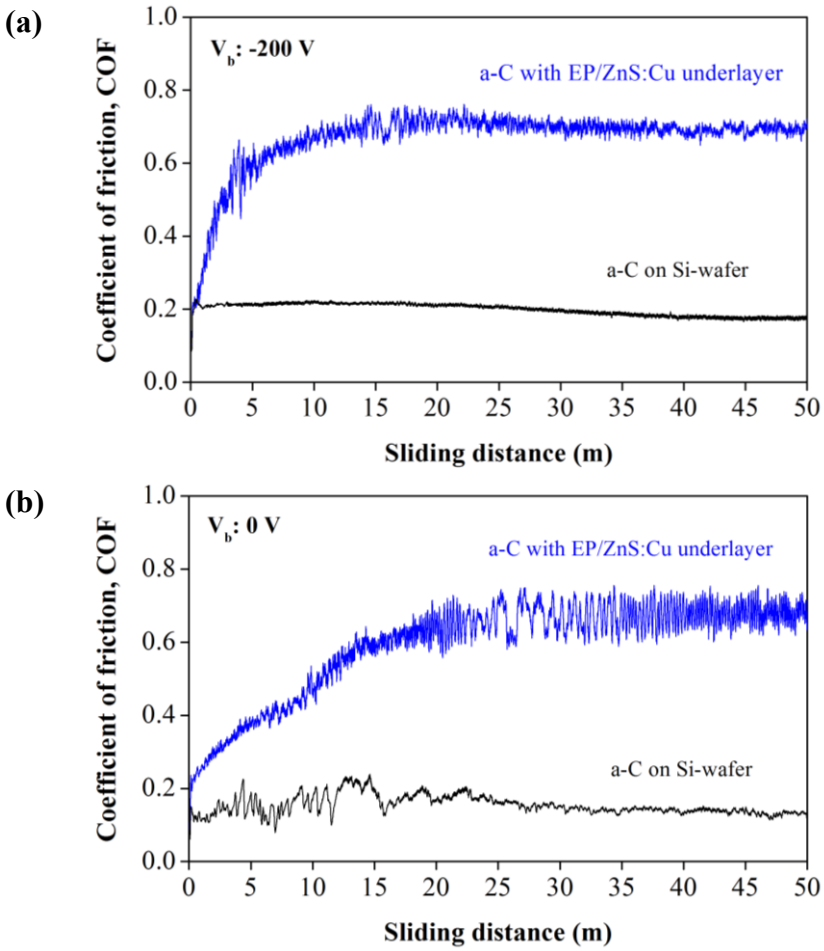

Fig. 3.11 Friction behaviours of a-C coatings with EP/ZnS:Cu underlayer and on Si-wafers deposited by sublimation of C_{60} in EBEP method at V_b of (a) -200 V and (b) 0 V

The corresponding wear tracks formed on the surface of the coating are presented in Fig. 3.12. The wear track of a-C film with EP/ZnS:Cu underlayer deposited at V_b of -200 V reveals the completely removal of a-C layer from EP/ZnS:Cu as can be seen in Fig. 3.12(a). The ZnS:Cu phosphor particles that are embedded in the epoxy matrix are also exposed to the surface. On the other hand, the wear track of a-C film deposited on Si-wafer at the same bias voltage is hardly observed as shown in Fig. 3.12(b), suggesting a superb wear resistance of the a-C film. In case of a-C film with EP/ZnS:Cu underlayer deposited at V_b of 0 V, a similar wear track with the previous a-C film is observed. The coating is

mostly worn out reaching to the EP/ZnS:Cu underlayer as shown in Fig. 3.12(c). However, the width of the wear track is narrower comparing with the wear track of the coating deposited at V_b of -200 V, suggesting the improved wear resistance properties. This is also consistent with the friction test result as already presented in Fig. 3.11(b), in which the COF of coating approached the steady state at higher value at longer sliding distance. Figure 3.12(d) shows the wear track of a-C film deposited on Si-wafer at V_b of 0 V. It also shows that a-C film has been completely worn out, resulting in the Si-wafer surface exposed.

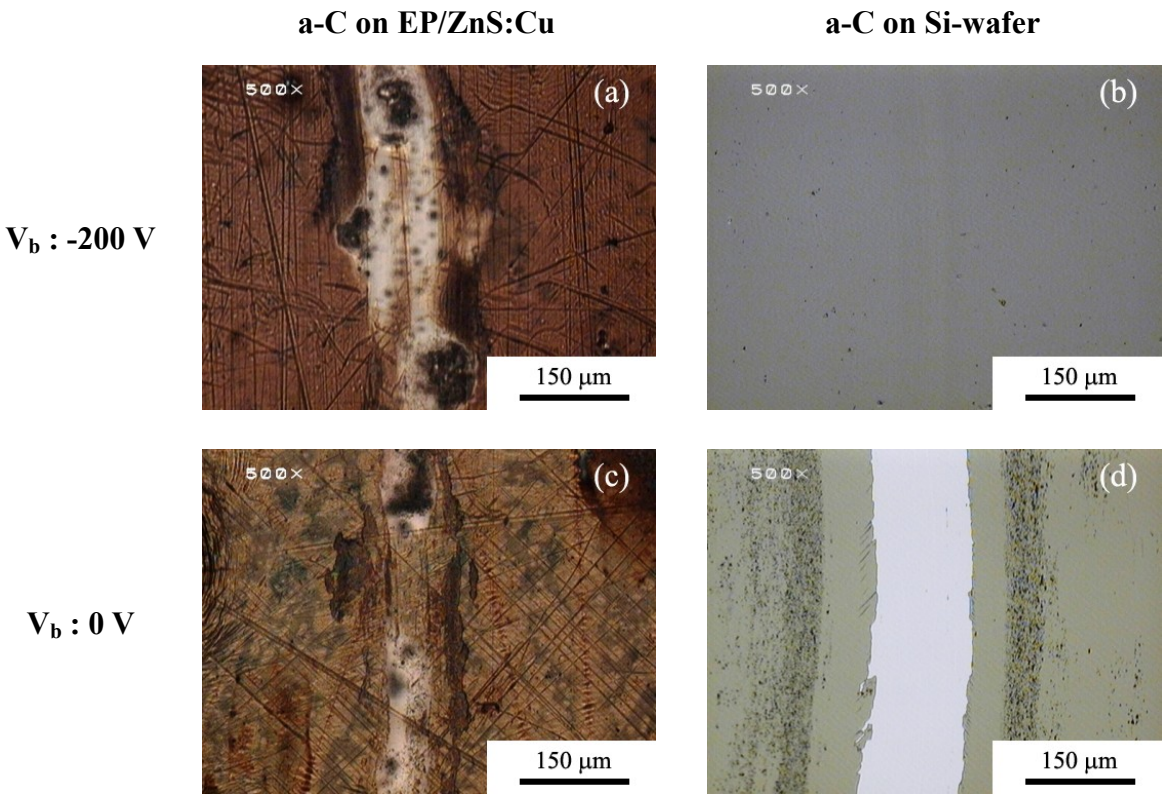

Fig. 3.12 Optical microscopic images of the wear tracks formed on the surfaces of a-C coatings with EP/ZnS:Cu underlayer and on Si-wafer deposited by sublimation of C_{60} in EBEP method at V_b of (a, b) -200 V and (c, d) 0 V, respectively

After the friction test, the photoluminescence (PL) spectra were collected from the wear tracks of the coatings in order to confirm the sensing capability. Figure 3.13(a) shows the PL spectrum detected from the wear track of a-C film with EP/ZnS:Cu underlayer deposited at V_b of -200 V. The spectrum exhibits a broad peak at 526 nm with a small shoulder at 451 nm, which is similar to the PL spectrum of as-fabricated EP/ZnS:Cu layer as shown in Fig. 3.6. This suggests that a-C film has been completely worn out, resulting in the EP/ZnS:Cu underlayer exposes to the UV excitation and simultaneously emits luminescence. The similar result was also obtained for the coating deposited at V_b of 0 V. The PL spectrum with the peak centre at 525 nm is obtained as shown in Fig. 3.13(b). The intensity is slightly lower and the shape of spectrum is slightly different from the spectra obtained in Fig. 3.13(a) because the degree of removal of a-C film was lower than the coating deposited in previous condition as evidenced by the optical microscopic image of the wear track in Fig. 3.12(c).

In summary, it is apparent from the results that deposition of a-C films on EP/ZnS:Cu layers by sublimation of C_{60} in EBEP resulted in the blistering and cratering textures formed on the surface. Moreover, it was also found that a-C films with EP/ZnS:Cu underlayer showed the soft polymer-like structure, which was different from hard type a-C structure found in a-C films deposited on Si-wafers. As a result, the high coefficient of friction (COF) and low wear resistant properties of a-C films were obtained.

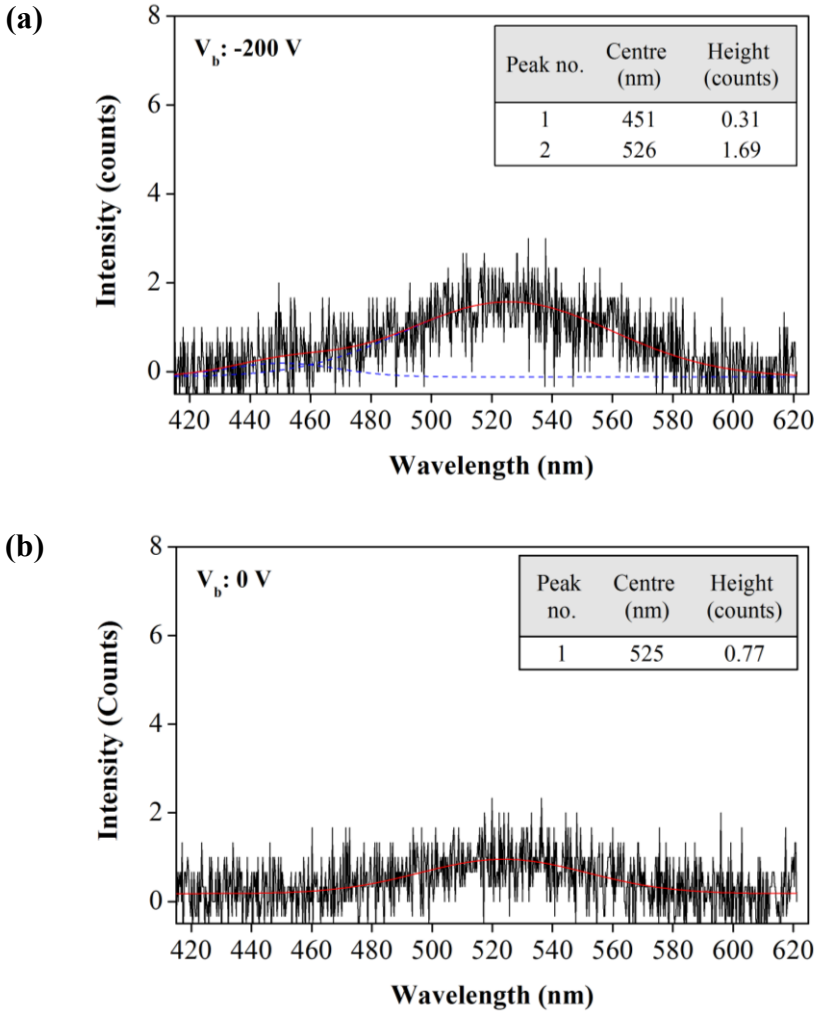

Fig. 3.13 Photoluminescence spectra detected from the wear tracks after the friction test of a-C coatings with EP/ZnS:Cu underlayer deposited by sublimation of C_{60} in EBEP method at V_b of (a) -200 V and (b) 0 V

3.3.3 a-C coatings with EP/ZnS:Cu underlayer deposited by pulsed vacuum arc deposition (VAD) method

According to the experimental results shown in the previous section, deposition of a-C films in continuous plasma processing led to the degradation of physical and tribological properties of the final a-C coatings with EP/ZnS:Cu underlayer because of the

interaction between plasma and EP/ZnS:Cu layers. To avoid the interaction with the continuous plasma, pulsed vacuum arc deposition (VAD) was selected for the deposition method and the results on physical properties of a-C films deposited on EP/ZnS:Cu layers are presented in this section.

The deposition condition has been summarised in Table 3.2, in which the discharge voltage, capacitance, and frequency were kept at 100 V, 720 μF and 1 Hz, respectively. Initially, the deposition was carried out at 6000 pulses of discharge to determine the deposition rate. The thicknesses of a-C films deposited on EP/ZnS:Cu as well as Si-wafer measured by SEM at cross-sections are shown in Fig. 3.14. The thickness of a-C film on EP/ZnS:Cu layer is 240 nm as shown in Fig. 3.14(a), which is nearly equal to a-C film on Si-wafer (230 nm) as shown in Fig. 3.14(b). The corresponding deposition rates of 0.04 nm/pulse could be obtained for a-C films deposited under this condition. It was also found that the adhesion between a-C film and EP/ZnS:Cu substrate was considerably good since no delamination or removal of a-C film from the EP/ZnS:Cu substrate could be observed along the interface of the coating.

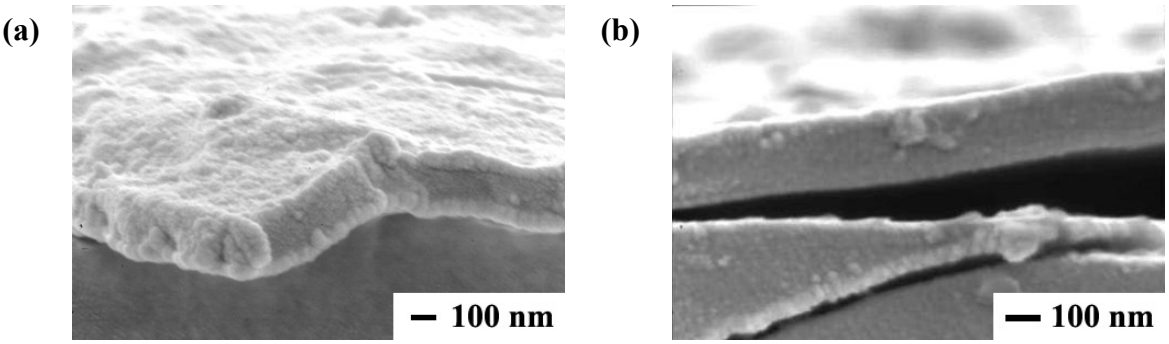

Fig. 3.14 SEM images of fractured surfaces of a-C deposited on (a) EP/ZnS:Cu layer and (b) Si-wafer by pulsed VAD method at 6000 pulses of discharge

The surface morphology of a-C coating with EP/ZnS:Cu underlayer is shown in Fig. 3.15(a). The scratch lines on the surface correspond to the randomly cracked network. These cracks are observed on the coating surface after it was taken out from the deposition chamber. The surface profile scanned across the crack and normal surface of a-C films is shown in Fig. 3.15(b). The profile reveals the corrugated texture formed on the coating surface between the grooves of cracks. In case of a-C film deposited on Si-wafer, cracking was not observed on the surface of the coating. However, instead of corrugated texture, a buckling surface or wrinkle is found randomly on the surface of a-C films as presented in Fig. 3.15(c). The wrinkled surface is occasionally found on the a-C film due to the high compressive stress of the film [36-38], resulting in delamination or spalling of the coating from the substrate as evidenced by Fig. 3.14(b). On the other hand, delamination of the a-C coating was not observed when it was deposited on EP/ZnS:Cu layer. This indicates the a-C film adhere well to the EP/ZnS:Cu layer. Due to the high compressive stress of a-C film and low strain energy of polymer surface, deposition of a-C film on EP/ZnS:Cu layer also provides a large difference in elastic moduli between the film and substrate as confirmed by the Young's moduli of both EP/ZnS:Cu layer and a-C film measured by nanoindentation in Table 3.5. As a result, cracks and corrugated texture are formed on the coating surface [39,40].

Table 3.5 Hardnesses and Young's moduli of epoxy resin layer and a-C film deposited by pulsed VAD at 6000 pulses of discharge measured by nanoindentation method

Coating	**Hardness (GPa)**	**Young's modulus (GPa)**
Epoxy resin coating	0.25	5.3
a-C film	38.87	255.0

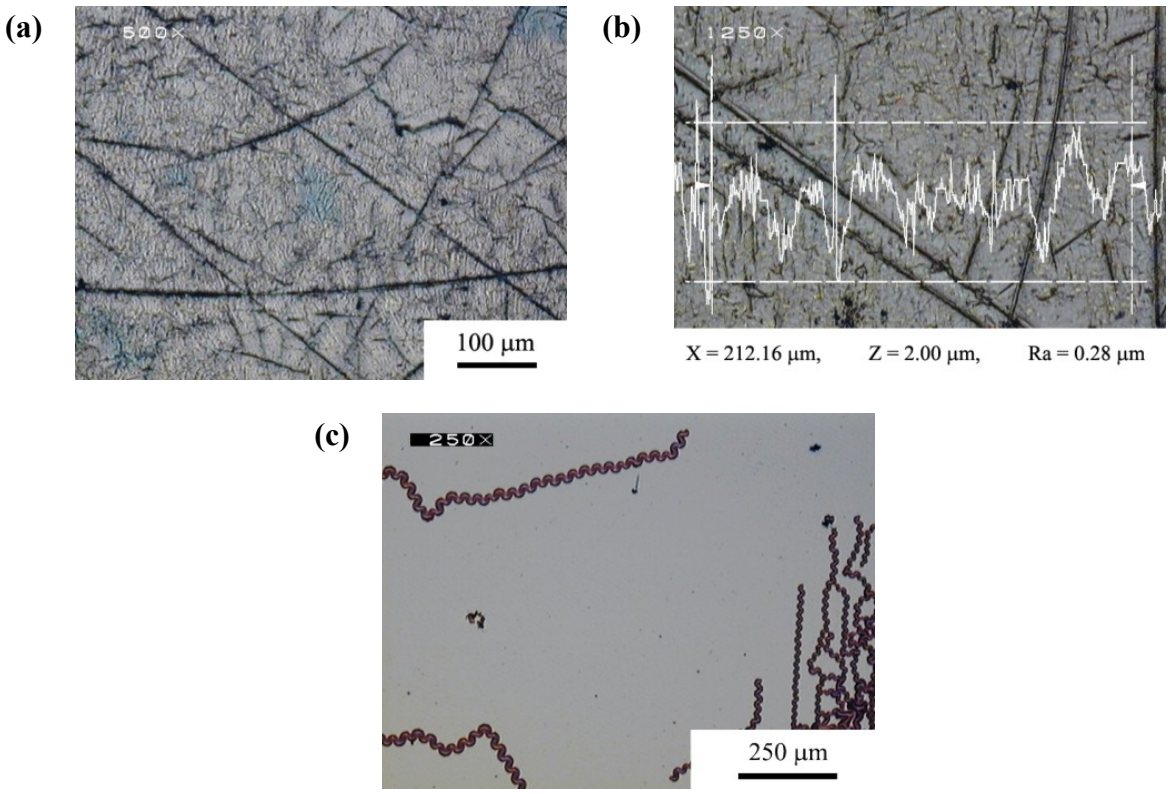

Fig. 3.15 (a) Optical microscopic image and (b) surface profile scanned across the surface of a-C coatings with EP/ZnS:Cu underlayer and (C) optical microscopic image of a-C film deposited on Si-wafer by pulsed VAD method at 6000 pulses of discharge

Either crack network or corrugated texture of the coating is typical features of hard coatings deposited on soft and flexible substrates such as rubber and polymer [41]. It is also suggested that during deposition and especially cooling down of the coated substrates, cracks may initiate and randomly propagate in the coatings due to the difference in thermal expansion between a-C coating and polymer substrate [10,13]. Although the a-C film was deposited on the floating substrate in ambient temperature, the temperature of the EP/ZnS:Cu substrates could be raised up due to the bombardment of energetic carbon species. However, it is presumed that the degree of rising up is not as high as it could damage the epoxy resin substrate because there was no evidence of blistering or cratering

textures formed on the surface of the coating like they were found in the previous experiment (Fig. 3.8).

The structure of a-C film deposited on EP/ZnS:Cu layer analysed by Raman spectroscopy is presented in Fig. 3.16. The spectrum exhibits a single broad peak with a peak centre at 1550 cm^{-1}. Moreover, a small peak at 821 cm^{-1} and a shoulder peak ranging from 1200 to 1400 cm^{-1} are also apparent on the spectrum. The latter peaks can be assigned to phonon scattering from the epoxy resin underlayer. For comparison, Raman spectrum of a-C film deposited onto Si-wafer with the same deposition condition is also shown in the same figure. The spectrum also shows the similar broad peak at centre of 1550 cm^{-1}, which is assigned to the G band of amorphous carbon structure. The shoulder at around 1350 cm^{-1}, which corresponds to the D band, was not dominant. The peaks ranging from 475-570 cm^{-1} and 900-1000 cm^{-1} are the peaks given by the silicon wafer substrate. Each Raman spectrum of both a-C films deposited on the substrate with and without EP/ZnS:Cu underlayer has a broad and nearly symmetric G peak centred at around 1550 cm^{-1} suggesting the non-hydrogenated amorphous structure with high content of sp^3 carbon bonds in the films [42,43]. This leads to the transparency of a-C film to the laser wavelength (532 nm) of Raman probe [44]. Therefore, the additional Raman peaks from the substrate can also be observed on the Raman spectrum.

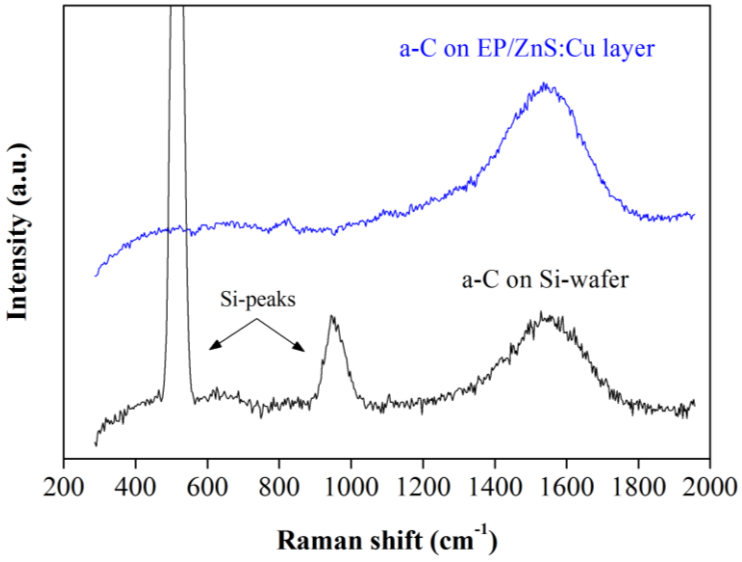

Fig. 3.16 Raman spectra of a-C film with EP/ZnS:Cu underlayer and on Si-wafer deposited by pulsed VAD at 6000 pulses of discharge

Photoluminescence (PL) characteristics of the EP/ZnS:Cu layers before and after deposition of a-C films by pulsed VAD were investigated by irradiating with a UV light at 365 nm. The PL spectra of the coatings are plotted in Fig. 3.17. It is noted here again that the luminescence was measured from the same EP/ZnS:Cu layer sample before and after it had been deposited with a-C films. The spectrum of the coating after being coating with a-C film was plotted relatively to the spectrum obtained before being deposited with a-C films. The PL spectra shows that the EP/ZnS:Cu layers exhibits a strong green luminescence with the peak centre at 525 nm and a small blue shoulder at around 450 nm. After a-C films has been deposited onto the EP/ZnS:Cu layer by pulsed VAD method at 6000 pulses of discharge, the luminescence from the coatings disappears as evidenced by the PL spectra of a-C deposited on EP/ZnS:Cu layer.

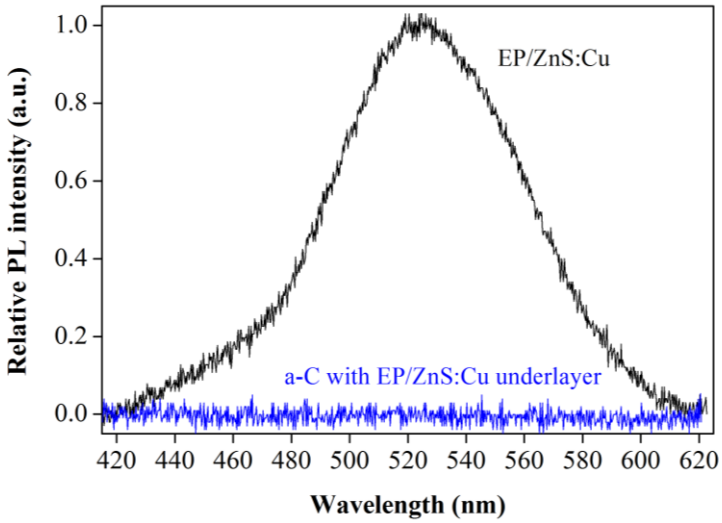

Fig. 3.17 Photoluminescence spectra of EP/ZnS:Cu coatings as-fabricated and after being coated with a-C films by pulses VAD method at 6000 pulses of discharge

Considering the Raman spectra of a-C films deposited on Si-wafer in Fig. 3.16, the additional peaks that originated by Si-wafer at 520 and 950 cm^{-1} are also appeared on the spectrum of a-C films. This indicates that a-C films have transparency to the laser wavelength of the Raman spectrometer at 532 nm, which corresponds to the green light. This implies that the green light can pass through the a-C film. Similarly, the PL spectrum of EP/ZnS:Cu layer also emits the green luminescence at 525 nm, which is near to the laser wavelength of the Raman probe. Therefore, the luminescence spectrum from the EP/ZnS:Cu underlayer should have been detected although the a-C film is deposited on it. However, the luminescence is undetected from such coating. Considering the optical absorption spectra of a-C film as shown in Fig. 1.12 [45], the absorption coefficient of a-C film to the light in UV range is approximately 10 times higher than in the visible range. This indicated that the UV excitation ray is absorbed by a-C layer leading to the prevention of the luminescence from the EP/ZnS:Cu underlayer.

Friction test was conducted by a ball-on-disk friction test in order to examine the tribological properties. The friction test condition are summarised in Table 3.6. It is further noted here that the wrinkles are occasionally formed on the surface of as-deposited a-C films on Si-wafers due to the high compressive stress as already shown in Fig. 3.15(c). As a result, delamination or spalling of the a-C film was observed. The friction test could not be able to carry out on such coatings. Therefore, a thin nickel intermediate layer (~20 nm) was added between a-C film and Si-wafer in order to suppress the formation of wrinkle.

Table 3.6 Ball-on-disk friction test conditions for a-C coatings deposited by pulsed VAD method

Ball:	Stainless steel (SUS 440C) and Alumina (∅ 4.8 mm)
Normal load (N):	0.77
Sliding speed (mm/s):	13
Atmosphere:	Ambient air

The friction behaviours of a-C coatings with EP/ZnS:Cu underlayer rubbed against stainless steel as well as on Si-wafer are illustrated in Fig. 3.18(a). The coating shows the initial coefficient of friction (COF) value at 0.2 and gradually increases to the higher value after a few metres of sliding distance, and finally reaches the steady state at value of 0.35. For a-C film deposited on Si-wafer, the coating presents the initial COF at 0.2 and keeps constant at this value for a few metres of the sliding distance. The COF then decreases to the lower value and keep stable at 0.13. However, after sliding for 25 m, the fluctuation of COF in the range of 0.1-0.15 occurs, which might have indicated the failure of the coating. Figure 3.18(b) shows the friction behaviours of the coatings rubbed against alumina balls. Both a-C films on EP/ZnS:Cu underlayer and on silicon wafer show the similar behaviour,

in which after the initial COF value of approximately 0.2, the friction coefficient drops to the lower value in a few sliding distance. At the steady-state, a-C film on EP/ZnS:Cu underlayer shows the COF at 0.15, while a-C film on silicon wafer shows slightly lower COF at 0.1.

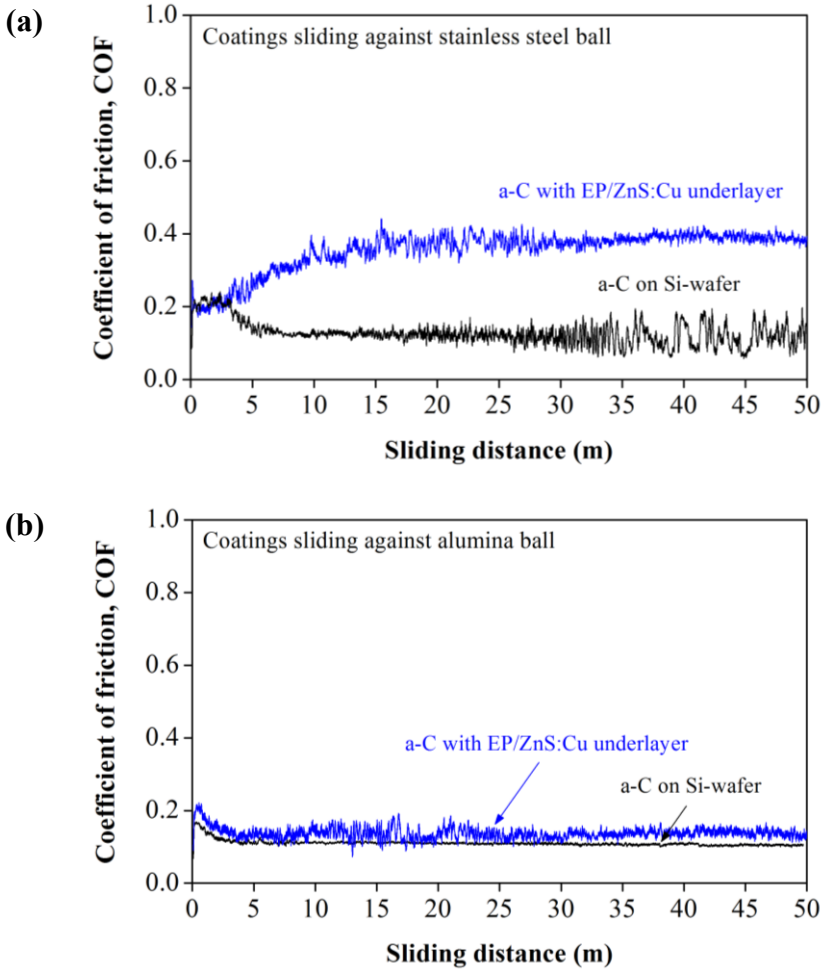

Fig. 3.18 Friction behaviours of a-C films with EP/ZnS:Cu underlayer and on Si-wafers deposited by pulsed VAD method at 6000 pulses of discharge sliding against (a) stainless steel and (b) alumina balls at normal load of 0.77 N

The optical microscopic observations of the wear tracks formed on a-C coatings with EP/ZnS:Cu underlayer sliding against stainless steel and alumina balls are shown in Fig. 3.29. In addition, the wear tracks formed on a-C films deposited on Si-wafers were also observed for comparison. It is found that the width of the wear tracks measured at the real contact points of a-C coatings on EP/ZnS:Cu underlayer are wider than those of the films on Si-wafers, suggesting that deformation of the EP/ZnS:Cu underlayer occurs during the test. For a-C coating with EP/ZnS:Cu underlayer, as shown in Fig. 3.19(a), it seems that the debris generated during the test still adheres in the form of layer on the wear track. This can be explained that the wear debris particles are generated from the real contact area at the top of the asperities on the surface roughness. These debris particles are accumulated at grooves of the crack network or between the large asperities, resulting in the layer formation as the test is prolonged [46]. The formation of this layer might also relate to the increasing of the COF to the higher value at the steady state of the friction test as shown in Fig. 3.18(a). In case of a-C film on EP/ZnS:Cu underlayer sliding against alumina ball, a low COF is obtained accompanying with partially removal of a-C film as can be observed in Fig. 3.19(b). It can be also observed that fracture and fragmentation of a-C film occurs due to the substrate deformation under the ball loading. Since alumina ball is twice time harder than stainless steel ball [47], the wear resistant of the coating become lower. As a result, the spallation or removal of the fragment happens, especially near the crack network.

For a-C film deposited on Si-wafer, the low COF value is obtained accompanying with the typical wear track. However, an unexpected damage occurs on the wear track for a-C film sliding against stainless steel ball, resulting in a local spalling of the coating as shown in Fig. 3.19(c). This caused the fluctuation of the COF as presented in Fig. 3.18(a). In case of a-C film sliding against alumina ball, the wear track is more clearly visible than

that observed from the film sliding against stainless steel ball due to the higher wear rate of the coating when sliding against harder material as shown in Fig. 3.19(d). The tribological characteristics of a-C films rubbed against stainless steel and alumina balls have been studied comparatively [48,49]. The results showed that the coating rubbed against stainless steel ball had higher coefficient of friction accompanying with the lower wear rate of a-C film than those of the coating rubbed against alumina ball, which were similar to the results obtained in the present study.

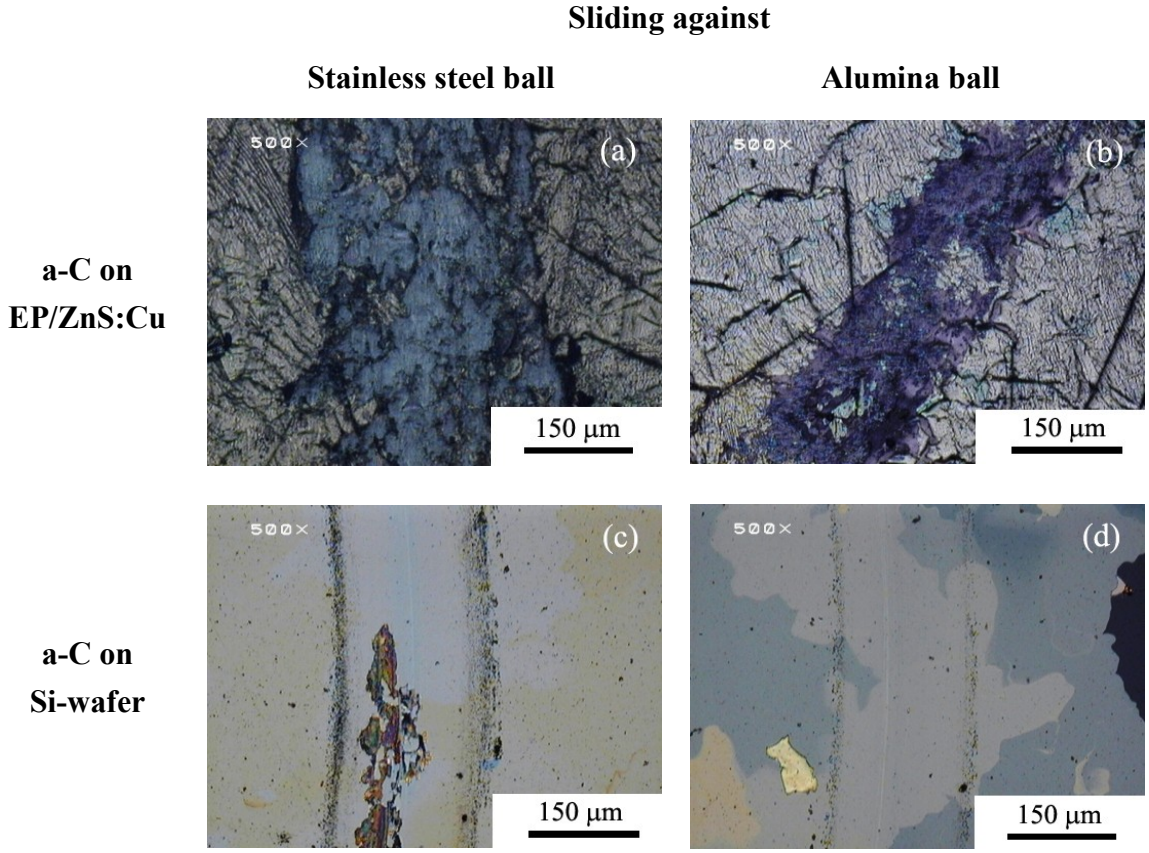

Fig. 3.19 Optical microscopic images of the wear tracks formed on the surfaces of a-C coatings with (a, b) EP/ZnS:Cu underlayer and (c, d) on Si-wafer deposited by pulsed VAD at 6000 pulses after sliding against stainless steel and alumina balls, respectively

After the friction test, the PL spectra were collected from the wear tracks of the coatings in order to confirm the sensing capability. Figure 3.20(a) shows the PL spectrum from the wear track of a-C coating with EP/ZnS:Cu underlayer rubbed against stainless steel ball. It shows a flat background without any distinct peak emission, as also evidenced by the fitted spectrum. This indicates the emission spectrum was undetected from the wear track. In contrast to the coating rubbed against alumina ball, the spectrum with a peak ranging between 500-600 nm can be detected as shown in Fig. 3.20(b). By the Gaussian curve fitting, the emission spectrum has the peak position at 528 nm, which is nearly similar to the emission spectrum from the as-prepared EP/ZnS:Cu layer.

The results on the luminescence spectra detected from the wear tracks of a-C coatings with EP/ZnS:Cu underlayer after the wear test show the consistencies with the optical microscopic images of the wear tracks in Fig. 3.19. The luminescence spectrum is undetected from the wear track of the coating after being rubbed against stainless steel ball. This corresponds to the result of the durability of the coating. On the other hand, the luminescence spectrum can be detected from the wear track of the coating after being rubbed against alumina ball. This is due to the removal of a-C film resulting in the exposure of EP/ZnS:Cu underlayer to the UV excitation and simultaneous emission of the luminescence to be detected.

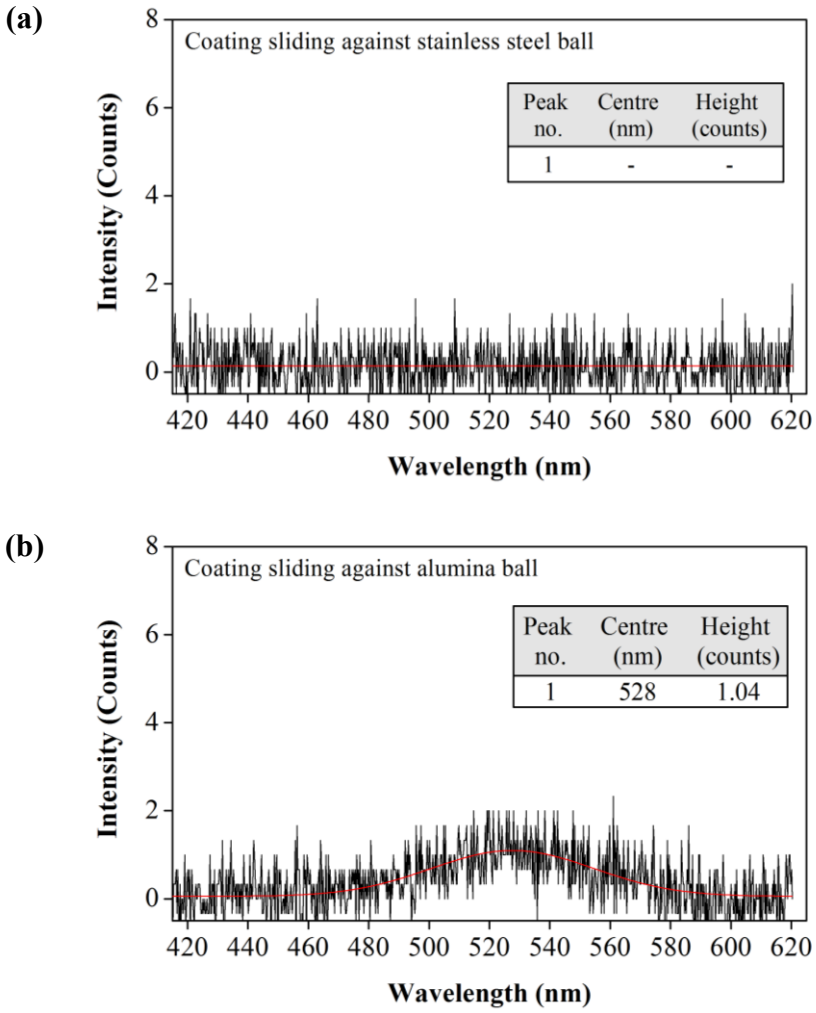

Fig. 3.20 Photoluminescence spectra detected from the wear tracks of a-C coatings with EP/ZnS:Cu underlayer deposited by pulsed VAD method at 6000 pulses of discharge after sliding against (a) stainless steel and (b) alumina balls

The obtained results have already shown that the wear monitoring of a-C films through luminescent spectroscopy was feasible. However, it is likely that the wear sensing capability was achieved only when the a-C film was mostly removed. This is similar to the demonstration carried out by Muratore et al. [50]. Another important issue for the concept of wear monitoring through this technique, as already mentioned in the first chapter of the

thesis, is that the sensing capability of the luminescent underlayer does not only depended on either the removal or the failure of the tribological coatings. It also depends on the degree of absorption of the excitation energy and emission energy through the tribological coating. This relates to the thickness of the tribological coating at which the luminescent underlayer can be excited and the luminescent emission can be detected.

The a-C films, especially non-hydrogenated type, typically have high internal stress that limits the thickness of the film to several hundred nanometres [51] and also affects the adhesion of the coating as similar to the result shown in Fig. 3.14 and 3.15. This limitation may cause the wear monitoring of a-C films to become more critical. In addition, according to the results from Raman spectroscopy of a-C films as shown in Fig. 3.16, the present of Raman signal of underlayer indicates the high transparency of a-C films to the laser excitation of Raman spectrometer (532 nm). This wavelength is close to the emission wavelength of the EP/ZnS:Cu underlayer (525 nm). This can be implied that it is possible to detect the luminescence from the coating even though the coating is not completely worn out.

Accordingly, the relationship between the luminescence intensity detected from a-C coatings with EP/ZnS:Cu underlayer and the thickness of a-C films has been studied. Figure 3.21(a) presents the PL spectra detected from several thicknesses of a-C films deposited on EP/ZnS:Cu underlayer. The thickness of a-C film was varied by changing the number of pulse discharge. It is also noted that spectra shown in the figure are plotted relatively to the intensity of the as-prepared EP/ZnS:Cu layer itself. The result shows that as the thickness of a-C films increases, PL intensity detected from EP/ZnS:Cu underlayer is reduced. After a-C films with the thickness of 240 nm has been deposited, the luminescence from the coating is undetected. The extracted peak intensities from each spectrum and the corresponding thicknesses of a-C film are then replotted in Fig. 3.21(b).

The data has also been exponentially fitted and has a well correlation with the Beer-Lambert law which shows the exponential decrease in the initial intensity of the beam as it pass through the coating at distance of traversing. As a result, this relationship enables the user to determine the remaining thickness of a-C film when it is worn out to a certain thickness.

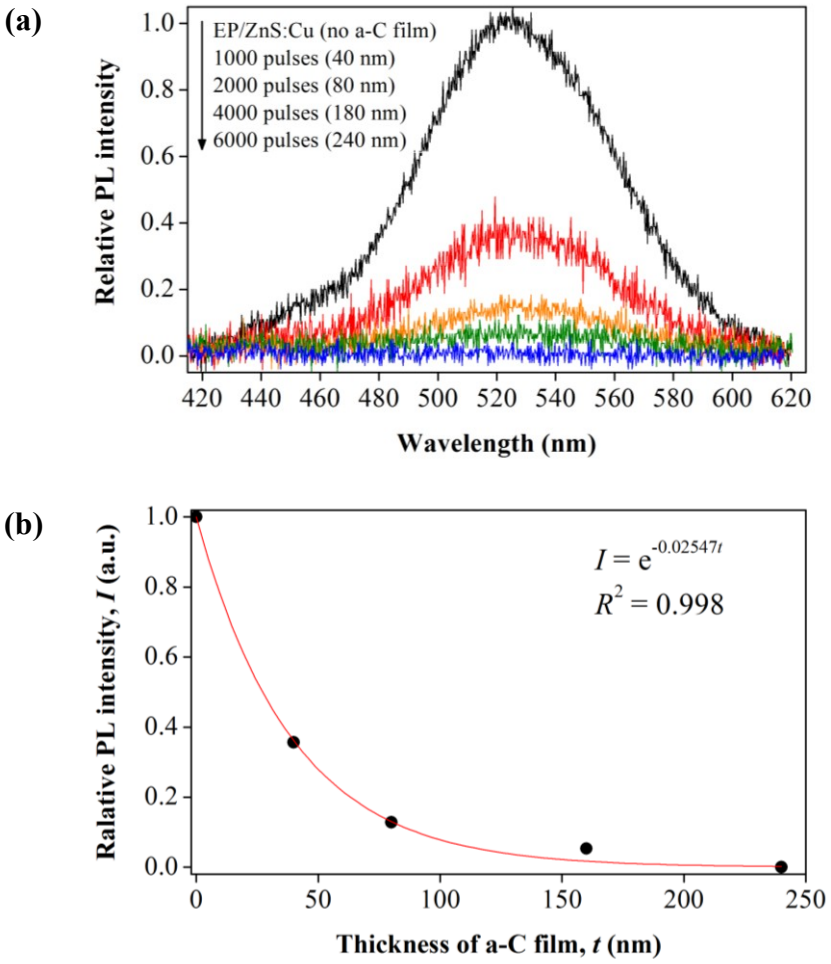

Fig. 3.21 (a) Photoluminescence (PL) spectra detected from the a-C coatings with EP/ZnS:Cu underlayer at various thicknesses of a-C film and (b) relationship between PL intensity at the peak centre of 525 nm as a function of a-C film thickness including the fitted equation and the coefficient of determination (R^2)

Although it has been shown that the luminescence could be detected from the wear track after the friction test of a-C coating with EP/ZnS:Cu underlayer sliding against alumina ball as shown in Fig. 3.20(b), several attempts to demonstrate the wear monitoring using the relationship between the PL intensity and the thickness of a-C film as shown in Fig. 3.21 have not been successful. A few limitations on the sensing capability of this coating system have been found;

(1) The wear mechanism of the coating; since the coating system consists of a hard a-C film deposited on the soft polymer epoxy resin and the thickness of the EP/ZnS:Cu underlayer (50 μm) is remarkably thicker than a-C layer (240 nm), the elastic property mismatch is drastically large, as summarised in Table 3.5. This can affect the tribological characteristic of the coating. Figure 3.22 shows the typical load-displacement curves of a-C films deposited on Si-wafer and on EP/ZnS:Cu layer as well as bare EP/ZnS:Cu layer under the indented load of 6 mN. Compared with a-C film deposited on Si-wafer, the a-C film deposited on EP/ZnS:Cu layer shows much higher maximum indentation depth accompanying with pop-in steps at the indentation depths of 100 and 250 nm. The presence of pop-in steps indicates that crack or fracture through the thickness of a-C film is generated because the indentation depth at which the pop-in steps has presented is equal to the coating thickness (240 nm) [52]. In addition, it is also apparent that the deformation behaviour of a-C film on EP/ZnS:Cu layer after the pop-in steps is similar to that of the bare EP/ZnS:Cu. This evidence strongly confirms that the mechanical characteristic of the underlayer substrate plays an important role in during the tribological test. Although the a-C film has been worn out exposing the EP/ZnS:Cu underlayer when it was rubbed against alumina ball, the wear track was still non uniform as already shown in Fig. 3.19(b). The removal of a-C film was in the form of fragment, which was resulted from the

deformation of the EP/ZnS:Cu under the ball loading. This might also cause the lack of the precise luminescence intensity.

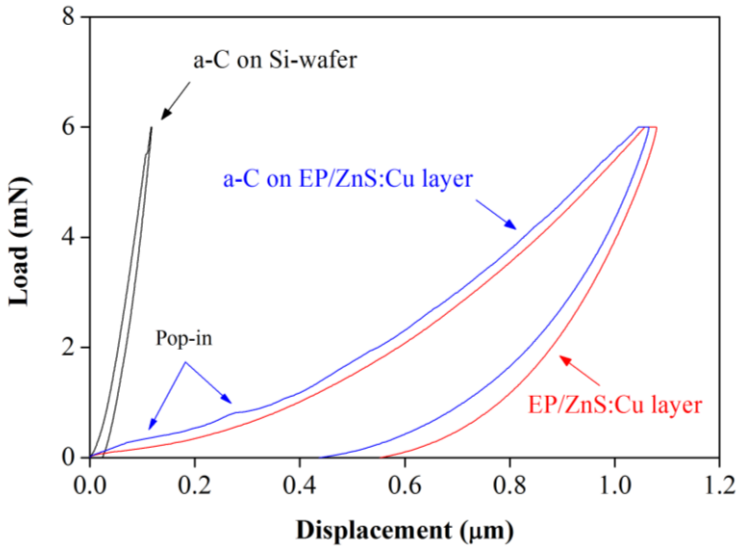

Fig. 3.22 Typical load-displacement curves of a-C films deposited on Si-wafer and EP/ZnS:Cu layer by pulsed VAD at 6000 pulses of discharge as well as the bare EP/ZnS:Cu layer analysed by nanoindentation at the indented load of 6 mN

(2) The surface roughness of the final coating; The average surface roughness (R_a) of a-C film deposited on EP/ZnS:Cu coating measured with a stylus profilometer is 262 nm as illustrated in Fig. 3.23, which is nearly equal to or over the thickness of a-C films (240 nm). As mentioned previously that the increase of the surface roughness is due to the crack network and the corrugated surface texture, it is difficult to investigate the wear depth precisely by using a relationship between the luminescent intensity and a-C film thickness, especially if the wear track is shallow. Therefore, the coating with a smooth surface is necessary for the investigation.

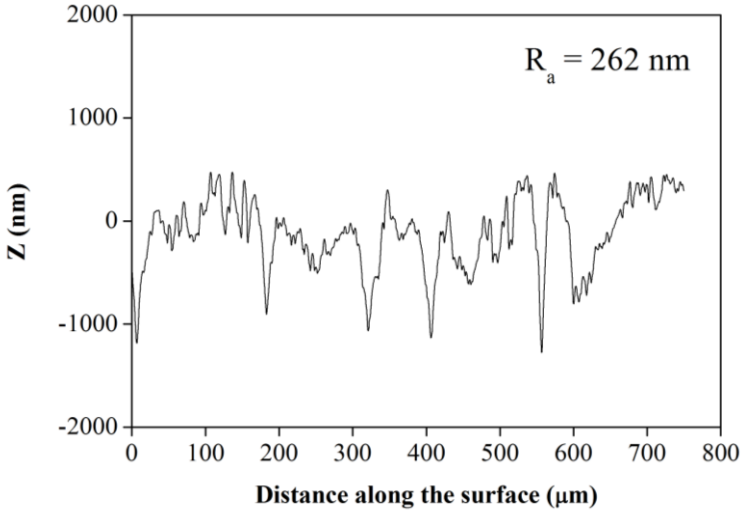

Fig. 3.23 Surface profilometer scanning along the surface of as-fabricated a-C coating with EP/ZnS:Cu underlayer

3.4 Conclusion

The coating system consisted of a-C film deposited onto epoxy resin containing luminescent ZnS:Cu powder (a-C coating with EP/ZnS:Cu underlayer) were fabricated. EP/ZnS:Cu layer were initially fabricated by a simple coating technique, in which the mixture of epoxy resin and ZnS:Cu powder was dropped onto Si-wafer substrate and it was covered by polystyrene film allowing the mixture spread over the substrate naturally.

Amorphous carbon (a-C) films were deposited onto the fresh surface of the cured EP/ZnS:Cu layers by two methods, i.e., sublimation of fullerenes powder (C_{60}) in electron beam excited plasma (EBEP) method at two substrate bias voltages (-200 and 0 V) and pulsed vacuum arc deposition (VAD) method at the number of discharge 6000 pulses. It was found that the a-C coatings deposited by sublimation of C_{60} in EBEP method at both bias voltages had polymer-like structure and physically degraded due to interaction with the plasma during deposition. In contrast, a-C coating deposited by pulsed VAD showed

the similar structure of typical hard a-C film. The luminescence from the EP/ZnS:Cu underlayer was unable to be detected after being coated with a-C film with all methods.

The performances of the a-C coatings with EP/ZnS:Cu underlayer coatings including tribological properties and wear sensing capability were demonstrated by a ball-on-disk friction test and subsequently photoluminescence measurement from the wear track. It was found that the a-C coatings deposited by sublimation of C_{60} EBEP methods showed the high coefficient of friction (COF) at 0.7 in almost entire the test. This was due to the structural change as well as the formation of the defects on the coating surface, resulting in the coatings which become soft and easily worn out during the friction test. However, the luminescence could be detected from the wear tracks, indicating the complete removal of a-C films. In contrast to a-C coating obtained from pulsed VAD method, the coating showed a high durability with COF of 0.35 when it was rubbed against stainless steel ball at the normal force of 0.77 N for 50 m. This result consequently led to the undetected luminescence from the wear track after the friction test. In contrast, the coating rubbed against alumina ball showed the lower COF at 0.15 and also the evidence of removal of a-C films, resulting in the luminescence which could be detected from the wear track. Moreover, the remaining thickness of a-C films can possibly be monitored when the a-C films are worn out to a certain thickness. However, wear monitoring of the coating system was found to be difficult to demonstrate due to the high surface roughness of the as-fabricated coating and non uniform wear track. Therefore, a rigid coating with smooth surface is necessary for further demonstration.

3.5 References

[1] M.A. Boyle, C.J. Martin and J.D. Neuner : *Epoxy resins*, ASM Handbook: Composites Vol. 21, ASM International, (2001) 78.

[2] J. Lim, S. Jun, E. Jang, H. Baik, H. Kim and J. Cho : Adv. Mater., **19** (2007) 1927.

[3] Y. Yang, Y.Q. Li, S.Y. Fu and H.M. Xiao : J. Phys. Chem. C, **112** (2008) 10553.

[4] M. Nyman, L.E. Shea-Rohwer, J.E. Martin and P. Provencio : Chem. Mater., **21** (2009) 1536.

[5] X.S. Xing and R.K.Y. Li : Wear, **256** (2004) 21.

[6] C. Qi, H. Gao, F. Yan, W. Liu, G. Bao, X. Sun, J. Chen and X. Zheng : J. Appl. Polym. Sci., **97** (2005) 38.

[7] V. Siddhartha, A. Patnaik and A.D. Bhatt : Mater. Des., **32** (2011) 615.

[8] N. Nakayama, R. Tominaga, M. Mayuzumi, K. Hanada, T. Sano and H. Takeishi : Surf. Eng., **19** (2003) 437.

[9] T. Ohana, T. Nakamura and A. Tanaka : Diam. Relat. Mater., **19** (2010) 894.

[10] Y.T. Pei, X.L. Bui, X.B. Zhou and J.Th.M. De Hosson : Surf. Coat. Tech., **202** (2008) 1869.

[11] S. Podgoric, B.J. Jones, R. Bulpett, G. Troisi and J. Franks : Wear **267** (2009) 996.

[12] Y. Ohgoe, K.K. Hirakuri, K. Tsuchimoto, G. Friedbacher and O. Miyashita : Surf. Coat. Tech., **184** (2004) 263.

[13] D. Martinez-Martinez, M. Schenkel, Y.T. Pei, J.C. Sanchez-Lopez and J.Th.M. De Hosson : Surf. Coat. Tech., **205** (2011) S75.

[14] K. Baba and R. Hatada : *Proceedings of the 9th International Conference on Modification of Materials with Particle Beams and Plasma Flow*, (2008) 407.

[15] I. Ahmad, S.S. Roy, Md.A. Rahman, T.I.T. Okpalugo, P.D. Maguire and J.A. McLaughlin : Curr. Appl. Phys., **9** (2009) 937.

[16] B.J. Jones and J.J. Ojeda : Surf. Interface Anal., **44** (2012) 1187.

[17] Y. Luo, D. Zhang and H. Chen : Adv. Mater. Res., **189** (2011) 9.

[18] H. Vaez-Taghavi and A. Hirata : Mater. Lett., **64** (2010) 83.

[19] H. Vaez-Taghavi and A. Hirata : Diam. Relat. Mater., **20** (2011) 1036.

[20] S.Y. Chun, A. Chayahara, A. Kinomura, N. Tsubouchi, C. Heck, Y. Horino and H. Fukui : Jpn. J. Appl. Phys., **38** (1999) L467.

[21] M. Horikoshi and A. Hirata : New Diam. Front. C. Tec., **16** (2006) 267.

[22] K.E. Chike, M.L. Myrick, R.E. Lyon and S.M. Angel : Appl. Spectrosc., **47** (1993) 1631.

[23] J.K.F. Tait, H.G.M. Edwards, D.W. Farwell and J. Yarwood : Spectrochim. Acta, Part A, **51** (1995) 2101.

[24] R. Hardis, J.L.P. Jessop, F.E. Peters and M.R. Kessler : Composites Part A, **49** (2013) 100.

[25] L. Qi, B.I. Lee, J.M. Kim, J.E. Jang and J.Y. Choe : J. Lumin., **104** (2003) 261.

[26] W.M. Yen, S. Shionoya and H. Yamamoto : *Phosphor handbook*, CRC Press, Boca Raton, (2006) 247.

[27] T.T. Nguyen, X.A. Trinh, L.H. Nguyen and T.H. Pham : Adv. Nat. Sci.: Nanosci. Nanotechnol., **2** (2011) 035008.

[28] R.G. Lacerda, P. Hammer, C.M. Lepienski, F. Alvarez and F.C. Marques : J. Vac. Sci. Technol. A, **19** (2001) 971.

[29] P.K. Chu and L. Li : Mater. Chem. Phys., **96** (2006) 253.

[30] H. Huck, E.B. Halac, M. Reinoso, A.G. Dall-Asen, A. Somoza, W. Deng, R.S. Brusa, G.P. Karwasz and A. Zecca : Appl. Surf. Sci., **211** (2003) 379.

[31] P. Zhou, K.A. Wang, Y. Wang, P.C. Eklund, M.S. Dresselhaus, G. Dresselhaus and R.A. Jishi : Phys. Rev. B, **46** (1992) 2595.

[32] A.G. Dall-Asen, M. Verdier, H. Huck, E.B. Halac and M. Reinoso : Appl. Surf. Sci., **252** (2006) 8005.

[33] M. Yoshikawa, G. Katagiri, H. Ishida, A. Ishitani and T. Akamatsu : J. Appl. Phys., **64** (1988) 6464.

[34] G. Adamopoulos, J. Robertson, N.A. Morrison and C. Godet : J. Appl. Phys., **96** (2004) 6348.

[35] C. Casiraghi, F. Piazza, A.C. Ferrari, D. Grambole and J. Robertson : Diam. Relat. Mater., **14** (2005) 1098.

[36] N. Matuda, S. Baba and A. Kinbara : Thin Solid Films, **81** (1981) 301.

[37] H.Y. Yu, C. Kim and S.C. Sanday : Thin Solid Films, **196** (1991) 229.

[38] M.C. Polo, J.L. Andujar, A. Hart, J. Robertson and W.I. Milne : Diam. Relat. Mater., **9** (2000) 663.

[39] S.J. Kim, J.I. Yoon, M.W. Moon and K.R. Lee : Diam. Relat. Mater., **23** (2012) 61.

[40] H. Takikawa, N. Miyakawa, S. Minamisawa and T. Sakakibara : Thin Solid Films, **457** (2004) 143.

[41] G.A. Abbas, S.S. Roy, P. Papakonstantinou and J.A. McLaughlin : Carbon, **43** (2005) 303.

[42] S. Xu, D. Flynn, B.K. Tay, S. Prawer, K.W. Nugent, S.R.P. Silva, Y. Lifshitz and W.I. Milne : Philos. Mag. B, **76** (1997) 351.

[43] M.C. Polo, J.L. Andujar, A. Hart, J. Robertson and W.I. Milne : Diam. Relat. Mater., **9** (2000) 663.

[44] T.A. Friedmann, K.F. McCarty, J.C. Barbour, M.P. Siegal and D.C. Dibble : Appl. Phys. Lett., **68** (1996) 1643.

[45] J. Robertson : Mater. Sci. Eng. R, **37** (2002) 129.

[46] J. Jiang, R.D. Arnell and J. Tong : Wear **211** (1997) 254.

[47] H. Liu, A. Tanaka and T. Kumagai : Thin Solid Films, **352** (1999) 145.

[48] H. Ronkainen, J. Likonen and J. Koskinen : Surf. Coat. Tech., **55** (1992) 570.

[49] B.K. Tay, D. Sheeja, Y.S. Choong, S.P. Lau and X. Shi : Diam. Relat. Mater., **9** (2000) 819.

[50] C. Muratore, D.R. Clarke, J.G. Jones and A.A. Voevodin : Wear, **265** (2008) 913.

[51] D. Sheeja, B.K. Tay, K.W. Leong and C.H. Lee : Diam. Relat. Mater., **11** (2002) 1643.

[52] X. Li, D. Diao and B. Bhushan : Acta Mater., **45** (1997) 4453.

CHAPTER 4

AMORPHOUS CARBON COATINGS WITH SILICA UNDERLAYER CONTAINING CdSe/ZnS QUANTUM DOTS

4. Amorphous carbon coatings with silica underlayer containing CdSe/ZnS quantum dots

4.1 Introduction

According to the experimental results obtained in Chapter 3, the demonstration of wear monitoring of a-C film was still remained because it was found that a-C films showed the remarkably rough surface. Moreover, the wear characteristic of a-C film was found to be non-uniform when the underlayer was a soft polymer-based substrate. As a result, the determination of remaining thickness became difficult. Therefore, the coatings with more rigidity and smooth surface should be further improved.

Instead of polymeric epoxy resin, silica coating offers several attractive properties, such as mechanical hardness, chemical inertness and electrical insulation. These have led to a variety of applications, such as electric insulating coatings, protective barriers against oxidation, corrosion, and scratching for metallic materials, coatings on glass for preventing alkali-dissolution [1]. In optoelectronic applications, silica is an effective matrix for encapsulating nano-size materials since it has proved to show good mechanical and optical properties and provide a high stability with nanometre-size semiconductor crystallites [2-4].

Regarding the use of luminescent particle with a size in several micrometers as an embedded material, it limited the thickness of the coating to at least equal to the size of the particle (several ten micrometers) as well as the homogeneity of the particle dispersion in the matrix. To overcome this limitation, the tiny nanocrystalline particles or quantum dots (QD) has been an effective candidate. Due to their special optical properties compared to those in their bulk state, they have been used in a broad range of applications including photovoltaics, solid-state lighting, and fluorescent imaging [5,6]. Among the QDs,

CdSe/ZnS QD has gained more interest because not only the tunable emission spectrum in the visible range by controlling the size of CdSe core, the luminescence efficiency or quantum yield can be more enhanced by passivation of CdSe core with ZnS shell [7,8].

Since the CdSe/ZnS QD structure is core/shell, it is difficult to fabricate silica coating containing the QD with such structure by conventional PVD or CVD methods. Typically, the method to fabricate luminescent QD dispersive silica coatings is by a sol-gel method [9,10]. However, the obtained coating has low density with porous structure, which might be improper for tribological applications. Another type of silica precursor for fabricating a dense silica coating is a class of the organo-silicon precursor known as polysilazane (abbreviated as PSZ) [11]. Polysilazane is inorganic polymer composed of Si–N bonds with Si–H terminal groups, which can be converted to a dense silica film when it reacts with water or moisture [12-14]. Due to its impressive mechanical properties and chemical stability, silica coating derived from PSZ is applied for protecting steel from corrosion and abrasive wear at high temperatures [15].

In this chapter, the silica coating containing luminescent CdSe/ZnS QD prepared from liquid PSZ and CdSe/ZnS QD is fabricated to be used as a wear-sensing underlayer. The mixture of PSZ and CdSe/ZnS QD is spin coated on the substrates and subsequently cured at the low temperature in high humidity atmosphere. After curing, the silica/QD coatings are obtained and eventually coated with a-C films by R.F. magnetron sputtering method. The physical, luminescent and tribological properties are characterised as well as the wear monitoring of the a-C film is demonstrated.

4.2 Experimental

4.2.1 Fabrication of silica coatings containing CdSe/ZnS quantum dots (silica/QD)

The commercial luminescent CdSe/ZnS core/shell quantum dots (abbreviated as QD) with the emission wavelength at 530±5 nm were dissolved in toluene at the concentration of 5 mg/ml by sonicating in an ultrasonic bath for 10 min. The dissolved quantum dots were then mixed with liquid polysilazane (PSZ) with a magnetic stirrer at room temperature with a stirring speed of 500 rpm for 30 min. The concentration ratio of the dissolved quantum dots to PSZ was kept at 2.5 vol.%. To fabricate a coating, a drop of PSZ solution containing QD with an amount of 50 μl was dropped onto silicon wafer (12 mm×12 mm) and then was spin coated at 1000 rpm for 10 sec. The spin coated samples were finally cured at 50°C for 3 hr with relative humidity higher than 80%. In this stage the conversion of PSZ to silica network was occurred.

4.2.2 Deposition of amorphous carbon (a-C) films

Amorphous carbon (a-C) films were subsequently deposited onto the cured PSZ/QD or silica/QD layers by R.F. magnetron sputtering system. The deposition conditions were similar to the conditions used for deposition of a-C films on ZnS:Mn layer as given in Chapter 2. The result also showed that the adhesion between a-C films and luminescent layer was insufficient. Hence, a thin silicon intermediate layer (Si-interlayer) was added between a-C layer and luminescent layer for the adhesion improvement. The deposition process was carried out in sequential starting from evacuating the deposition chamber after the substrates had been set, substrate surface treatment by argon plasma, deposition of Si-intermediate layer and finally deposition of a-C films. The detail of deposition process and conditions is listed in Table 4.1. It is also noted here that the

preliminary study on deposition of amorphous carbon (a-C) films onto silica/QD layer by sublimation of C_{60} in electron beam excited plasma (EBEP) and pulsed vacuum arc deposition (VAD) were also carried out by using the process conditions as similar to the previous chapter. However, it was unsuccessful to obtain the a-C film with a clear surface appearance. The results will be shown and discussed in the next section.

Table 4.1 Process parameters and conditions for deposition of a-C coatings on luminescent silica/QD layer

Process	**Parameter**	**Corresponding value**
Chamber condition	Target	Graphite
	Plasma gas	Argon (99.995% purity)
	Base pressure (Pa)	Less than 1.5×10^{-3}
Plasma surface treatment of substrate	R.F. power (W)	100
	Pressure (Pa)	1
	Time (min)	10
Deposition of Si-intermediate layer	R.F. power (W)	50
	Pressure (Pa)	1
	Electrodes distance (mm)	50
	Time (min)	3
	Thickness (nm)	24
Deposition of a-C films	R.F. power (W)	100
	Pressure (Pa)	1
	Time (min)	30, 60, 120 and 240
	Electrodes distance (mm)	50
	Substrate temperature (°C)	Room temperature
	Deposition rate (nm/min)	1.4

4.2.3 Coating characterisations

For the silica/QD layer, the thickness was measured with a scanning electron microscope (SEM) at the fractured surface. Surface morphology of the coating was investigated with an optical microscope and an atomic force microscope (AFM). The structure of the coating was analysed by a Fourier transform infrared spectroscopy (FT-IR). The luminescent property was confirmed by irradiating with a UV light at 365 nm and the emitted photoluminescence (PL) spectrum was collected with a spectrometer. Furthermore, it was also found that the luminescence could be detected from the coating via Raman spectroscopy, which will be discussed later in the next section.

For the a-C film coated on silica/QD layer (a-C/silica/QD coating), Raman spectroscopy was used to determine the structure of a-C films. The surface morphology of the coating was also investigated with the optical microscope and AFM. The luminescence characteristic of the coating was analysed by Raman spectroscopy. For wear monitoring demonstration, the luminescence signal detected from the wear track after the friction test was examined and was used to determine the remained coating thickness. The laser beam with the output power of 10 mW was focused to the sample with an objective lens. The spot size of the laser on the sample surface was 1 μm. The Raman signals were measured over the range from 170-1900 cm^{-1} with a spot mode. The spectra were recorded for 3 times in every 5 s. For the friction test, a-C/silica/QD coatings were rubbed against stainless steel ball (SUS 440C with 4.8 mm in diameter) with a normal load of 0.3 N using a laboratory built ball-on-disk friction tester. The test was carried out in ambient atmosphere with a sliding speed of 13 mm/s. The wear track diameter was 5 mm. An atomic force microscope (AFM) was used to examine the wear profile formed on the coatings after friction test.

4.3 Results and discussion

4.3.1 As-fabricated silica/QD layers

The as-fabricated silica coatings containing luminescent CdSe/ZnS quantum dots (silica/QD) prepared by spin coating of the mixture of liquid polysilazane and CdSe/ZnS quantum dots show the improved hardness as simply scratched by a steel pin comparing with the epoxy resin coating already presented in the previous chapter. The thickness of silica/QD coating measured by SEM at the cross section is 1 μm as shown in Fig. 4.1. The dispersion of the luminescent quantum dots could not be observed due to the size of quantum dot being typically less than 10 nm [16-18], which is over the operating range of the SEM. Furthermore, it can be seen from the cross-section that the fractured edges extend across the interface into the coating without traces of delamination at the coating-substrate interface, indicating good adhesion of the coating to the substrate.

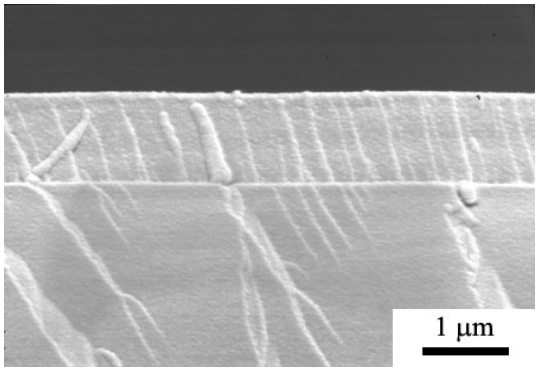

Fig. 4.1 SEM image of cross-section of silica/QD coating

The structure of as-fabricated silica/QD coatings was analysed by FT-IR in order to reveal the chemical composition. Figure 4.2 shows the infrared absorption spectra of silica/QD coatings before and after curing. Before curing, the main observable peaks are at

831 and 931 cm^{-1} corresponding to the vibration of Si-N groups, whereas the peaks at 1182 and 3371 cm^{-1} based on the N-H group. In addition, a strong peak at 2166 cm^{-1} can be assigned to the vibration from Si-H groups [19]. These are mainly the basement compositions of polysilazane. After hydrolysis with moisture or water, silanol groups are formed as short living intermediates. Finally, condensation and cross-linking reactions result in the formation of silica as can be displayed by the following reaction [12,13];

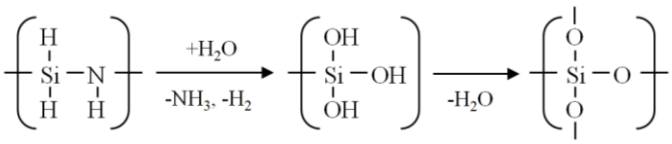

Therefore, the strong peaks at 450 and 1076 cm^{-1} corresponding to the Si-O groups [13,14,20] are observed after curing, while other peaks found in the state before curing significantly decrease. This has confirmed that the conversion of polysilazane to silica network is occurred during the curing step.

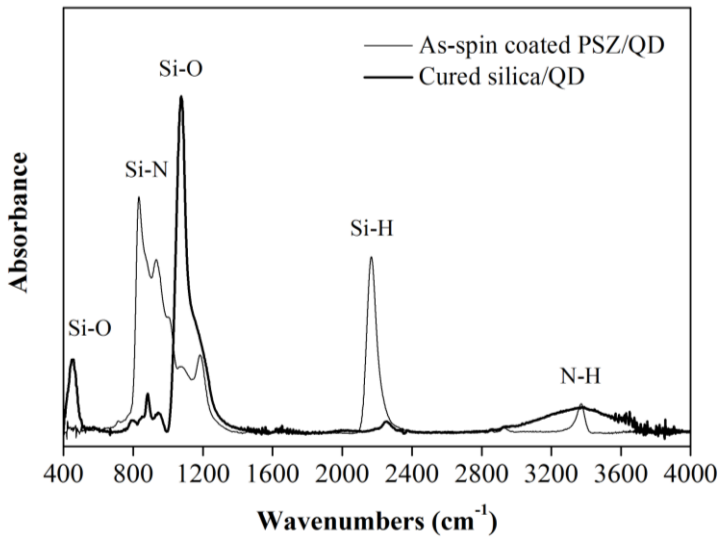

Fig. 4.2 FT-IR spectra showing the molecular conversion from PSZ/QD to silica/QD coating after curing at 50°C for 3 hr in relative humidity higher than 80%

The surface morphology of the as-fabricated silica/QD observed with an optical microscope is shown in Fig. 4.3(a). Some amount of micron-size droplets are observed on the surface, which are believed to be the silica that preliminary precipitated when the PSZ exposed with the moisture in the atmosphere since the polysilazne is highly reactive with the hydroxyl group (moisture or water) due to it contains huge amount of Si-H groups. These droplets are also found on the neat silica coating and after the spin coating process. However, the major area of the surface shows smooth surface in the macroscopic scale. In microscopic scale, the surface morphology was examined by AFM as shown in Fig. 4.3(b). The random asperities with the height less than 20 nm can be observed on the surface of the coating. These asperities are different from the droplets formed as described previously because the size is smaller. It is probably that these asperities are caused by the embedded CdSe/ZnS quantum dots in the silica coating matrix. Accordingly, the additional AFM analysis was carried out on the surface of the neat silica coating prepared by the same method as shown in Fig. 4.3(c). Note that the vertical scale of the image is different. As can be seen from the image, there is no asperity formed on the surface of the coating. This could be reasonably concluded that the asperities formed on the silica/QD surface were caused by the embedded luminescent CdSe/ZnS QD. Furthermore, the average surface roughness (R_a) of the silica/QD coating as measured from the area presented in the figure was 1.07 nm, which is remarkably smoother than the ZnS:Mn and EP/ZnS:Cu coatings as already presented formerly.

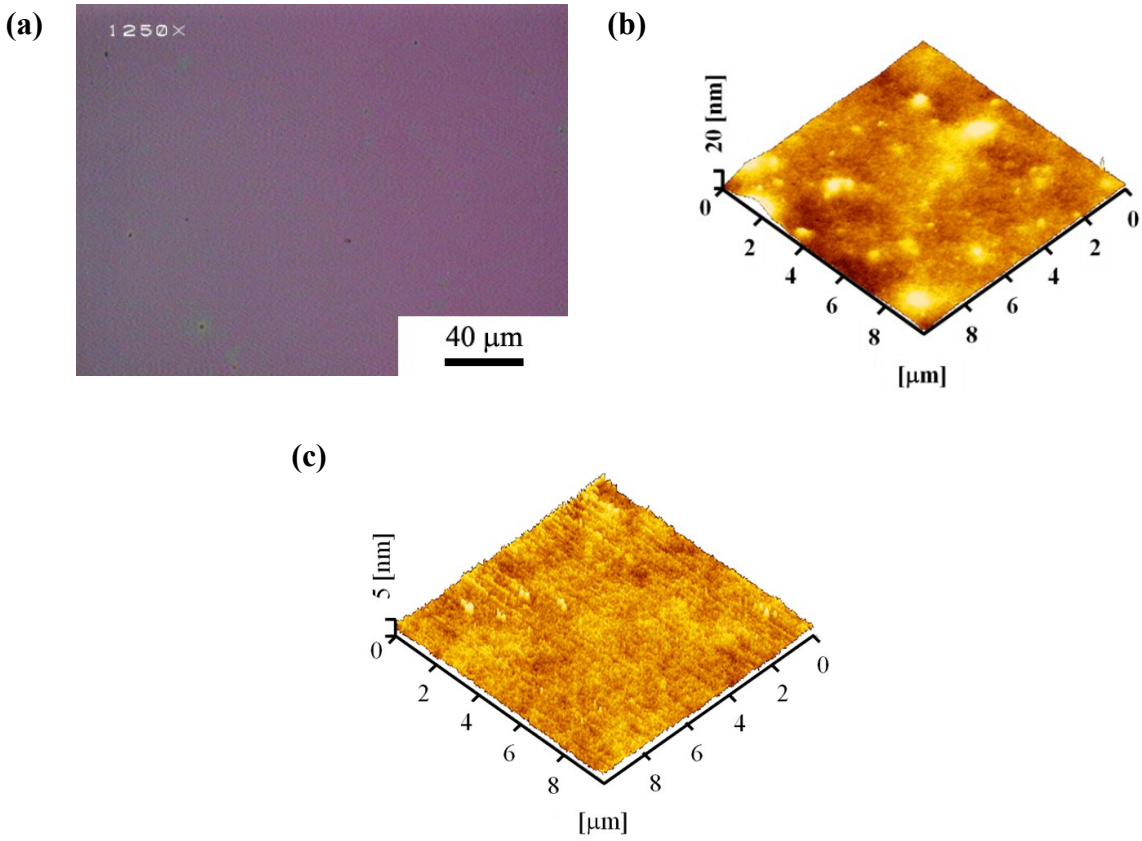

Fig. 4.3 (a) Optical microscopic and (b) AFM image of as-fabricated silica/QD layer and (c) AFM image of neat silica coating

Regarding the structural analysis by FT-IR as shown in Fig. 4.3, the information of the chemical composition of the silica coating could only be obtained without any information of the luminescent quantum dots (QD) that embedded in the silica matrix. The existence of the luminescent QD in the silica coating can be investigated by luminescence spectroscopy as shown in Fig. 4.4(a). The silica/QD was irradiated with a UV light at the excitation wavelength 365 nm. The coating exhibits a green luminescence at the peak centre of 535 nm, which is in agreement the emission spectrum claimed by the QD provider. This indicates that the luminescent QD are incorporated in the silica matrix coating.

In CdSe/ZnS core/shell QD, the energy band gap of the ZnS shell (~3.6-3.8 eV) is wider than the band gap of CdSe core material. The electron and hole are confined within the CdSe core because both conduction and valence band edges of CdSe core are located within the energy gap of ZnS shell [21,22]. As a result, the emission energy is determined by energy gap of the CdSe core, which is size-dependent [23]. Figure 4.4(b) illustrates the excitation and relaxation transitions of electron-hole pair in the CdSe/ZnS QD. Following photoexcitation by a UV light at 365 nm (3.4 eV) of the QD to the high energy state in the conduction band (CB) of the CdSe core, the non-radiative relaxation of the charge carriers to the band edge and finally radiative recombination from the lowest states of the band edge is processed.

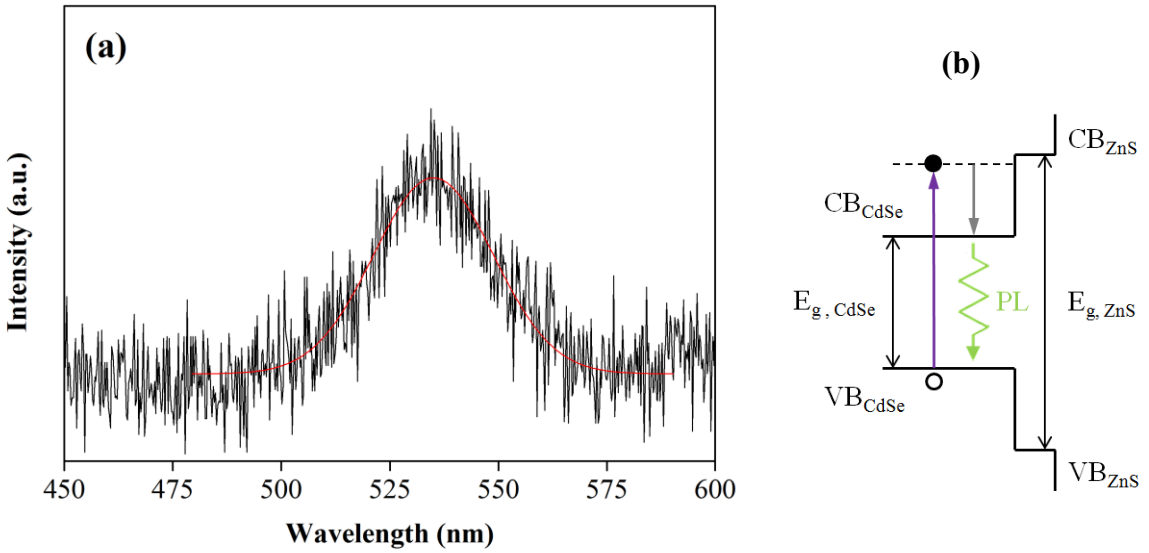

Fig. 4.4 (a) Photoluminescence (PL) investigation of as-fabricated silica/QD coating under irradiating with a UV light at 365 nm and (b) schematic band diagram showing the excitation and relaxation transitions of electron-hole in CdSe/ZnS quantum dots [21,22]

It has also been found that the incorporation of the QD in the silica matrix could be proved using Raman spectroscopy technique. Raman spectrum of the as-fabricated silica/QD coating is shown in Fig. 4.5(a). The spectrum exhibits a strong luminescence background with the maximum value located at 323.5 cm^{-1}. In addition, a small peak at 520 cm^{-1} is also appeared on the spectrum. Further Raman spectroscopic analyses on the CdSe/ZnS QD particles as well as neat silica coating prepared by the same method were also carried out in order to investigate the origin of the Raman peaks of the silica/QD coating. Figure 4.5(b) shows the Raman spectrum of the CdSe/ZnS QD particles. The spectrum exhibits strong luminescence background similar to the obtained spectrum from silica/QD in Fig. 4.5(a). Because of the high PL quantum efficiency of QD, the Raman spectra are usually superimposed on a broad luminescence background [24]. However, the shape or characteristics of spectra depends on the wavelength of excitation source [25]. For the neat silica coating, the characteristic peaks that correspond to the coating are not clearly observed except for the three dominant peaks located at 308, 520 and 950-1000 cm^{-1} as shown in Fig. 4.5(c). These peaks could be characterised to originate from Si substrate [26] due to the high transparency of the silica coating to the wavelength of laser probe. Therefore, the luminescence background and a small peak at 520 cm^{-1} obtained on the Raman spectrum of silica/QD coating are the results from the CdSe/ZnS QD embedded in the coating and Si-wafer, respectively.

The results on Raman spectroscopy of silica/QD layer suggested that the luminescence from the silica/QD layer can be detected using Raman spectrometer. Due to a fact of the higher sensitivity with lower noise level of the measuring system for Raman spectrometer compared with the spectrometer used in case of UV excitation, the luminescence investigation of the coating system was carried out with Raman spectrometer throughout this Chapter.

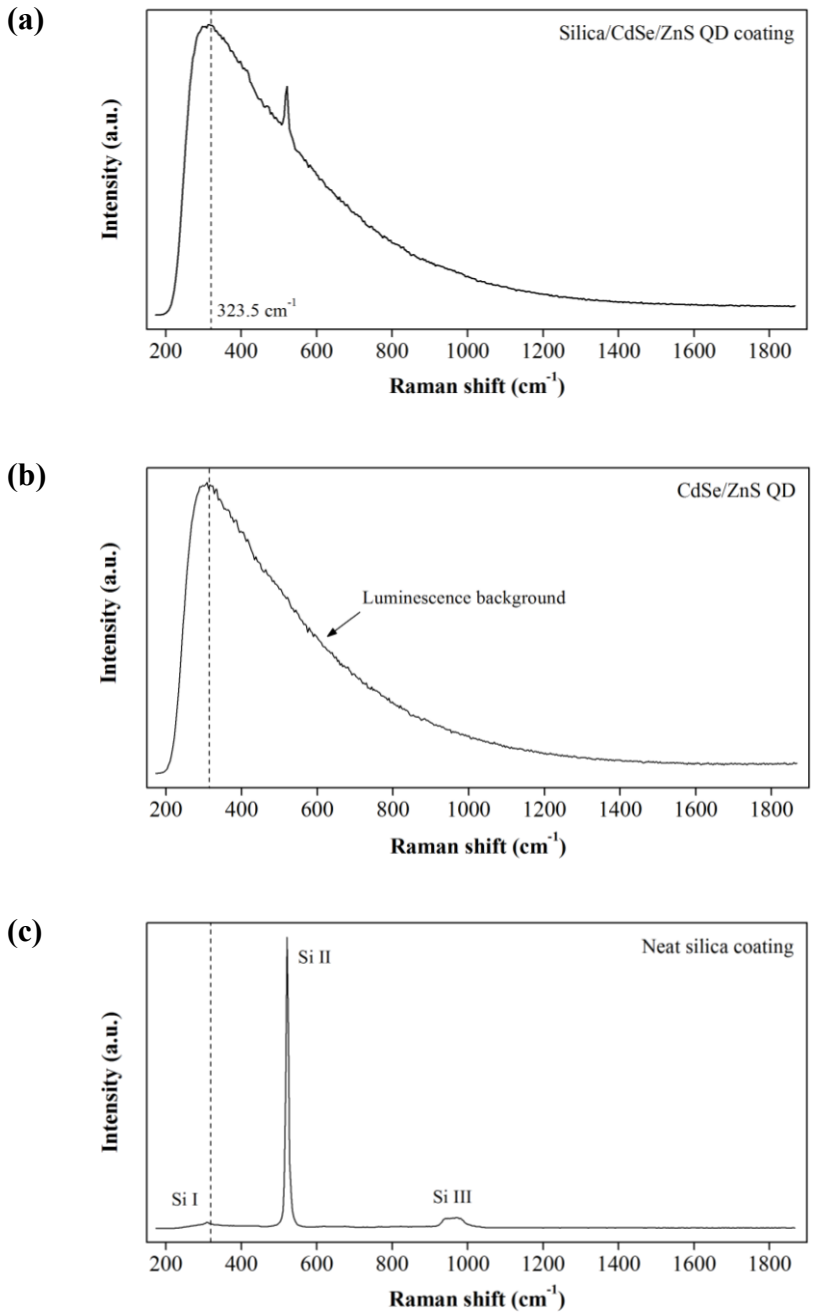

Fig. 4.5 Raman spectra measured from (a) silica/QD coating, (b) Neat CdSe/ZnS QD and (d) neat silica coating under the laser excitation at 532 nm

4.3.2 Deposition of a-C films on silica/QD layers by R.F. magnetron sputtering method

As mentioned in the experimental section, the preliminary experiments on deposition of a-C films onto silica/QD layers by other methods have been carried out prior to deposition of a-C film onto the luminescent silica/QD layer by R.F. magnetron sputtering method. The deposition of a-C films by sublimation of C_{60} in EBEP excited plasma at the substrate bias voltage -200 V and pulsed vacuum arc deposition (VAD) at 6000 pulses of discharge similarly to the previous Chapter have been tried. The surface appearances of the coatings obtained from both methods are illustrated in Fig. 4.6. The cratering defects were observed throughout the surface of a-C/silica/QD coating prepared by sublimation of C_{60} in EBEP method as shown in Fig. 4.6(a). By applying DC negative bias voltage to the silica/QD coating substrate, which is insulator, the charge accumulation on the film surface is large as to cause dielectric breakdown. As a result, discharge spark is occasionally observed on the substrate surface during deposition, leading to the cratering defects formed on the coating surface [27]. For the a-C/silica/QD coating prepared by pulsed VAD method, wrinkle, crack and local spallation of a-C film are observed on the surface of the coating immediately after the samples were taking out from the coating chamber. Although a thin tungsten intermediate layer was deposited onto the silica/QD layer prior to a-C deposition for the adhesion improving purpose, the wrinkles are still formed on the surface as shown in Fig. 4.6(b). Since the a-C film deposited by pulsed VAD method is typically contains high compressive stress [28], the formation of wrinkles, cracks and spallation of a-C film suggested the adhesion of a-C layer to the substrate was still insufficient.

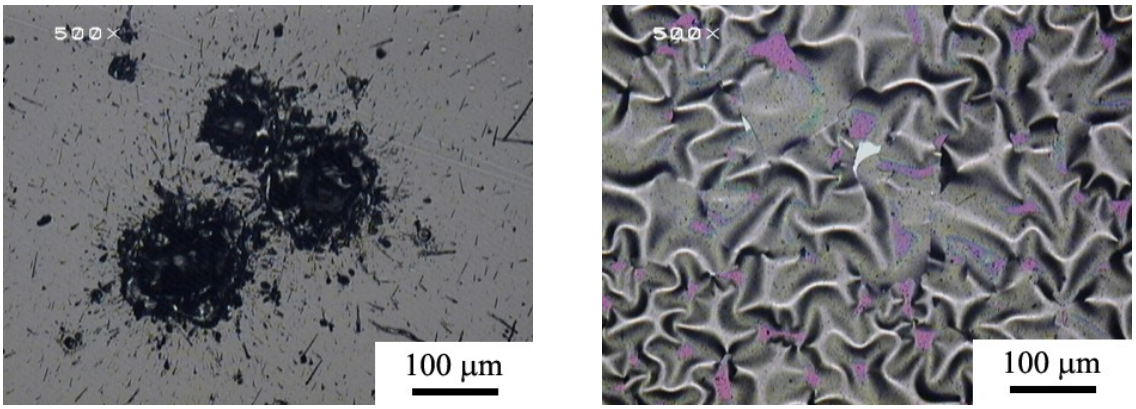

(a) Sublimation of C_{60} in EBEP **(b)** Pulsed VAD

Fig. 4.6 Surface appearances observed with optical microscope of a-C/silica/QD coatings prepared by (a) sublimation of C_{60} in EBEP method at the substrate bias voltage of -200 V and (b) pulsed VAD method at 6000 pulses of discharge with 20-nm-tungsten intermediate layer

In case of a-C/silica/QD prepared by R.F. magnetron sputtering, the coating shows the clear surface without any crack, wrinkle or spallation of a-C layer as shown in Fig. 4.7(a). Accordingly, R.F. sputtering method was used in further study to fabricate the a-C films with silica/QD underlayer. The deposition was carried out by referring to the conditions and parameters as listed in Table 4.1. The total thickness of a-C film deposited directly onto the substrate for 60 min was 85 nm. It is also noted that a thin Si-intermediate layer with the thickness of 24 nm was also added between a-C film and silica/QD layer for the adhesion improvement. Therefore, the total thickness for a-C film deposited for 60 min with Si-intermediate layer was 109 nm, while the thickness of 364 nm was obtained for a-C film deposited for 240 min with Si-intermediate layer.

The surface appearances of the a-C films with silica/QD underlayer fabricated by various conditions are shown Fig. 4.7. By observation with an optical microscope, all samples show the clear surface without any crack, wrinkle or spallation of a-C layer. The AFM images of all coatings are shown nearby. Note that the images were taken on the areas that included less dirt as much as possible. The points of the results obtained from the AFM images are that the surface morphology of a-C film conforms well to the morphology of silica/QD layer substrate in macroscopic level as can be seen in Fig. 4.7(a) for a-C deposited directly onto silica/QD layer without Si-intermediate layer (a-C/silica/QD coating). The random asperities as a consequence of the luminescent QD embedded in the silica matrix can also be observed. However, as the total thickness increases by the addition of Si-intermediate layer between a-C layer and silica/QD layer (a-C/Si/silica/QD), the surface morphology seems to become more flatten and the evolution of the surface roughness is dominated by the intrinsic a-C structure as shown in Fig. 4.7(b) and (c), respectively. In addition, the average surface roughness (R_a) of a-C/Si/silica/QD coating with total thickness of 364 nm is 1.35 nm, which is slightly higher than the R_a of the silica/QD coating substrate (1.07 nm). This indicates the high surface smoothness of a-C film in microscopic level although a thin silicon intermediate layer 24 nm thick is added between a-C film and substrate.

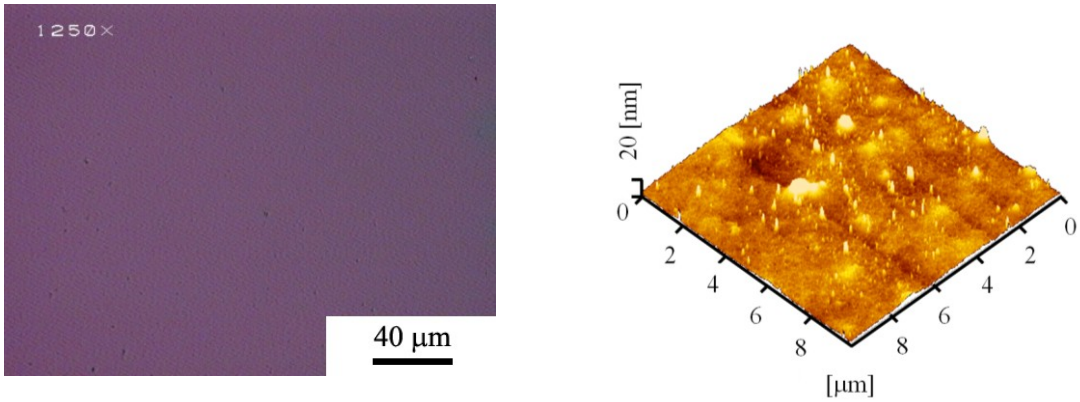

(a) a-C/silica/QD coating (a-C: 85 nm)

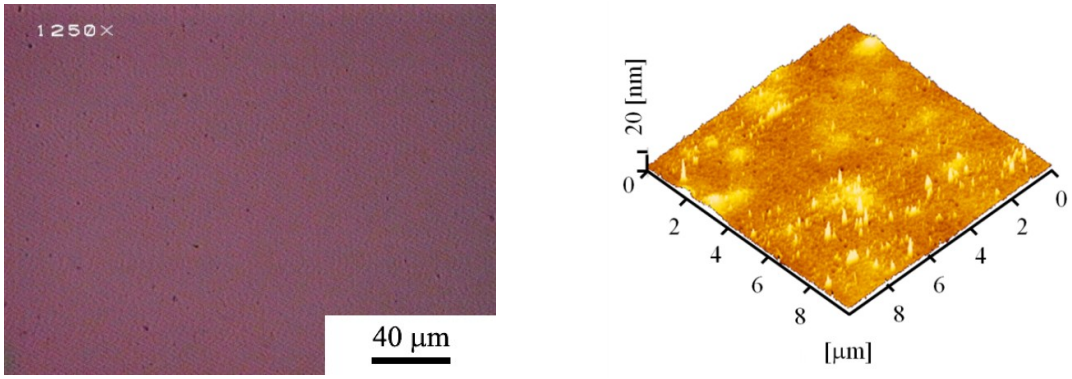

(b) a-C/Si/silica/QD coating (a-C/Si: 109 nm)

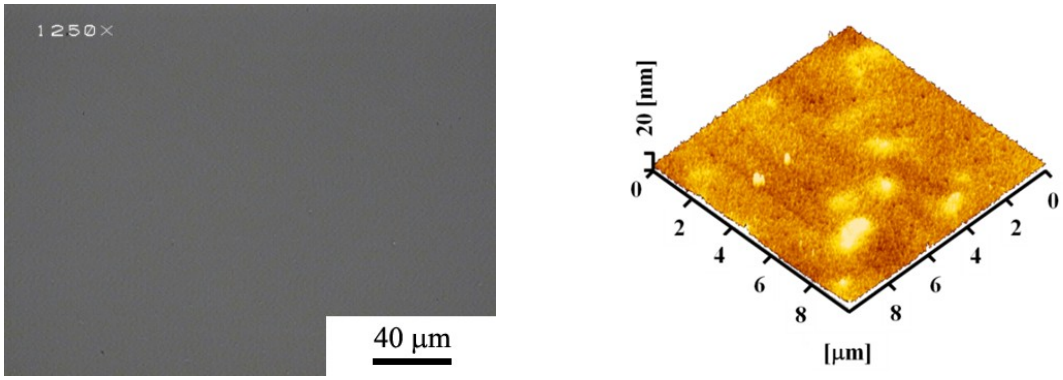

(c) a-C/Si/silica/QD coating (a-C/Si: 364 nm)

Fig. 4.7 Optical microscopic and AFM images of (a) a-C/silica/QD coating (a-C layer thickness: 85 nm), (b) a-C/Si/silica/QD coating (a-C/Si layer thickness: 109 nm) and (c) a-C/Si/silica/QD coating (a-C/Si layer thickness: 364 nm)

Raman spectroscopy was used to verify the structure of a-C films after being deposited onto the silica/QD layer. However, it was found that the Raman spectra of a-C coatings with low thickness (85 and 109 nm) were obtained accompanying with the strong luminescence background originated from the silica/QD underlayer as shown in Fig. 4.8(a). It is noted that the laser excitation of the Raman probe was focused on the surface of a-C layer to minimise the luminescent background as much as possible. Due to the strong luminescent background, the Raman peak of a-C that typically located in the range of 1200-1800 cm^{-1} are almost diminished for a-C/silica/QD coating. Although the Raman spectrum of a-C/Si/silica/QD coating shows an observable peak, it is difficult to distinguish the peak from the whole spectrum clearly. However, as the a-C film becomes thicker, the Raman peak of a-C is clearer with the reduced luminescent background as can be seen in Fig. 4.8(b). The spectrum shows the typical Raman spectrum of a-C film and is similar to that of a-C film deposited on Si-wafer as presented in Fig. 4.8(c). The spectra are composed of two bands as can be decomposed by simple Gaussian spectra, revealing the corresponding D band at 1360 cm^{-1} and G band at 1537 cm^{-1}, respectively. The position, band width (FWHM) and the integrated intensity ratio of D and G bands are summarised in Table 4.2.

Table 4.2 Positions and widths of the D and G bands from the Gaussian peaks fitting of the Raman spectra in Fig. 4.8(b) and (c) as well as ratio of their integrated intensities

a-C films with Si-intermediate layer deposited on	**D band**		**G band**		I_D/I_G
	Position (cm^{-1})	**FWHM (cm^{-1})**	**Position (cm^{-1})**	**FWHM (cm^{-1})**	
silica/QD	1360	316.9	1537	165.4	1.56
Si-wafer	1363	315.3	1538	165.2	1.56

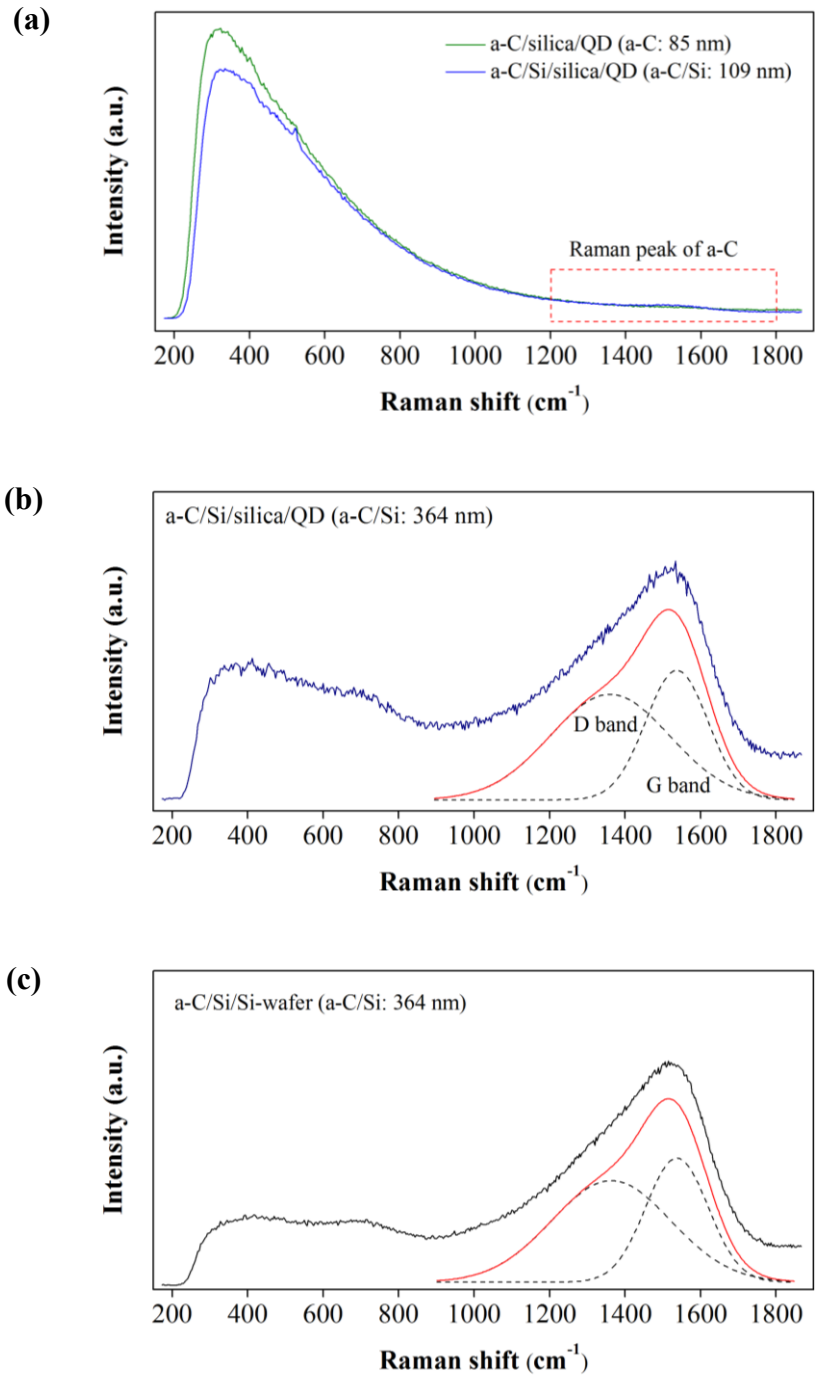

Fig. 4.8 Raman spectra of a-C coatings with silica/QD underlayer deposited by R.F. magnetron sputtering, in which (a) a-C/silica/QD (a-C: 85 nm) and a-C/Si/silica/QD (a-C/Si: 109 nm) coatings, (b) a-C/Si/silica/QD (a-C/Si: 364 nm) coating and (c) a-C/Si coating on Si-wafer (a-C/Si: 364 nm)

Tribological properties of both a-C/silica/QD and a-C/Si/silica/QD coatings were examined by rubbing against stainless steel ball in a ball-on-disk friction test apparatus under the test condition summarised in Table 4.3. The friction characteristics of the coatings are shown in Fig. 4.9. For a-C/silica/QD coating with the thickness of 85 nm, the coefficient of friction (COF) value at the beginning of the test is 0.2 and is kept the value in the range of 0.15-0.2 for only 2 metres. Then the COF value increases quickly to the higher value and finally reaches to 0.7 at the steady state within the short sliding distance. In contrast, a-C/Si/silica/QD coating with total thickness of 109 nm shows the improved friction behaviour. The coating shows the COF at 0.2 at the starting point and gradually decreases to the lower value in the range of 0.12-0.15 and keeping this value for a few metres of sliding distance. Then COF has a trend of gradual increase in the value and finally the COF value reaches to around 0.2 at the sliding distance of 20 metres. In addition to the a-C/Si/silica/QD coating, as the thickness of a-C film increases the friction characteristic is found to be more improved as can be seen for a-C coating with total thickness of 364 nm. The coating shows almost stable COF at 0.1 during the entire test, which is found to be identical to the typical COF value of a-C films deposited by sputtering [29-31].

Table 4.3 Ball-on-disk friction test conditions for a-C coatings with silica/QD underlayer prepared by R.F. magnetron sputtering

Ball:	Stainless steel (SUS 440C) (∅ 4.8 mm)
Normal load (N):	0.3
Sliding speed (mm/s):	13
Atmosphere:	Ambient air

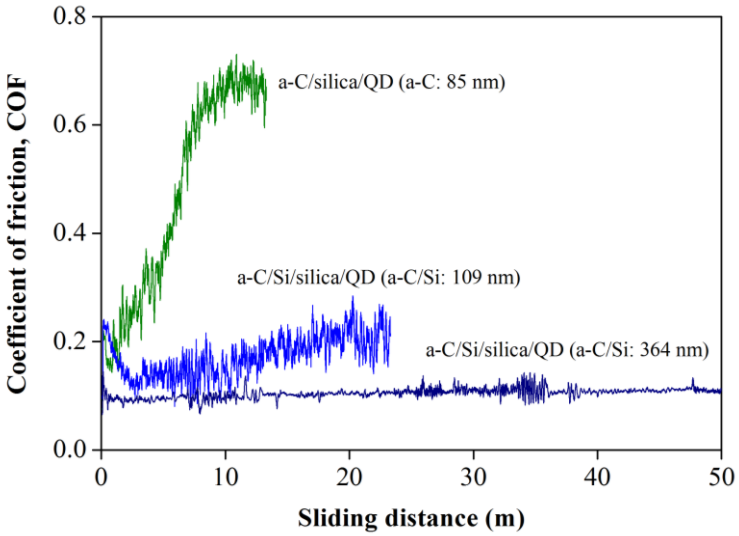

Fig. 4.9 Friction behaviours of various a-C coatings with silica/QD underlayer deposited by R.F. magnetron sputtering

The optical microscopic images observed on the wear tracks formed on all coatings are shown in Fig. 4.10. The a-C/silica/QD coating shows a completely removal of a-C coating as can be seen in Fig. 4.10(a). The result is consistent with high COF as obtained in Fig. 4.9. In case of a-C/Si/silica/QD coating, local damage is also found on the wear track as can be seen in Fig. 4.10(b), especially, near the defect that is preliminary formed on the as-fabricated silica/QD. However, at the free of defect zone, the uniform wear track is observed. This might be the reason of the fluctuation of the COF as well as the gradual increase of the COF of the coating as shown in Fig. 4.9. The wear track of a-C/Si/silica/QD coating with total thickness of 364 nm shows the smallest and uniform wear track as can be seen in Fig. 4.10(c), which is in agreement with the lowest and stable COF as observed during the friction test as shown in Fig. 4.9.

Compared with a-C/silica/QD coating, the wear track of the a-C/Si/silica/QD coating shows narrower wear track even though the film is subjected to the friction test with longer sliding distance, indicating the adhesion of a-C film to the silica/QD is improved by the Si-intermediate layer. It was proved that the adhesion strength of a-C film to silica or glass depended on the formation of Si–C bonds at the interface. In addition, the number of Si–C bonds is larger for the film having higher adhesion strength [32]. In the present study, it is believed that the formation of Si-C bonds is also occurred because there is no crack wrinkle or delamination of a-C film formed on the edge of the wear track as compared with the wear track obtained from a-C/ZnS:Mn coating system as already shown in Fig. 2.17(a) in chapter 2. However, the number of Si-C bonds seems to be not high enough since the bonding of Si atom in silica is mainly with oxygen (O). The formation of Si-C bonds can happen only at the dangling bonds of silicon that are formed on the glass surface by the plasma treatment. Addition of Si-intermediate layer increases the probability for the C atoms to form Si-C bonds directly with the Si atoms of the intermediate layer instead of silica layer. Since the adhesion strength between a-C film and silica/QD is improved, the tribological properties of a-C is consequently improved as clearly evidenced by the improved tribological properties when the thickness of a-C film is increased.

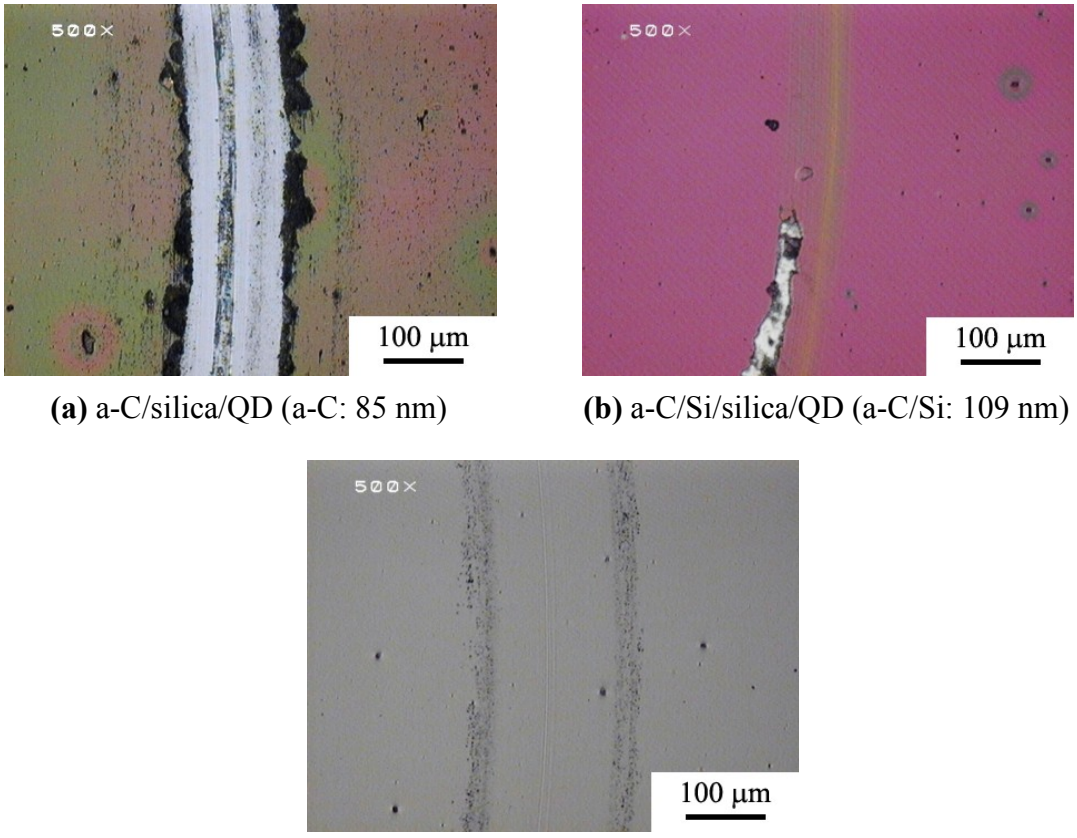

(a) a-C/silica/QD (a-C: 85 nm)

(b) a-C/Si/silica/QD (a-C/Si: 109 nm)

(c) a-C/Si/silica/QD (a-C/Si: 364 nm)

Fig. 4.10 Optical microscopic images observed on the wear tracks formed on the a-C coatings with silica/QD underlayer deposited by R.F. magnetron sputtering, in which (a) a-C/silica/QD coating (a-C: 85 nm) and (b and c) a-C/Si/silica/QD coatings (a-C/Si: 109 and 364 nm, respectively)

4.3.3 Demonstration of wear monitoring

As described briefly in the Chapter 3, in order to demonstrate the wear monitoring of a-C film through luminescent spectroscopy technique, the relationship between luminescent intensity and the thickness of coating should be formulated. The previous section has shown that the a-C/Si/silica/QD coatings exhibited the improved tribological properties. Therefore, this coating system has been focused in this section. Amorphous

carbon (a-C) films with several thicknesses have been deposited on to silica/QD with equal thickness of Si-intermediate layer of 24 nm. The luminescent intensity detected from each a-C coating was measured with Raman spectrometer by measuring relatively to the bare silica/QD layer. Figure 4.11 shows the Raman spectra of the coatings measured at various a-C coating thicknesses. The inset in Fig. 4.11 illustrates the procedure to measure the spectra. Initially the Raman spectra were collected from silica/QD coating from the masked area that was made prior to deposition of a-C coating. Then the spectra from the coating were collected by only moving the stage, while the lens or the excitation laser was remained their initial position. It is apparent that the relative intensity of the luminescence background detected from the coating is decreased when the thickness of a-C films increases. As the thickness of the coating increases to 364 nm, the luminescence background on the Raman spectrum almost disappears.

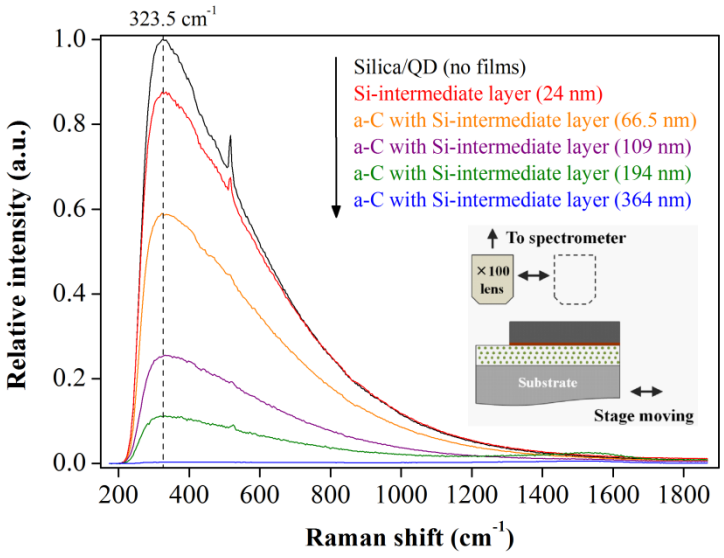

Fig. 4.11 Luminescence investigation by Raman spectroscopy measured from the coatings at various a-C coating thicknesses

From the Raman spectra plotted in Fig. 4.11, each maximum intensity of the luminescence background at 323.5 cm^{-1} was extracted and plotted against the total thickness of the coating as shown in Fig. 4.12. The data presented on the figure were the average of four measurements. It can be seen that the relative luminescent intensity decreases exponentially with increasing of the coating thickness. The similar trend was also obtained by Scharf and Singer [33], who demonstrated the relationship between the Raman intensity of silicon substrate and the thickness of single layer diamond-like nanocomposite. The demonstration was carried out based on the Beer-Lambert law, which states that the intensity of the light passing through a solid will be attenuated by an amount proportional to $e^{-\alpha l}$, where l is the path length that the light travels and α is the absorption coefficient, which is material dependent factor (neglecting the surface reflectivity).

In order to reveal the relationship between luminescent intensity and coating thickness, the data in Fig. 4.12 were fitted exponentially. The fitted curve as well as the relationship equation is shown together with the data in the same figure. Care should be taken here that the fitting has been performed using the luminescent intensity obtained from Si-intermediate layer as the origin point. In addition, the luminescent intensity was measured relatively to the bare silica/QD layer. For the first 24 nm, the attenuation of luminescence intensity is governed by the absorption coefficient and the thickness of Si-intermediate layer, which is shown in the shaded area in the figure. As the coating thickness increases and enters to the a-C film region, the luminescent intensity is attenuated by the fixed term of Si-intermediate layer and the variable term of a-C film. By fitting the data in this region, the whole thickness of a-C films can be monitored easily and precisely. In general, if the a-C film has been worn out to a certain thickness, the remaining thickness of the coating can be estimated by measuring the luminescent intensity and using the relationship shown in Fig. 4.12. It is also further expected from the equation that if the

relative luminescent intensity detected from the coating reaches to approximately 0.9, the remaining thickness should be 24 nm. This indicates the whole a-C film has been removed remaining only the Si-intermediate layer.

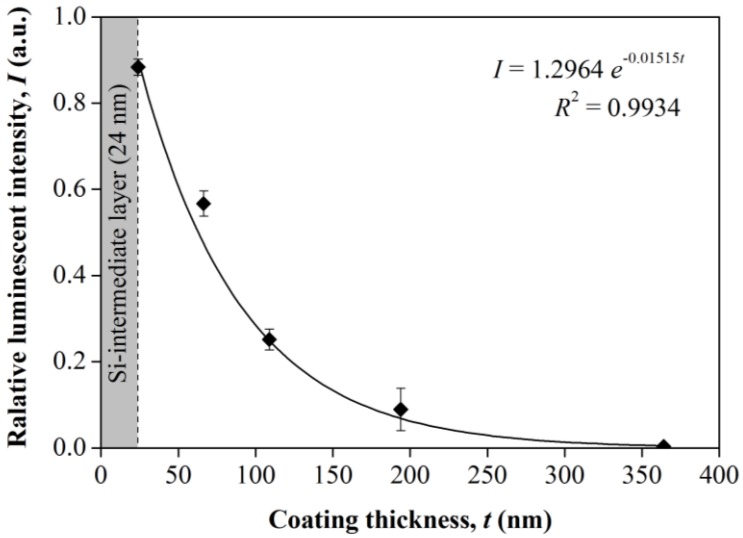

Fig. 4.12 Relationship between luminescent intensity from the coating as a function of coating thickness including the fitted equation and coefficient of determination (R^2)

The luminescent intensity from the wear track of a-C coating after the friction test was detected to demonstrate the wear monitoring and determining the remaining thickness of the a-C coating at the point that was worn out. The result of demonstration by luminescence spectroscopy will be compared with the surface profile analysis by AFM. As mentioned earlier in the experimental section that the Raman detection mode in the present study was spot mode with a spot size of around 1 μm, the detection was carried out only at the deepest zone of the wear track. Furthermore, the spectra were collected at the different three adjacent points, where the acquisition time of detection at each point was 3 times in every 5 sec.

Raman spectra obtained from the wear track of a-C/Si/silica/QD coating with total thickness of 364 nm within the white dashed area in Fig. 4.13(a), taken from different three places within the area, are plotted in Fig. 4.13(b). The spectrum obtained from the coating at virgin condition is also shown in the figure for comparison. The Raman spectra that indicate the a-C structure (at 1000-1800 cm^{-1}) are also observed. It can also be seen that the luminescence background with the peak at 323.5 cm^{-1} on the spectra obtained from the wear track are noticeably increased in all detected points. By simply replacing the luminescent intensity value into the fitted relationship obtained in Fig. 4.12, the thickness of the coating could be obtained, which can be implied directly as the remaining thickness of the coating. The luminescent intensity detected at each point as well as the corresponding coating thickness are summarised in Table 4.4.

Table 4.4 Determination of remaining coating thickness after the friction test of a-C/Si/silica/QD coating by luminescent spectroscopy and profilometry

Position on wear track (Arbitrary)	**By luminescent spectroscopy**		**By profilometry (AFM)**	
	Relative luminescent intensity (a.u.)	**Corresponding coating thickness (nm)**	**Wear depth (nm)**	**Remaining thickness (nm)**
Position 1	0.00687	345.9	15.1	348.9
Position 2	0.00623	352.3	13.5	351.5
Position 3	0.00633	351.6	13.7	350.3
Position 4	-	-	13.0	350.0
Position 5	-	-	12.9	351.1
Average	0.00648	349.9	13.6	350.4

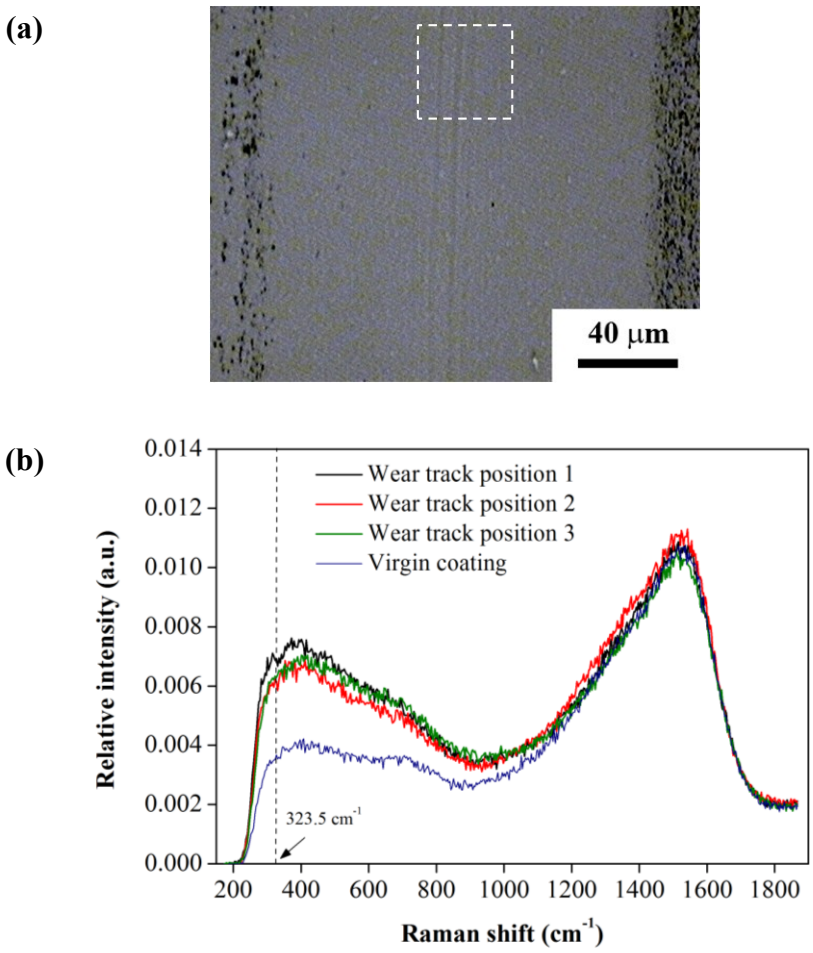

Fig. 4.13 (a) The area on wear track of a-C/Si/silica/QD coating with total thickness of 364 nm for wear monitoring demonstration, (b) Raman spectra obtained from the wear tracks at different three adjacent positions compared with the spectrum obtained from the virgin coating

The surface profiles scanned across the wear track were also analysed to measure the depth of the wear tracks. The AFM profiles were scanned across the wear tracks from the same area shown in Fig. 4.14(a). An example of the wear profile analysis is illustrated in Fig. 4.14(b). The remaining thickness of the coating calculated by subtraction of the wear depth with the total thickness could subsequently be obtained. The profiles scanned

across the track at five adjacent positions were taken along direction of the sliding. The results of wear depth and corresponding remaining thickness are also summarised in Table 4.4. The remaining thicknesses resulted from the luminescent spectroscopy are in the range of 345.9-352.3 nm with the average value of 349.9 nm, whereas the thicknesses resulted from profilometry are in the range of 348.9-351.5 nm with the average value of 350.4 nm. It shows that the results obtained by luminescent spectroscopy are in the range of the results obtained by profilometry.

(a)

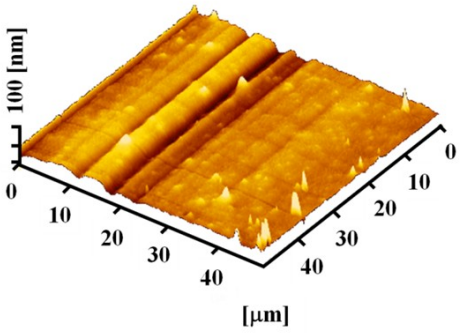

(b)

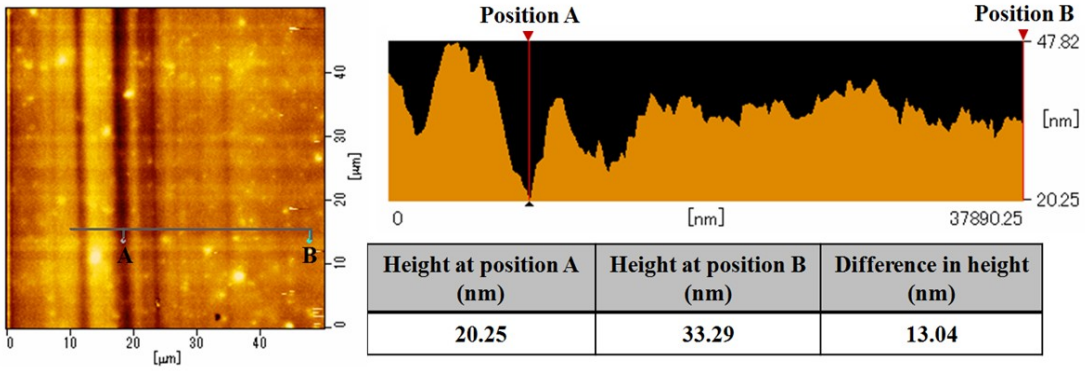

Height at position A (nm)	Height at position B (nm)	Difference in height (nm)
20.25	33.29	13.04

Fig. 4.14 (a) AFM image obtained from the wear track at white dash area shown in Fig. 4.13, and (b) surface profile scanning across the wear track analysed by AFM (Note that position A and B are the reference positions for measuring the depth of wear track)

By considering the average value, the results obtained from both methods correspond well to each another with an error in decimal point position. The results suggest that monitoring the wear life of a-C films by luminescent spectroscopy is feasible, even though the demonstration was carried out *ex situ*, in which the error caused by the positioning mismatch can be occurred. However, the obtained result on the wear track profile from several point measuring shows the narrow deviation, which suggest the wear depth of a-C films was considerably uniform.

Furthermore, not only the tribological characteristic influences the wear sensing capability, but also the optical absorption characteristic of the coating does [34]. Concerning the Raman spectra of a-C films detected at the wear track position as shown in Fig. 4.13(b), all spectra fit well with the spectrum detected from the virgin surface of a-C coating. This indicates the structure of a-C film does not change by the friction test. Generally, friction can induce the graphitisation to the sublayer surface of a-C film at the point of contact, resulting in the structural transformation from diamond-like to graphite-like structure [35,36]. This occurrence may affect to the sensing capability because the structural change can lead to the change of optical absorption characteristic of the coating [33]. Since there was no occurrence of structural change in present work, the wear monitoring technique by luminescent spectroscopy was feasible in this region.

4.4 Conclusion

In this chapter, fabrication of a-C coating with luminescent wear sensing underlayer and demonstration of the wear monitoring of a-C coating through luminescent spectroscopy wear carried out. Silica coating containing luminescent CdSe/ZnS quantum dots (silica/QD) was used as the wear-sensing layer and was fabricated by spin coating and

low temperature curing of liquid polysilazane mixed with quantum dots. The as-fabricated silica/QD layer showed surface smoothness in nanometre scale with nanometre-height random asperities due to the embedded quantum dots in the silica matrix. The a-C films were deposited onto the silica/QD layer by R.F. magnetron sputtering method. It was found that the adhesion strength between a-C film that deposited directly onto the silica/QD layer was not strong enough since the film wore out easily during the friction test. However, the adhesion as well as the friction property of a-C film on silica/QD underlayer was significantly improved by addition of thin Si-intermediate layer between a-C film and silica/QD layer.

The as-fabricated silica/QD coating exhibited strong luminescence as detected by Raman spectroscopy. After the deposition of a-C film with Si-intermediate layer to several thicknesses onto the silica/QD layers, it was found that the luminescent intensity was decreased when the thickness of a-C film increased. When the total thickness of coating reached to 364 nm, the luminescence from the sensing layer was almost unable to be detected. The relationship between luminescent intensity and coating thickness was found to be decayed exponentially. Wear monitoring of the coating was demonstrated by detecting the luminescent intensity from the wear track of the coating after friction test and determining the remaining thickness by utilising the relationship between luminescent intensity and coating thickness. The results showed that the remaining thickness of coating determined by luminescent spectroscopy coincided well with the result obtained by profilometry. This suggests that wear life monitoring of a-C films trough luminescent spectroscopy is feasible.

4.5 References

[1] T. Kubo, E. Tadaoka and H. Kozuka : J. Mater. Res., **19** (2004) 635.

[2] B. Bhattacharjee, D. Ganguli, S. Chaudhuri and A.K. Pal : Thin Solid Films, **422** (2002) 98.

[3] C. Bullen, P. Mulvaney, C. Sada, M. Ferrari, A. Chiasera and A. Martucci : J. Mater. Chem., **14** (2004) 1112.

[4] S.M. Reda : Acta Mater., **56** (2008) 259.

[5] C.J. Murphy : Anal. Chem., **74** (2002) 520A.

[6] A.D. Dukes III, J.R. McBride and S.J. Rosenthal : ECS Transactions, **33** (2011) 3.

[7] B.O. Dabbousi, J. Rodriguez-Viejo, F.V. Mikulec, J.R. Heine, H. Mattoussi, R. Ober, K.F. Jensen and M.G. Bawendi : J. Phys. Chem. B, **101** (1997) 9463.

[8] P. Reiss, M. Protiere and L. Li : Small, **5** (2009) 154.

[9] Q. Wang, N. Iancu and D.K. Seo : Chem. Mater., **17** (2005) 4762.

[10] L. Sorensen, G.F. Strouse and A.E. Stiegman : Adv. Mater., **18** (2006) 1965.

[11] P. Colombo, G. Mera, R. Riedel and G.D. Soraru : J. Am. Ceram. Soc., **93** (2010) 1805.

[12] F. Bauer, U. Decker, A. Dierdorf, H. Ernst, R. Heller, H. Liebe and R. Mehnert : Prog. Org. Coat., **53** (2005) 183.

[13] H. Kozuka, M. Fujita and S. Tamoto : J. Sol-Gel Sci. Technol., **48** (2008) 148.

[14] M. Günthner, K. Wang, R.K. Bordia and G. Motz : J. Eur. Ceram. Soc., **32** (2012) 1883.

[15] A. Schütz, M. Günthner, G. Motz, O. Greibl and U. Glatzel : Surf. Coat. Tech., **207** (2012) 319.

[16] B. Bhattacharjee, C.H. Hsu, C.H. Lu and W.H. Chang : Physica E, **33** (2006) 388.

[17] H. Ma, G.H. Ma, W.J. Wang, X.X. Gao and H.L. Ma : Chin. Phys. B, **17** (2008) 1280.

[18] Y.J. Choi, Y.J. Kim, J.W. Lee, Y. Lee, Y. Lim and H.W. Chung : J. Nanosci. Nanotechnol., **12** (2012) 2160.

[19] F. Ay and A. Aydinli : Opt. Mater., **26** (2004) 33.

[20] P.G. Pai, S.S. Chao, Y. Takagi and G. Lucovsky : J. Vac. Sci. Technol. A, **4** (1986) 689.

[21] A.G. Chaudhuri and S. Paria : Chem. Rev., **112** (2012) 2373.

[22] J. Hoy, P.J. Morrison, L.K. Steinberg, W.E. Buhro and R.A. Loomis : J. Phys. Chem. Lett., **4** (2013) 2053.

[23] B.O. Babbousi, J. Rodriguez-Viejo, F.V. Mikulec, J.R. Heine, M. Mattoussi, R. Ober, K.F. Jensen and M.G. Bawendi : J. Phys. Chem. B., **101** (1997) 9463.

[24] A.V. Baranov, Y.P. Rakovich, J.F. Donegan, T.S. Perova, R.A. Moore, D.V. Talapin, A.L. Rogach, Y. Masumoto and I. Nabiev : Phys. Rev. B, **68** (2003) 165306.

[25] Y. Lee, S.H. Lee, S. Lee, H. Lee, J. Kim and J. Joo : Appl. Phys. Lett., **102** (2013) 033109.

[26] Y. Zhao, D. Yang, D. Li and M. Jiang : Mater. Sci. Eng. B, **116** (2005) 95.

[27] H. Usui, H. Kikuchi, K. Tanaka, S. Miyata and T. Watanabe : J. Vac. Sci. Technol. A, **16** (1998) 108.

[28] S. Xu, D. Flynn, B.K. Tay, S. Prawer, K.W. Nugent, S.R.P. Silva, Y. Lifshitz and W.I. Milne : Phil. Mag. B, **76** (1997) 351.

[29] B.K. Gupta and B. Bhushan : Wear, **190** (1995) 110.

[30] E. Mounier, P. Juliet, E. Quesnel and Y. Pauleau : Surf. Coat. Tech., **76** (1995) 548.

[31] B. Rother, U. Herrmann and S. Schulze : Thin Solid Films, **398** (2001) 187.

[32] S. Takeda and S. Suzuki : J. Vac. Sci. Technol. A, **22** (2004) 1297.

[33] T.W. Scharf and I.L. Singer : Thin Solid films, **440** (2003) 138.

[34] C. Muratore, D.R. Clarke, J.G. Jones and A.A. Voevodin : Wear, **265** (2008) 913.

[35] H. Ronkainen, S. Varjus, J. Koskinen and K. Holmberg : Wear, **249** (2001) 260.

[36] Y. Liu, A. Erdemir and E.I. Meletis : Surf. Coat. Tech., **82** (1996) 48.

CHAPTER 5

SUMMARY OF THESIS

5. Summary of thesis

5.1 Thesis conclusions

Amorphous carbon (a-C) coatings with luminescent wear-sensing capability using ZnS-based underlayer have been developed. The structure of the coating consists of a-C film, which is a tribological layer and luminescent wear-sensing layer, which is mainly ZnS-based material. The concept of wear monitoring of a-C film through luminescent spectroscopy is that the degree of luminescence from underlayer is monitored when the a-C layer is worn out to a certain degree. Three a-C coating systems have been fabricated and characterised their physical, mechanical, luminescent and tribological properties as well as demonstrated the wear-sensing capability.

In chapter 2, the a-C coatings with ZnS:Mn underlayer has been initially fabricated. The single layer of luminescent ZnS:Mn (5 at.% Mn) was fabricated by R.F. magnetron sputtering method. It was found that the luminescent properties of ZnS:Mn films were enhanced by post-annealing at 700°C for 60 min in Ar atmosphere. ZnS:Mn films exhibited strong yellowish-orange at the peak centre 587 nm under irradiated with UV light at 365 nm. The a-C films were subsequently deposited onto the luminescent ZnS:Mn layer by the same sputtering method for 60 min with a deposition rate of 1.4 nm/min. The obtained a-C/ZnS:Mn coating shows a clear surface without cracks or wrinkle form on the coating surface. The luminescence from the ZnS:Mn layer could not be detected, suggesting the a-C film can prevent the luminescence mechanism to be occurred. However, it was found that the adhesion between a-C film and ZnS:Mn layer was not strong enough. The a-C film peeled off easily during the friction test. Thin Si-intermediate layer with the thickness of 24 nm was added between a-C film and ZnS:Mn layer for the purpose of adhesion improvement, but neither adhesion strength nor friction properties was improved.

Although the coating exhibited weak tribological properties, the luminescence spectrum the ZnS:Mn underlayer could be detected again with the spectrum shape and peak similar to the as-fabricated ZnS:Mn film, suggesting the feasibility to use ZnS-based material as a sensing layer.

In chapter 3, the second coating system was developed with improved adhesion property between a-C film and luminescent underlayer. In this system, the composite based coating using epoxy resin coating containing ZnS:Cu phosphor powder (EP/ZnS:Cu) was fabricated as a wear-sensing underlayer. ZnS:Cu phosphor powder with the particle size of 10-20 μm was mixed with and epoxy resin at the concentration of 5 wt.%. The mixture was dropped onto the substrate and covered by polystyrene (PS) film to control the smoothness and flatness of the coating. After curing at 40°C for 12 hr and removal of PS film, the coating exhibited a clear and flat surface with the thickness of 50 μm and the smoothness conforming to the PS film. The coating exhibited a strong green luminescent spectrum with the peak centre at 525 nm under the UV excitation, which can be assigned to the luminescence from the embedded ZnS:Cu powder. The a-C films were deposited onto the EP/ZnS:Cu layer by sublimation of fullerenes (C_{60}) in electron beam excited plasma (EBEP) and pulsed vacuum arc deposition (VAD) methods. It was found that deposition of a-C films by sublimation of C_{60} in EBEP caused the physical degradation to the EP/ZnS:Cu coating due to the strong interaction with Ar plasma during the deposition. In case of deposition of a-C films by pulsed VAD, a random crack network and the corrugated surface texture were formed due to the difference in elastic properties of hard a-C film and soft polymer epoxy layer. However, a-C film showed the structure of typical a-C film without any surface damage. The luminescent intensity detected from EP/ZnS:Cu layer was found to be decreased exponentially as the thickness of a-C film increased. As the thickness of a-C film increased to 240 nm, the luminescence from the underlayer was

unable to be detected. The friction test results revealed that a-C film adhered well to the EP/ZnS:Cu underlayer and provide the coefficient of friction as typical as monolithic a-C film when it was rubbed against alumina ball. After the friction test against the alumina ball, the luminescence from the underlayer could be detected again, suggesting that the a-C film has worn out. However, the precise wear monitoring demonstration was difficult to be achieved because of non-uniform wear track and remarkably rough surface of a-C coatings.

In chapter 4, the final a-C coating with luminescent silica coating containing luminescent CdSe/ZnS quantum dots (silica/QD) was fabricated in order to improve the rigidity of the coating as well as surface smoothness to allow the demonstration of wear-monitoring become more precise. The luminescent silica/QD coatings were fabricated by spin coating of the mixture between a liquid polysilazane and a colloid of CdSe/ZnS QD (2.5 vol.%). After curing at 50°C for 3 hr in the high relative humidity atmosphere, the conversion of polysilazane to rigid silica network was occurred. The random asperities with the height of several nanometres were observed by AFM analysis, corresponding to the embedded CdSe/ZnS QD in the silica matrix. However, the average surface roughness was still in the nanometre scale. It was found that the coating exhibited a strong luminescent background as measured with Raman spectrometer, corresponding to the embedded CdSe/ZnS QD in the silica matrix. The a-C films were deposited onto the silica/QD layer by R.F. magnetron sputtering method. It was found that the adhesion as well as the friction property of a-C film with silica/QD underlayer was significantly improved by addition of thin Si-intermediate layer between a-C film and silica/QD layer. After the deposition of a-C film with Si-intermediate layer to several thicknesses onto the silica/QD layers, it was found that the luminescent intensity was decreased when the thickness of a-C film increased. When the total thickness of coating reached to 364 nm, the

luminescence from the sensing layer was almost unable to be detected. The relationship between luminescent intensity and coating thickness was found to be decayed exponentially. Wear monitoring of the coating was demonstrated by detecting the luminescent intensity from the wear track of the coating after friction test and determining the remaining thickness by utilising the relationship between luminescent intensity and coating thickness. The results showed that the remaining thickness of coating determined by luminescent spectroscopy coincided well with the result obtained by profilometry. This suggested that wear monitoring of a-C films by luminescent spectroscopy was feasible.

5.2 Considerable issues concerning the present research for further studies

According to the results obtained in the present research, it is apparent that wear monitoring of a-C films by the technique of luminescent spectroscopy is feasible. The considerable issues for applying this technique in the real applications can be pointed out in three main parts.

5.2.1 The luminescent sensing layer

As can be seen from the results obtained in Chapter 2 that a single layer of ZnS-based material (ZnS:Mn) exhibited strong luminescence, which is the first basic requirement for the wear-sensing layer. However the adhesion between ZnS:Mn layer to a-C layer was found to be insufficient although a thin silicon intermediate layer was added between them for the reason of adhesion improvement. The adhesion between a-C layer and luminescent layer was found to be improved by altering the luminescent layer to the composite structure as already presented in Chapter 3. The epoxy resin containing ZnS:Cu

powder showed the strong luminescence and adhesion to a-C layer. However, it was found that the surface morphology of the a-C coating was remarkably rough and the wear track of the coating was non-uniform due to mechanical properties mismatch between the a-C layer and the luminescent epoxy layer. Accordingly, the luminescent sensing layer with more rigid, smoother surface was fabricated in Chapter 4, which is silica coating containing luminescent CdSe/ZnS quantum dot. Although it was found that the adhesion of such layer to a-C layer was still insufficient, it could be solved by the addition of silicon intermediate layer. As a result, the tribological properties of a-C coating were significantly improved.

According to the results as summarised above, the roles of luminescent sensing layer are not only to exhibit strong luminescence, but also to support the overall coating since it is the additional layer to the conventional a-C coating system. Therefore, the basic requirements of the luminescent sensing layer should be;

- Strong adherent to a-C layer
- High rigidity
- Smooth surface
- Highly active to the excitation

5.2.2 Amorphous carbon layer

As explained in the Chapter 1, the wear-sensing capability from the luminescent sensing layer does not depend only on the wear mode of a-C layer, but it also depends on the optical absorption of a-C films. The optical absorption properties of a-C films are also varied a great deal with the types of a-C films as can be seen in Fig. 1.12. Therefore, in order to utilise the present wear monitoring technique, the relationship between luminescent intensity and thickness of a-C films should be formulated initially.

Since the present study showed that wear monitoring of a-C film can be achieved when the structure of a-C film was not changed or graphitisation of a-C film was not detected by the friction test. In this case the optical properties of a-C film remained unchanged, the effects of structural change of a-C film on the wear-sensing capability was not included in the present study. Therefore, further study concerning this issued should be performed.

5.2.3 Overall coating system

The demonstration of wear monitoring presented in this research was carried out in the fundamental way or *ex situ* demonstration, which is applicable to the coated parts that are not applied in the continuous operation, such as cutting tools. In case of the coated parts that are applied in the continuous operation, such as gears or bearings, it is worthy to demonstrate the monitoring in real time or so called *in situ*. However, the testing apparatus as well as the high sensitivity detecting equipment is needed for conducting this demonstration.

Acknowledgements

This thesis collects the work that I have spent three years for study. Several achievements and failures that I have experienced were the worthy lessons for my next step. Throughout this work, I am grateful to a number of people who have guided and supported and provided me the assistance.

Assoc. Prof. Atsushi Hirata, my advisor, for his guidance and support since the initial to the final step enabled me to develop an understanding of this work.

Prof. Hitoshi Tokura, our lab leader, for his warm welcoming to the lab and for his continuous support to the lab during my stay here as well as Assoc. Prof. Hirofumi Hidai, who is now at Chiba University.

Asst. Prof. Yuko Aono, for her availability and great support and assistance in everything during my stay here.

Akemi Tokioka-san, for her always kindness to me.

Prof. Toyohiko Yano, Asst. Prof. Katsumi Yoshida, from Department of Nuclear engineering for allowing me to use the hot-pressing machine to make the ZnS:Mn sputtering target and special thank to Mr. Noppasint Jiraborvornpongsa, who operated the machine and made the target for me.

Asst. Prof. Satoshi Momozono, for training and allowing me to use the nanoindentation apparatus.

Prof. Katsunori Hanamura, Assoc. Prof. Tomohisa Tanaka and Assoc. Prof. Hiroki Akasaka, the committees of my thesis presentation, for their valuable comments and suggestions on my thesis.

Prof. Hiroaki Morimura, Director of Tokyo Tech office (Thailand), for his always kindness and cheerfulness to me during my stay here.

The staffs of Centre of Advanced Materials Analyses, Monotsukuri Centre and Workshop of Mechanical Engineering department for their providing analysis equipments, experimental apparatus and professional making the necessary goods for my research.

The Tribology group at AIST Tsukuba, especially Dr. Tsuguyori Ohana, for giving me the opportunity to join the group during my internship period. I gained a lot of useful experiences from there.

Tokura-Hirata lab members since October 2009 to March 2013 for the wonderful moment, friendship and help given to me. Specially Ippei Nakagawa-san and Hiroyasu Kogo-san for being my tutors when I was here in the first year. In addition, thank you very much to Vaez-san, who helped me a lot during my stay here not only in the school, but also in daily life.

My Thai friends in Tokodai, who also shared the wonderful moments in Tokodai and Japan together with me as well as supported me everything during my stay here.

Japanese government scholarship, without the financial support from the Japanese government, really I could not be able to be here for my study.

TAIST-Tokyo Tech programme, for giving me the opportunity and making me to know the institute named “Tokyo Institute of Technology”.

My family, for their great encouragement, understanding, prays for me throughout my study here.

Finally, thanks to the Allah (S.W.T) for the great blessings and making me a strong and peaceful believer.